

# Modeling the 3D dynamic rupture of microearthquakes induced by fluid injection

Francesco MOSCONI<sup>1</sup>, Elisa Tinti<sup>2</sup>, Emanuele Casarotti<sup>3</sup>, Alice-Agnes Gabriel<sup>4</sup>, Antonio Pio Rinaldi<sup>5</sup>, Luca Dal Zilio<sup>6</sup>, and Massimo Cocco<sup>7</sup>

<sup>1</sup>Sapienza, Rome University

<sup>2</sup>Università La Sapienza

<sup>3</sup>Istituto Nazionale di Geofisica e Vulcanologia. Via di Vigna Murata

<sup>4</sup>Ludwig-Maximilians-University (LMU) Munich

<sup>5</sup>Swiss Federal Institute of Technology (ETHZ)

<sup>6</sup>Earth Observatory of Singapore

<sup>7</sup>Istituto Nazionale di Geofisica e Vulcanologia

June 24, 2024

## Abstract

Understanding the dynamics of microearthquakes is a timely challenge with the potential to address current paradoxes in earthquake mechanics, and to better understand earthquake ruptures induced by fluid injection. We perform fully 3D dynamic rupture simulations caused by fluid injection on a target fault for FEAR experiments generating  $M_w$  [?] 1 earthquakes. We investigate the dynamics of rupture propagation with spatially variable stress drop caused by pore pressure changes and assuming different constitutive parameters. We show that the spontaneous arrest of propagating ruptures is possible by assuming a high fault strength parameter  $S$ , that is, a high ratio between strength excess and dynamic stress drop. In faults with high  $S$  values (low rupturing potential), even minor variations in  $D_c$  (from 0.45 to 0.6 mm) have a substantial effect on the rupture propagation and the ultimate earthquake size. Our results show that modest spatial variations of dynamic stress drop determine the rupture mode, distinguishing self-arresting from run-away ruptures. Our results suggest that several characteristics inferred for accelerating dynamic ruptures differ from those observed during rupture deceleration of a self-arresting earthquake. During deceleration, a decrease of peak slip velocity is associated with a nearly constant cohesive zone size. Moreover, the residual slip velocity value (asymptotic value for a crack-like rupture) decreases to nearly zero. This means that an initially crack-like rupture becomes a pulse-like rupture during spontaneous arrest. In summary, our findings highlight the complex dynamics of small earthquakes, which are partially contrasting with established crack-like models of earthquake rupture.

# Modeling the 3D dynamic rupture of microearthquakes induced by fluid injection

**Mosconi F.<sup>1</sup>, Tinti E.<sup>1,2</sup>, Casarotti E.<sup>2</sup>, Gabriel A-A.<sup>3</sup>, Rinaldi A.P.<sup>4</sup>, Dal Zilio L.<sup>5</sup>, and Cocco M.<sup>2</sup>**

<sup>1</sup> La Sapienza Università di Roma, P.le Aldo Moro 5, 00185 Roma, Italia

<sup>2</sup> Istituto Nazionale di Geofisica e Vulcanologia, Rome, Italy

<sup>3</sup> Scripps Institution of Oceanography, UCSD, La Jolla, USA

<sup>4</sup> Swiss Seismological Service, Department of Earth Sciences, ETH Zürich, Switzerland

<sup>5</sup> Earth Observatory of Singapore, Nanyang Technological University, Singapore, Singapore,

Corresponding author: Francesco Mosconi (francesco.mosconi@uniroma1.it)

## Key Points:

- 3D dynamic rupture simulations of microearthquakes on a pressurized fault, with pore pressure profiles determined from poroelastic models.
- Modest variations of dynamic stress drop determine the rupture mode, distinguishing self-arresting from run-away ruptures.
- Runaway ruptures can dissipate more energy than self-arresting ones which display cracks transition into pulses upon arrest.

**Keywords:** induced earthquake, self-arresting rupture, runaway rupture, pore pressure changes, dynamic rupture propagation.

## Abstract

30 Understanding the dynamics of microearthquakes is a timely challenge with the potential to  
31 address current paradoxes in earthquake mechanics, and to better understand earthquake  
32 ruptures induced by fluid injection. We perform fully 3D dynamic rupture simulations caused  
33 by fluid injection on a target fault for FEAR experiments generating  $M_w \leq 1$  earthquakes. We

34 investigate the dynamics of rupture propagation with spatially variable stress drop caused by  
35 pore pressure changes and assuming different constitutive parameters. We show that the  
36 spontaneous arrest of propagating ruptures is possible by assuming a high fault strength  
37 parameter  $S$ , that is, a high ratio between strength excess and dynamic stress drop. In faults  
38 with high  $S$  values (low rupturing potential), even minor variations in  $D_c$  (from 0.45 to 0.6 mm)  
39 have a substantial effect on the rupture propagation and the ultimate earthquake size. Our  
40 results show that modest spatial variations of dynamic stress drop determine the rupture mode,  
41 distinguishing self-arresting from run-away ruptures. Our results suggest that several  
42 characteristics inferred for accelerating dynamic ruptures differ from those observed during  
43 rupture deceleration of a self-arresting earthquake. During deceleration, a decrease of peak slip  
44 velocity is associated with a nearly constant cohesive zone size. Moreover, the residual slip  
45 velocity value (asymptotic value for a crack-like rupture) decreases to nearly zero. This means  
46 that an initially crack-like rupture becomes a pulse-like rupture during spontaneous arrest. In  
47 summary, our findings highlight the complex dynamics of small earthquakes, which are  
48 partially contrasting with established crack-like models of earthquake rupture.

49

## 50 Plain language

51 Understanding small earthquakes, especially those induced by underground fluid injection, is  
52 crucial in earthquake science. In our study, we reproduce these events using computer  
53 simulations on a 50 meter wide fault, aiming to understand how fluid-induced stress changes  
54 affect the earthquake behavior. We find that earthquakes can stop under specific conditions,  
55 specifically when fault strength largely exceeds the difference between on-fault stress before  
56 and after the earthquake. Minor changes in rock properties, like static to dynamic friction  
57 transitions, significantly impact earthquake size. Our research also shows that stress variations  
58 on faults can determine if the earthquake is growing or arresting. We observe a significant  
59 spatial extension of the earthquake arrest phase, noting differences in features compared to  
60 earthquakes that exhibit accelerating rupture propagation. This distinct behavior is linked to  
61 the stress heterogeneity due to pore pressure gradient within the fault. Overall, our findings  
62 reveal the complex dynamics of small earthquakes, which is partially contrasting with the  
63 conventional crack theory.

## 64 1. Introduction

65 The study of earthquake mechanics and the analysis of source properties has been mainly  
66 focused on moderate to large seismic events (Kanamori, 2003; Schmedes et al., 2010; Harris,  
67 2017; Abercrombie, 2021). The investigation of the rupture process in micro-earthquakes, with  
68 magnitudes ranging between -4 and 2, has so far been carried out by spectral analysis of  
69 recorded data to derive source parameters such as seismic moment, source radius, stress drop  
70 and corner frequency (Imanishi and Ellsworth, 2006; Allmann et al., 2007, 2009; Selvadurai,  
71 2019; Abercrombie, 1995, 2021; Abercrombie and Rice, 2005; Cocco et al., 2016; 2023).  
72 These studies have been largely motivated by the need to constrain the scaling of earthquake  
73 source parameters – such as stress drop, radiated energy, source radius, and fracture energy –  
74 with seismic moment or total coseismic slip, laying the groundwork for our current  
75 understanding.

76 More recently, the emerging focus on induced seismicity and its related hazards has provided  
77 an opportunity to analyze faults more closely, improving our understanding of the dynamics  
78 that govern rupture initiation (Ellsworth, 2013; Grigoli et al., 2017; Moein et al., 2023; Galis  
79 et al., 2017). This was further promoted by the numerous laboratory experiments designed and  
80 performed to study the onset of dynamic instabilities in response to fluid injection on the rock  
81 sample, which provided relevant observations on induced laboratory earthquakes under  
82 controlled conditions (Scuderi and Collettini, 2016, Cappa et al., 2019; Hunfeld et al., 2021;  
83 Bolton et al., 2023; Volpe et al., 2023). While numerous studies on source complexity have  
84 concentrated on large earthquakes due to their associated severe damage and hazards, a  
85 persistent, unresolved, question in earthquake mechanics concerns the degree of heterogeneity  
86 and complexity influencing the rupture processes of microearthquakes. Furthermore, to the best  
87 of our knowledge, no studies have investigated the 3D rupture propagation and arrest of  
88 induced microearthquakes — an essential aspect in bridging the knowledge gap concerning  
89 induced seismicity and its relationship with microearthquakes.

90 Investigating the dynamics of microearthquakes necessitates the precise determination of  
91 constitutive parameters such as stress, friction, and critical slip at small spatial scales  
92 (millimeters to centimeters), which are crucial for understanding rupture propagation over  
93 meter-scale distances (1-100 m). Given the challenges in constraining source parameters using  
94 surface or near-surface data, innovative approaches have been proposed and adopted to collect  
95 near-source data and observations. These approaches include utilizing deep boreholes that  
96 intersect fault surfaces (Zoback et al., 2011; Tobin et al., 2022, among several others) as well

97 as underground laboratories providing access to fault zones at depths ranging between a few  
98 hundreds and a kilometer (Guglielmi et al. 2015; Lesko; 2015; among many others). Within  
99 this array of monitoring systems (deep borehole, underground labs and deep mines), the  
100 Bedretto Underground Laboratory for Geosciences and Geoenergies (BULGG) in the Swiss  
101 Alps provides access to a volume of crystalline faulted rocks at depth of 1000-1500 m (Ma et  
102 al., 2022; Achtziger et al., 2024). BULGG hosts the FEAR (Fault Activation and Earthquake  
103 Ruptures) ERC-Synergy project (Meier et al.; 2024) that aims at reactivating a natural fault  
104 under controlled conditions by stimulating the nucleation of a target earthquake of magnitude  
105  $M_w = 1$ . This event will be recorded with a dense multi-disciplinary on-fault monitoring system.  
106 Among several faults classified along the whole tunnel, the target fault for FEAR experiments,  
107 named hereinafter MC fault, has been identified (Achtziger et al., 2024; Volpe et al., 2023).  
108 The information required to constrain dynamic rupture simulations (e.g., Harris et al., 2018),  
109 including the fault geometry and stress state (slip tendency, stress orientation) as well as its  
110 frictional properties (Volpe et al., 2023) is available. Planned stimulation experiments within  
111 this fault zone, spanning 50-100 meters, will adhere to a precise injection protocol (Meier et  
112 al., 2024). The dedicated on-fault monitoring system is designed to capture microseismicity  
113 across a wide magnitude range ( $M_w$  -6 to 1), offering an unparalleled opportunity to examine  
114 the complex dynamics of rupture nucleation and propagation during microearthquakes within  
115 the magnitude range between 0 to 1.

116 The role of fluids in earthquake mechanics is well-documented in natural tectonic settings,  
117 anthropogenic activities, and laboratory experiments (Rice, 1992; Cocco and Rice, 2002;  
118 Miller et al., 2004; Ellsworth, 2013; Guglielmi et al., 2015; Viesca and Garagash, 2015;  
119 Martinez Garzon et al., 2016; De Barros et al., 2018; Cappa et al., 2019; Wang et al., 2024, and  
120 reference therein). Fault reactivation can result from an increase in the pore pressure  $P_f$   
121 (Hubbert and Rubey, 1959; Scholz, 1990), leading to a reduction in the effective normal stress  
122 ( $\sigma'_n = \sigma_n - P_f$ ) thereby influencing the frictional strength of the fault. In recent years, the  
123 growing energy demand, both fossil and renewable, has led to an increase in the activities  
124 related to the underground fluid injection. This requires to pose more attention on the hazard  
125 of the induced and triggered seismicity, in the context of oil and gas reservoir, underground  
126 carbon dioxide sequestration and geothermal energy (Ellsworth, 2013; Candela et al., 2018,  
127 Moein et al., 2023). Some examples of notable earthquakes associated to fluid injection are the  
128 2011  $M_w$  5.7 and 5.0 earthquakes near Prague in Oklahoma, United States (Keranen et al.,  
129 2013), the  $M_w$  5.8 Pawnee, Oklahoma, in 2016 (Yeck et al., 2017) and the 2017  $M_w$  5.5

130 earthquake near an enhanced geothermal site in Pohang, South Korea (Grigoli et al., 2018; Kim  
131 et al., 2018; Lee et al., 2019, Palgunadi et al., 2020).  
132 Numerous studies analyzed fault slip reactivation under elevated pore pressure, and both fluid-  
133 driven seismic and aseismic slip has been observed within a complex spectrum of fault-slip  
134 behavior (Garagash and Germanovich, 2012; Cappa et al., 2019; Larochelle et al., 2021; Dal  
135 Zilio et al., 2022; Ciardo and Rinaldi, 2022; Bolton et al., 2023). Experimental studies across  
136 various scales have highlighted the emergence of a zone characterized by aseismic slip, or  
137 creeping, adjacent to the injection point (Cornet, 2012, 2016; Garagash and Germanovich,  
138 2012; Guglielmi et al., 2015; Scuderi and Collettini, 2016). The nature of the stress state in the  
139 stimulated fault zone influences this aseismic slip, leading to strain-energy accumulation  
140 outside the slipping area. This process continues until a critical nucleation length is reached, at  
141 which point a dynamic instability can propagate (Uenishi and Rice, 2003; Cebry et al., 2022).  
142 Upon nucleation, the rupture propagates dynamically, characterized by high slip velocities and  
143 rupture speeds, generating seismic waves. The arrest of the rupture occurs when the rupture  
144 front does not possess enough energy to continue propagating. While the mechanisms of  
145 natural earthquake arrest are still debated (Kame and Yamashita, 1999; Galis et al., 2019; Ke  
146 et al., 2022; among several others), dynamic rupture models typically assume locally low-stress  
147 or high frictional strength, for example by prescribing spatial heterogeneities of the shear stress  
148 or static friction coefficient (Das & Aki, 1977; Harris et al., 2018; Ramos et al., 2021).  
149 The study of rupture propagation and arrest in induced earthquakes allows the differentiation  
150 between self-arrested and runaway ruptures. The former refers to ruptures that spontaneously  
151 stop at a finite distance from the nucleation zone often remaining within the pressurized patch,  
152 while the latter describes ruptures that extend across the entire fault, ceasing only at fault  
153 boundaries due to geometrical complexities, stress or strength heterogeneities (Galis et al.,  
154 2017; Ke et al., 2018, 2022). This classification elucidates the rupture dynamics without  
155 necessarily invoking heterogeneous stress patches. Galis et al., (2017) pointed out that, while  
156 injection-induced earthquakes may cause severe seismic hazard, they also represent an  
157 opportunity to gain insights in earthquake physics. They used a linear slip weakening law to  
158 model an induced rupture and Linear Elastic Fracture Mechanics (LEFM) to interpret the  
159 transition between self-arresting and runaway induced earthquakes. They found that this  
160 transition is mainly controlled by frictional parameters and stress heterogeneity. Additionally,  
161 these authors corroborate the dependence of the expected magnitude of the induced earthquake  
162 on the radius of the pressurized area and on the injected fluid volume (Mc Garr, 2014; Galis et

163 al., 2017; De Barros et al., 2019; Moein et al., 2023). However, a fundamental physical  
164 explanation of why dynamic rupture arrests or can continue propagating is still elusive.

165 In this study, we concentrate on the spontaneous dynamic simulation of rupture processes for  
166 induced earthquakes with a maximum magnitude of less than 1 ( $M_w < 1$ ). Our simulations  
167 encompass the full dynamics of earthquake rupture and seismic wave propagation within a 3D  
168 volume, based on a linear slip-weakening model to describe shear stress evolution at the rupture  
169 front and initiated by pore fluid pressurization. We apply our model to the target fault within  
170 the Bedretto Underground Laboratory for Geosciences and Geo-energies (BULGG) at an  
171 approximate depth of 1500 meters.

172 The aim of this study is to simulate the propagation and the arrest of dynamic ruptures on the  
173 pressurized fault selected for FEAR experiments. The fault is characterized by initially uniform  
174 frictional parameters and is subjected to uniform prestress. This simplified initial stress  
175 condition is adopted to emphasize the role of pore pressure changes on spontaneous dynamic  
176 rupture propagation. A realistic pore pressure profile caused by fluid injection in a nucleation  
177 patch is simulated considering the poroelastic response of the fault zone. The rupture process  
178 during induced microearthquakes is investigated to shed light on the key features of dynamic  
179 propagation as well as the constitutive parameters influencing the extent of the rupture before  
180 its arrest, determining the magnitude of the induced earthquake.

181

## 182 2. Methods and Source Parameterization

183 We utilize the open-source software SeisSol ([www.seissol.org](http://www.seissol.org)) to model the 3D spontaneous  
184 rupture propagation of micro-earthquakes on a 3D fault plane. SeisSol is based on the arbitrary  
185 high-order derivative discontinuous Galerkin (ADER-DG) method (Dumbser and Käser,  
186 2006), and solves the 3D elastodynamic equation for spontaneous frictional failure on a  
187 prescribed fault surface, whereas for the seismic wave propagation it computes the elastic wave  
188 equation in heterogeneous media (Pelties et al., 2012). The applicability of SeisSol has been  
189 verified in various earthquake scenarios, ranging from models including a simple planar fault  
190 to more complex fault geometries involving geometric discontinuities, non-planarity, fault  
191 roughness, and multiple intersecting adjacent fault branches (Harris et al., 2018; Ulrich et al.,  
192 2019; Tinti et al., 2021; Taufiqurrahman et al., 2022; Biemiller et al., 2023, Gabriel et al.,  
193 2023). This study presents the first dynamic rupture simulation for an induced micro-

194 earthquake on a decametric-scale planar fault (50 m length), under stress conditions determined  
195 by fluid injection and pore-pressure changes.

196

197 **2.1. Linear slip-weakening friction law**

198 Dynamic earthquake modeling requires the use of a fault constitutive law which describes shear  
199 traction evolution in each point on the fault characterizing the breakdown stage and dynamic  
200 weakening near the rupture front. Different constitutive laws analytically describe the shear  
201 stress as a function of diverse constitutive variables, such as slip, slip velocity, state, and  
202 temperature. Here, we adopt the linear slip-weakening (LSW) constitutive law (Ida, 1972)  
203 because it is simple and allows the clear definition of fracture energy and a direct control on  
204 different key parameters such as fault strength and dynamic stress drop during the rupture  
205 propagation.

206 This constitutive relation is characterized by the peak stress value on the fault  $\tau_p = \mu_s \sigma'_n$ , the  
207 dynamic residual (i.e., frictional) stress level  $\tau_d = \mu_d \sigma'_n$ , and the critical slip distance  $D_c$ , as

208

$$209 \tau = \begin{cases} \left[ \mu_s - (\mu_s - \mu_d) \frac{\delta}{D_c} \right] \sigma'_n, & \delta < D_c \\ \mu_d \sigma'_n, & \delta > D_c \end{cases} \quad (1)$$

210

211 where  $\mu_s$  and  $\mu_d$  are the static and dynamic friction coefficients, respectively,  $\sigma'_n$  is the effective  
212 normal stress and  $\delta$  the slip. When the shear stress reaches its peak value the fault starts  
213 slipping and the shear stress decreases linearly from the peak to the residual stress value over  
214 a critical slip distance  $D_c$ . This breakdown stress drop ( $\Delta\tau_p = \tau_p - \tau_d$ ) corresponds to a friction  
215 decrease from the static to the dynamic friction coefficient. Once the slip exceeds the critical  
216 slip distance ( $D_c$ ), the shear traction becomes independent of slip and equal to the residual  
217 dynamic stress level  $\tau_d = \mu_d \sigma'_n$ . The final stress is equal to the residual stress level, and stress  
218 overshoot or undershoot are not considered. The energy dissipated to sustain the rupture  
219 propagation, namely the fracture energy, depends on the values of the breakdown stress drop  
220 and the critical slip weakening distance  $D_c$ .

221 According to equation (1), the strength excess ( $\tau_p - \tau_0$ ) is defined as the difference in shear  
222 stress between its peak and initial values, with the peak stress being equal to the yield strength  
223 of the fault. The strength excess occurs with no slip and is associated with a linear elastic and  
224 reversible process. The dynamic stress drop ( $\Delta\tau_d = \tau_0 - \tau_d$ ), is the stress released during the

225 dynamic weakening. Because the final stress is equal to the residual dynamic stress level ( $\tau_d$ ),  
226 the dynamic and static stress drop are the same. The ratio between the stress excess and the  
227 dynamic stress drop is the strength parameter  $S$ , as defined by the pioneering paper of Andrews  
228 (1976):

$$229 \quad S = \frac{(\tau_p - \tau_0)}{(\tau_0 - \tau_r)} \quad (2)$$

230  
231 Previous studies dealing with modeling earthquake ruptures have emphasized the importance  
232 of computing the non-dimensional strength parameter  $S$  that allows us to describe the potential  
233 of the fault to develop a rupture (Andrews, 1976; Das & Aki, 1977; Geubelle & Kubair, 2001;  
234 Liu & Lapusta, 2008; Barras et al., 2023). Andrews (1976) found that the parameter  $S$  controls  
235 the transition of a crack from sub-shear rupture to supershear rupture propagation. More recent  
236 studies have also demonstrated its significance in influencing rupture style (Gabriel et al., 2012;  
237 Bai and Ampuero, 2017) or its role in the context of induced seismicity (Galis et al., 2017).  
238 The parameter  $S$  measures the material strength (strength excess) relative to the stress release  
239 during dynamic rupture (dynamic stress drop). The strength excess quantifies the necessary  
240 stress to be concentrated at the rupture front, from the initial to the peak shear stress, needed  
241 for the propagation. On the other hand, the dynamic stress drop encompasses the stress released  
242 during the dynamic breakdown referred to the initial shear stress, characterizing the tectonic  
243 loading of the fault before the initiation of a dynamic rupture.  
244 The LSW constitutive law allows the interpretation of key features of the dynamic rupture  
245 propagation in terms of a few parameters, even in a very sensitive condition such as an induced  
246 earthquake. The advantage of working in a well constrained in-situ boundary condition, as  
247 provided by the Bedretto Lab, helps to decrease the a-priori assumptions and to investigate the  
248 dynamics of microearthquakes focusing on the less poorly constrained constitutive parameters  
249 (such as the critical slip distance  $D_c$ ).

## 250 2.2. Fault model and input parameters

251 We simulate a dynamic rupture scenario, for an induced earthquake, on a  $60^\circ$  dipping normal  
252 fault, embedded in a 3D elastic medium, with a P-wave speed of 2621 m/s, S-wave speed of  
253 1531 m/s and a density of 2620 kg/m<sup>3</sup>. To accurately define the fault geometry, we leverage  
254 in-situ geological and geophysical characterizations of the target fault, conducted as part of the  
255 FEAR project in the Bedretto Tunnel. These characterizations, detailed in Achtziger et al.  
256 (2024), reveal that the target fault exhibits an approximately planar geometry, extending

257 laterally for about 250 meters. In our model we consider a volume of 200 x 200 x 200 m and  
258 a fault dimension of 50 x 50 m, representing the fluid pressurized portion of the larger MC fault  
259 zone (Figure 1a). The computational domain is discretized using an unstructured mesh, with a  
260 total number of ~69 million tetrahedral elements. The elements in the volume change in size,  
261 transitioning from 12 cm length close to the fault to a maximum value of 15 m at the volume  
262 edge, in order to maintain both computational efficiency and high resolution, simultaneously.  
263 The well-constrained in-situ boundary conditions of the Bedretto Tunnel allow us to include a  
264 realistic on-fault stress state with negligible spatial variations due to the small fault dimension  
265 here considered. Therefore, we impose a constant normal and shear stress on the fault prior to  
266 fluid injection, with the former prescribed at  $\sigma_n = 22.7$  MPa and the latter to  $\tau_0 = 4.7$  MPa.  
267 The static ( $\mu_s$ ) and dynamic ( $\mu_d$ ) friction coefficients are considered homogeneous and constant  
268 over the fault. The static friction is  $\mu_s = 0.58$ , while the dynamic friction is assumed to be  $\mu_d =$   
269 0.21 for the first set of Models A and  $\mu_d = 0.15$  for the second set of Models B that will be  
270 discussed in the paper. The initial resulting stress conditions after the stress perturbation due  
271 the injection of fluid within each specific set of models will be described more in detail in the  
272 subsequent Section 3.

273 A crucial parameter in dynamic rupture simulations is the on-fault resolution to capture the  
274 stress dissipation in the cohesive zone, i.e. the spatial dimension along fault where the shear  
275 stress weakening occurs, evolving from the peak value to the residual level. Based on the  
276 extended analysis conducted by Wollherr et al. (2018) to achieve a well resolved cohesive zone  
277 we adopt a spatial discretization with an on fault mesh element size of 12 cm with a mean  
278 cohesive zone dimension of 0.34m (detailes in Supplementary material)

279

### 280 3. Stress changes from fluid injection

281 The main goal of this work is to investigate the characteristics of a dynamic rupture resulting  
282 from on-fault fluid pressurization, exploring various scenarios to understand the conditions  
283 leading to a self-arresting rupture with  $M_w < 1$ , as opposed to a runaway earthquake that  
284 ruptures the entire fault surface, resulting in a  $M_w > 1$ .

#### 285 3.1. Pore pressure changes profile

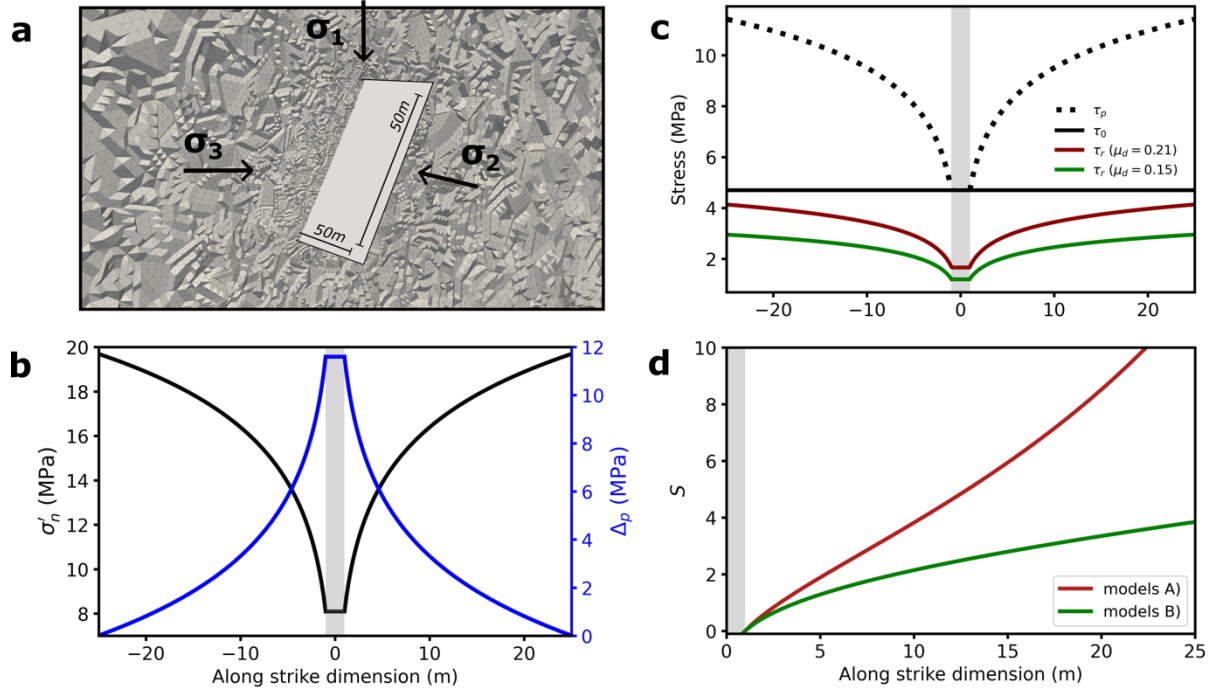
286 In order to create realistic pressure conditions on the fault zone, we employ the software  
287 TOUGH3-FLAC3D, that allows the simulation of coupled fluid flow and geomechanics

288 (Rinaldi et al., 2022). This approach aims at simulating complex non-linear behavior  
289 potentially occurring in the vicinity of the injection point, as well effects of a packed interval.  
290 The coupled approach allows us to account for full poroelasticity via porosity evolution as well  
291 as variation of permeability as function of geomechanical parameters (e.g. stress or strain). We  
292 develop a first-order model (50 m X 50 m X 50 m) with a fault zone dipping 60°, 20 cm thick,  
293 and cutting through an homogenous medium.

294 Initial conditions follow the state of stress found at the BedrettoLab (Bröker & Ma, 2022,  
295 Bröker et al., 2023), with minimum horizontal stress at 20 MPa, maximum horizontal stress at  
296 25 MPa, and vertical stress at 31 MPa for the injection region. The initial pore pressure at the  
297 injection is set at 3.8 MPa. We impose constant stress and pressure at all boundaries. In terms  
298 of rock properties, the fault zone is assumed weaker than the surrounding formation, with a  
299 Young's modulus of 5 GPa compared to 15 GPa of the host rock. The Poisson's ratio is set to  
300 0.25 in the entire domain. We neglect poroelastic effects by assuming a near-zero Biot's  
301 coefficient (0.001).

302 The permeability of the fault zone is assumed constant at  $10^{-15}$  m<sup>2</sup>, representing a fractured  
303 region within homogeneous granite with permeability set at  $10^{-18}$  m<sup>2</sup>. The injection region at  
304 the center of the model is set as a 1 m<sup>2</sup> patch, with permeability changing as a function of the  
305 normal effective stress (Rinaldi & Rutqvist, 2019). Porosity is set to 1% in the entire domain.  
306 We simulate 24 hours of injection at constant flow rate (0.012 kg/s), simulating a constant  
307 pressure of about 14.5 MPa at the injection point, and allowing fluids to propagate along the  
308 fault. The given pressure is the one observed to be the jacking pressure in several injections at  
309 the BedrettoLab (Bröker et al., 2023). In TOUGH-FLAC, the given conditions would reactivate  
310 the fault within the next numerical time step with a further increase in pressure when assuming  
311 a fault zone with a friction angle of 31°, yielding a static friction coefficient of 0.6 very similar  
312 to the value adopted for dynamic simulations (0.58). Hence, we stop our simulation at the time  
313 step before earthquake nucleation on the fault would occur. The simulated pressure profile  
314 (Figure 1b) is then used as the starting point for the dynamic rupture model and it is considered  
315 representative of key physical conditions during direct injection into a fault zone.

316



317

318 **Figure 1.** 3D dynamic rupture model setup. **(a)** Adopted fault geometry and grid size (50 x  
319 50m), volumetric computational mesh (200 x 200 x 200m) and principal stress orientations. **(b)**  
320 Profile of pore-pressure change of the 25m radius pressurized fault patch (blue line) and on-  
321 plane effective normal stress (black line). The gray bar shows the position of the injection  
322 borehole. **(c)** Spatial profile of the resulting stress parameters after the fluid pressurization.  
323 The peak stress (or static fault strength, black dashed line) and the initial shear stress (black  
324 solid line) are the same for both the class of Models A and B, which differ for the residual  
325 stress level because of the different adopted dynamic friction coefficients (red solid line 0.21  
326 and green solid line 0.15). **(d)** Evolution of the strength parameter S (Eq. 2) for half-fault  
327 dimension for the set of Models A and B (red line and green line, respectively).

328 **3.2. Modeled stress conditions**

329 Figure 1-b shows the pore pressure and normal stress profiles resulting from fluid injection into  
330 the modeled fault patch: the effective normal stress is minimal in the injection zone (gray  
331 shaded bar) and increases along the strike direction as pore pressure decreases.

332 Figure 1c illustrates the spatial distribution of the on-fault stress parameters. The peak stress or  
333 the fault static strength ( $\tau_p = \mu_s \sigma'_n$ ) is shown by a black dashed line and it increases from the  
334 fault center (injection point) towards the fault boundary due to the increase of  $\sigma'_n$  (Figure 1b).  
335 The initial stress (solid black line) is constant over the whole pressurized fault patch. At the  
336 center of the fault, the peak stress is equal to the initial shear stress meaning that the strength  
337 parameter is zero and the rupture can nucleate. The fault portion affected by the nucleation is  
338 represented with the gray bar. The residual shear stress also increases within the fault radius  
339 because of the effective normal stress gradient. It is important to note that all the discussed

340 stress conditions are valid across the different fault directions, implying a radial  
341 parametrization.

342 As anticipated above, we simulate here two sets of models distinguished for the value of the  
343 assumed dynamic friction coefficient: Models A (solid red) dynamic friction is  $\mu_d = 0.21$ , while  
344 in Models B  $\mu_d = 0.15$ . Although peak stress remains similar between Models A and B,  
345 variations in dynamic friction lead to differences in breakdown and dynamic stress drop values,  
346 as well as spatial stress gradients along the fault. The spatial gradient of the effective normal  
347 stress ( $\sigma'_n$ ) also determines the spatial variability of the parameter S (Figure 1d), which is due  
348 to the spatial increment of the strength excess coupled with the reduction in the dynamic stress  
349 drop along the fault radius. This implies a quite different spatial gradient of the strength  
350 parameter S for the two sets of Models (A and B), as shown in Figure 1d for half fault  
351 dimension.

352 As we will discuss in the following, each set of models yields different behaviors of dynamic  
353 rupture propagation for different ranges of the critical slip weakening distance: namely, Models  
354 A yield self-arresting ruptures and Models B runaway ruptures. This confirms that the S  
355 parameter plays a crucial role in the behavior of dynamic rupture propagation for induced  
356 earthquakes. It is worth observing that in our simulation, we intentionally did not include any  
357 additional heterogeneity of the initial stress or other constitutive parameters, because we are  
358 going to focus on the role of pore pressure and effective normal stress ( $\sigma'_n$ ) changes caused by  
359 the fluid injection. In the following we will examine the influence of the S parameter on the  
360 behavior of dynamic rupture propagation and arrest in the context of induced seismicity.

361

### 362 3.3. Rupture nucleation

363 The earthquake nucleation zone is located at the fault injection point by assuming that the fault  
364 strength (initial stress value) equals the peak shear stress, the latter being determined by the  
365 pore-pressure peak caused by fluid injection (see Figure 1). In models of single dynamic  
366 rupture events, we generally adopt the assumption of artificial rupture initiation to enable more  
367 computationally efficient simulations. (Dalguer & Day, 2009; Bizzarri, 2010; Galis et al.,  
368 2015). Indeed, accounting for spontaneous nucleation due to an increasing tectonic loading in  
369 time (Uenishi and Rice, 2003, Rubin and Ampuero, 2005) requires different model  
370 parametrization, a friction law that accounts for the fault strength recovery (i.e., Rate & State  
371 friction law) and different numerical algorithms, e.g., an adaptive time stepping scheme during  
372 the simulation of the full seismic cycle (Lapusta and Liu, 2009) solvers suited for elliptic

373 instead of hyperbolic partial differential equations (Uphoff et al., 2023), which are adopted for  
374 simulations of sequences of earthquakes and aseismic slip (e.g., Barbot et al. 2012; Jiang et al.,  
375 2022 ).

376 In general, a dynamic rupture necessitates to first reach a critical length before spontaneously  
377 growing, leading to an unstable propagation. A relation to estimate the universal critical  
378 nucleation length for homogenous condition of the in-plane crack under slip weakening friction  
379 law has been provided by Uenishi & Rice (2003):

380

381

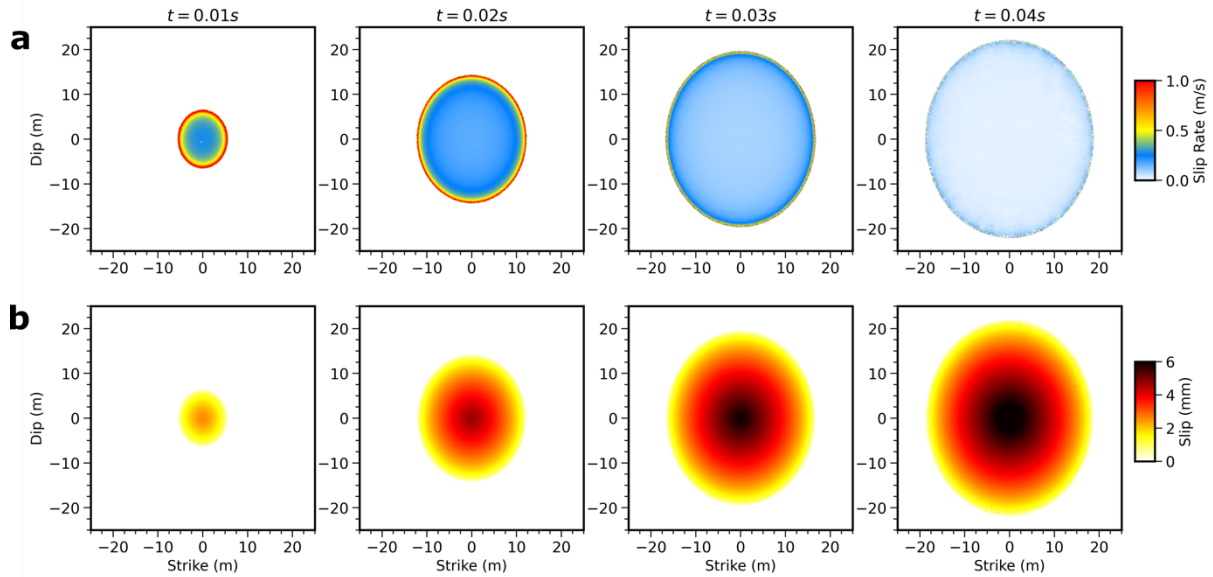
$$l_c = 1.158 \frac{1}{(1-\nu)} \frac{G D_c}{\Delta\tau_b} \quad (3)$$

382 where,  $G$  is the shear modulus,  $\nu$  the Poisson's ratio,  $D_c$  the critical slip weakening distance  
383 and  $\Delta\tau_b$  is the breakdown stress drop.

384 There are two nucleation approaches mainly adopted in the literature for dynamic rupture  
385 simulations: initiation through a time-weakening law where the rupture front velocity is  
386 imposed (Andrews, 1985) or the overstressed patch leading to instantaneous nucleation patch  
387 failure (Kanamori, 1981). This study adopts a slightly modified rupture initiation method,  
388 tailored to the unique stress conditions induced by fluid stimulation and the subsequent  
389 reduction in effective normal stress. We assume a constant time-independent pore pressure  
390 value within the injection zone corresponding to a borehole radius of 1 m and representing the  
391 maximum pressure change (Figure 1b, Section 3.1). This fluid pressure plateau represents the  
392 initial region where the fault strength equals the initial shear stress level, and consequently the  
393 rupture is able to nucleate. To achieve a gradual and smooth increase in fault slip rate at the  
394 hypocenter from  $\sim 10^{-2}$  m/s to typical seismic slip velocity values for dynamic rupture  
395 simulations ( $\sim 10^0$  m/s), we impose a slightly smaller  $D_c = 0.4$  mm within the nucleation patch  
396 for all models. A quantitative formulation which would allow us to estimate the critical size of  
397 the nucleation patch in 3D and under non-homogeneous normal stress conditions is elusive.  
398 We therefore use equation (3) to develop an estimate of the size of the nucleation patch.  
399 Equation 3 predicts a critical nucleation half-length varying between 0.7 and 1.2m due the  
400 variation in breakdown stress drop and the different adopted  $D_c$  values. In agreement with this  
401 estimate, in our simulations the nucleation patch size is adopted from the poro-elastic  
402 simulations protocol of fluid injection (1 m bore hole size), with a nucleation behavior  
403 consistent across all models. The adopted stress and constitutive conditions allow us to  
404 maintain the same nucleation patch size in all our simulations because the fault strength

405 reduction along the source radius is determined by the imposed pore-pressure profile resulting  
406 from poro-elastic modeling.

407



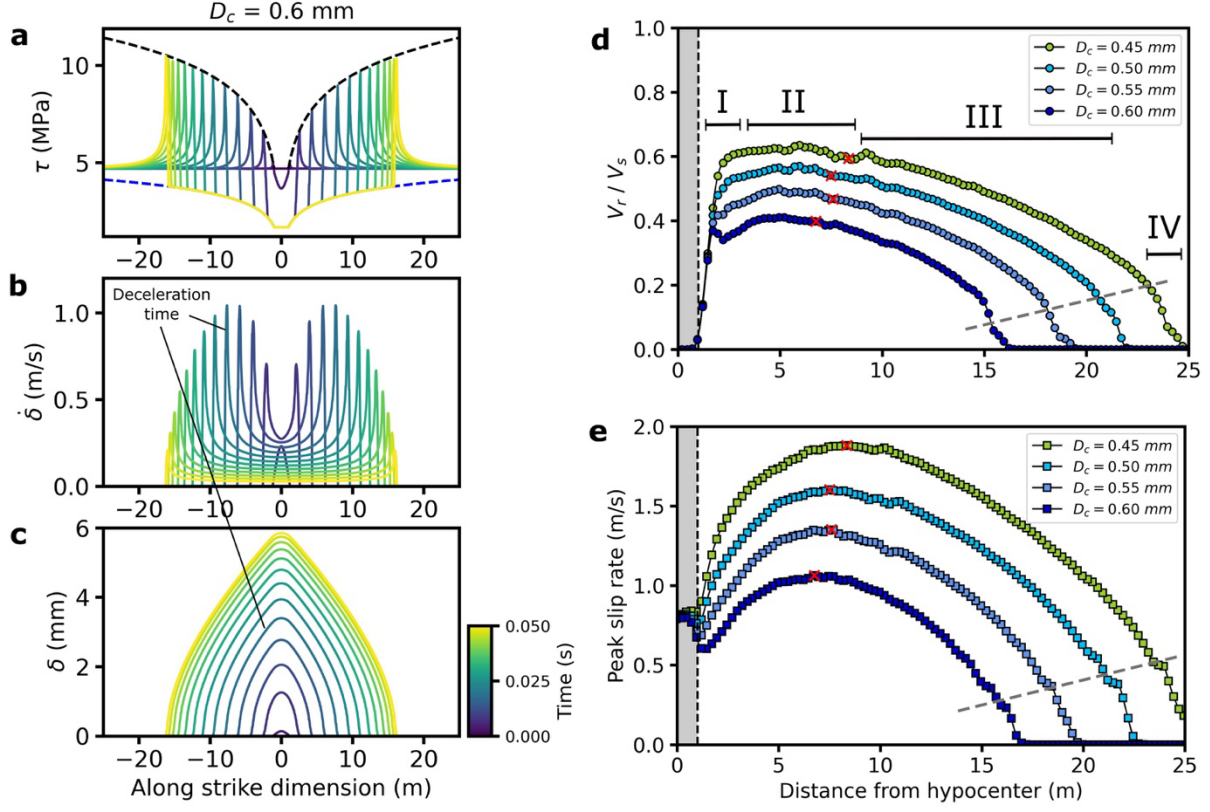
408

409

410 **Figure 2.** Evolution of the dynamic rupture for the model with  $D_c = 0.6\text{ mm}$  belonging to the  
411 class of Models A. **(a)** Snapshots of the slip rate during the rupture propagation. **(b)** Snapshots  
412 of the accrued cumulative slip. Color scales display values of slip rate and slip.

## 413 4. Results

414 We present a series of 3D simulations of the spontaneous propagation of dynamic rupture along  
415 a pressurized fault with a spatial pore pressure profile constrained by poroelastic simulations  
416 aimed at reproducing a stimulation experiment envisioned in the FEAR project. As described  
417 above, the fault geometry and parameterization are taken from the target fault zone of the FEAR  
418 project in the Bedretto underground laboratory (BULGG). We investigate two classes of  
419 Models characterized by different values of the dynamic friction coefficient: Models A have  
420 dynamic friction  $\mu_d$  equal to 0.21, while in Models B  $\mu_d$  is 0.15. For each class of Models we  
421 use different ranges of the critical slip weakening distance. In the following we present the  
422 results of our simulations for each class of Models.



423

424

425 **Figure 3.** Illustration of the set Models A with imposed  $\mu_d = 0.21$  for an along-strike section.  
426 (a-c) Example of rupture evolution through different snapshots of shear stress ( $\tau$ ), slip velocity  
427 ( $\dot{\delta}$ ) and slip profile ( $\delta$ ), the colormap indicates the temporal evolution of the rupture. (d)  
428 Rupture speed and peak slip rate (e) as a function of the hypocentral distance (injection point).  
429 The four stages shown in panel d have been drawn for the model with  $D_c = 0.45$  mm. Red stars  
430 mark the end of phase II, corresponding to the respective maximum in peak slip rate for each  
431 model. Color scale displays temporal evolution in panels a-b-c and adopted  $D_c$  values in panels  
432 d, e.

433

434

#### 4.1. Self-arresting earthquakes

435 We first analyze the set of Models A ( $\mu_d = 0.21$ ) and explore a range of  $D_c$  values ranging from  
436 0.45 mm to 0.6 mm. The dynamic models computed with these parameters are characterized  
437 by self-arresting ruptures, which results in induced earthquakes with  $M_w < 1$ . Figure 2 shows  
438 the evolution of a propagating rupture for a model with  $D_c = 0.6$  mm: Panel (a) displays the  
439 snapshots of slip velocity at different times, while Panel (b) shows the snapshots of cumulative  
440 slip. The slip distribution shown in Panel b resembles those observed in natural earthquakes  
441 and laboratory experiments. (Scholz & Lawer, 2004; Ke et al., 2018). Given the source  
442 parameterization, the rupture propagates with nearly radial symmetry. This symmetry provides

443 a basis for detailed examination of shear stress, slip velocity, and slip evolution along specific  
444 orientations, including the along-strike direction – a focal point of our subsequent analysis.  
445 Figure 3 shows the shear stress, slip velocity and slip evolution with respect to the fault strike  
446 direction during dynamic rupture propagation computed for  $D_c = 0.6$  mm (panels a, b and c,  
447 respectively), which displays the key features of self-arresting ruptures over a source radius of  
448 nearly 15 m. The evolution of shear stress, slip velocity and slip in the along-dip direction is  
449 detailed in the Supplementary Material (Figure S1a, b, c). Comparing Figures 3a-c and S1a-c  
450 confirms that, despite minor differences in rupture velocities, the along-dip results are similar  
451 to those retrieved analyzing propagation along-strike direction. The initial increase of peak slip  
452 velocity is followed by a gradual decrease during the arrest stage resulting in the retrieved  
453 spatial slip gradient. This slip rate behavior implies a crack-like rupture (Kostrov, 1964),  
454 meaning that all points behind the rupture front continue to slip until the rupture arrest. Peak  
455 and residual stress values change with position along the strike because of the variable effective  
456 normal stress (Figure 1).

457 The breakdown stress drop increases during rupture propagation, because the increase of peak  
458 shear stress along the fault radius is larger than the increase of residual stress. Panels d and e  
459 of Figure 3 summarize the behavior of dynamic ruptures for the four simulations conducted  
460 with  $D_c$  ranging from 0.45 mm to 0.6 mm showing the rupture velocity and peak slip rate,  
461 respectively, with respect to half-strike dimension. The vertical gray-shaded bar indicates the  
462 size of the nucleation patch adopted in all simulations, while the red stars identify the points  
463 along the fault where each rupture model reaches its maximum peak slip velocity, (Figure 3 e).  
464 The behavior of rupture velocity and peak slip rate allows us to subdivide the rupture  
465 propagation in four distinct stages (Figure 3d). The first stage (I) corresponds to the initial rapid  
466 acceleration of the rupture front outside the nucleation patch associated with rapidly increasing  
467 peak slip rate. This stage is followed by a propagation at nearly constant rupture velocity  
468 characterized by smoothly increasing peak slip rate reaching its maximum value during  
469 propagation (stage II). At this point, the dynamic rupture starts to decelerate. We have  
470 distinguished two stages during rupture deceleration: stage III is characterized by a continuous  
471 decrease of rupture velocity with a progressive decrease of peak slip rate, followed by stage IV  
472 in which rupture velocity and peak slip velocity abruptly drop to zero. The inferred four stages  
473 describe acceleration, propagation, deceleration, and arrest of dynamic rupture propagation, as  
474 clearly pointed out by the spatial evolution of rupture speed and slip rate.

475 Rupture velocity reaches its maximum value during the initial rupture acceleration (I) in a  
476 relatively small spatial extension; this maximum rupture speed is maintained during the

477 subsequent stage (II) preceding rupture deceleration (in stage III). The spatial extension of  
478 dynamic rupture during these first two stages slightly depends on the adopted  $D_c$  values, while  
479 on the contrary the rupture velocity values depend on the assumed values of the critical slip  
480 weakening distance  $D_c$ : the smaller  $D_c$ , the higher the rupture velocity values characterizing  
481 each simulation. During the acceleration stages (I and II), peak slip velocity continuously  
482 increases up to its maximum value marking the beginning of rupture deceleration. Inferred  
483 peak slip velocity values are inversely proportional to the critical slip weakening distance  $D_c$   
484 (Figure 3 e).

485 Differently from the initial stages (I and II) characterized by rupture acceleration or propagation  
486 at nearly constant speed, the spatial extension of the deceleration stage (III) depends on  $D_c$ : the  
487 larger  $D_c$ , the smaller is the rupture area characterized by rupture deceleration. This implies  
488 that  $D_c$  together with the dynamic friction value control the dimensions of the final ruptured  
489 area and therefore the magnitude of the induced earthquake for self-arresting ruptures. It is  
490 interesting to observe that the rate at which the rupture decelerates appears to be similar among  
491 all models. Finally, all simulations display the arrest phase IV characterized by an abrupt  
492 decrease in both rupture speed and peak slip rate, as indicated by the gray dashed line in Fig.  
493 3d-e. We note that all ruptures stop within the pressurized fault patch, with source radii ranging  
494 from approximately  $\sim 15$  to  $\sim 24$  m. The released moment magnitudes ( $M_w$ ) are 0.76, 0.88, 0.97  
495 and 1, respectively, increasing with decreasing  $D_c$ .

496 A self-arresting rupture generates a nearly triangular shape of the slip spatial profile (Figure 3  
497 c), with a maximum slip of 5.8mm for the adopted  $D_c$  value (0.6 mm). During the initial rupture  
498 acceleration stages (I and II) slip reaches a peak value of  $\sim 3$ mm (at the injection point), as  
499 indicated by lines in Panel b-c highlighting the timestep when deceleration starts (the rupture  
500 front at this point is 6-7 m away from nucleation). This implies that only half of peak slip and  
501 less than half of the rupture extension has been reached during the acceleration of the rupture  
502 (phase I and II), determining a large portion of the seismic moment release during the  
503 deceleration stage (phase III and IV) (see Supplementary Material, Figure S3).

504

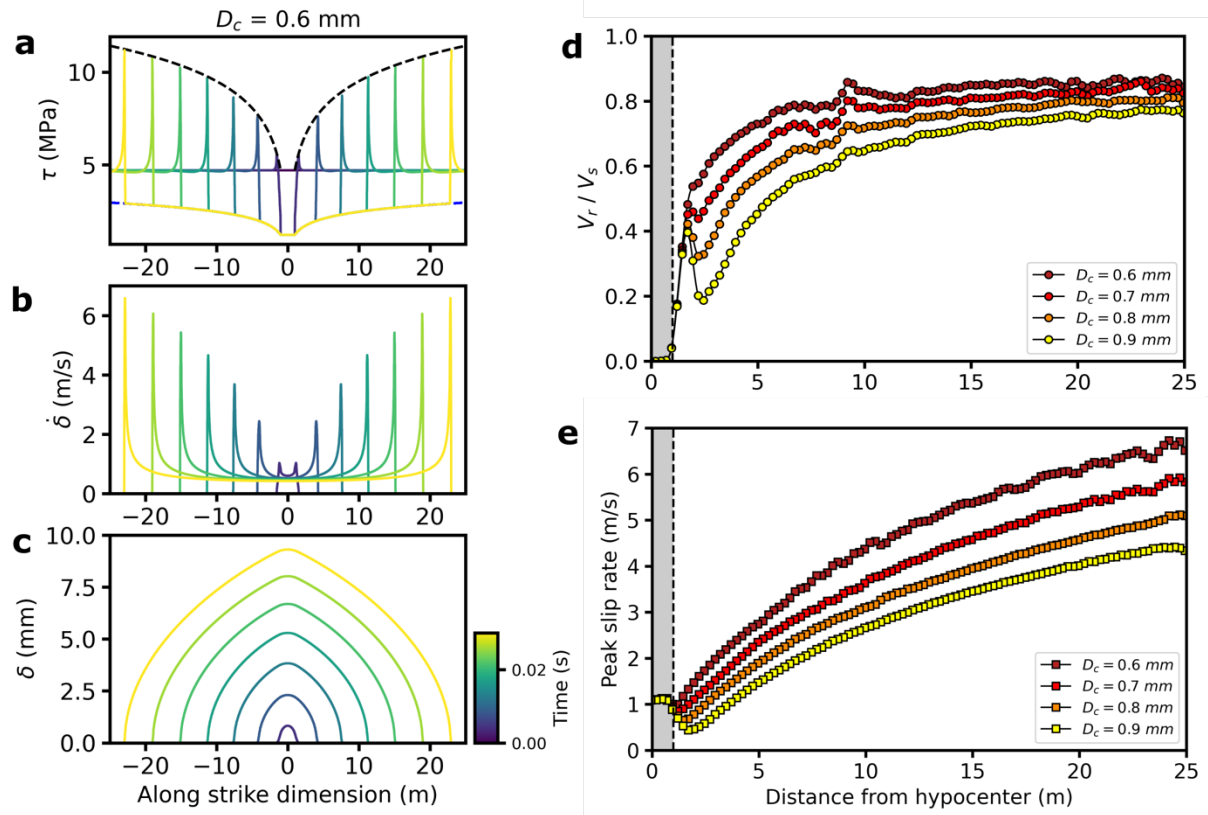
## 505 4.2. Runaway earthquakes

506 It is often assumed (Shapiro et al., 2011; McGarr, 2014) that a rupture remains confined within  
507 the volume affected by the pore pressure change, that is within the pressurized fault patch.  
508 However, if the dynamic load at the crack-tip is sufficiently large to sustain rupture  
509 propagation, the rupture can extend beyond the pressurized patch. This extension enables the

510 rupture to encompass a larger fault area, consequently leading to an earthquake of greater  
511 magnitude. This is the case of the runaway ruptures investigated in this study. As anticipated  
512 above, the class of Models B relies on the assumption of a lower dynamic friction coefficient  
513 (namely,  $\mu_d = 0.15$ ) over the target fault, leading to runaway ruptures propagating outside the  
514 pressurized fault. For this class of Models B, we explored a range of  $D_c$  values ranging from  
515 0.60 mm to 0.90 mm.

516 Figure 4 shows the shear stress, slip velocity and slip evolution along the strike direction  
517 (Panels a, b, c, respectively) for a simulation performed with  $D_c=0.6$  mm, the same  $D_c$  value  
518 used in Figure 3 for self-arresting ruptures (the respective along-dip evolution is shown in  
519 Figure S2). The shear traction evolution displayed in Figure 4a shows the differing increase of  
520 peak and residual stress values with space, resulting in the increase of breakdown stress drop  
521 during the rupture propagation. The spatial increase of the strength parameter S (Figure 1d) is  
522 modest because the increase of strength excess (the same as model A) is counterbalanced by  
523 the larger dynamic stress drop (see equation 2). The peak slip rate continuously increases  
524 during propagation, maintaining a constant residual slip velocity value behind the rupture front  
525 coherently with crack-like ruptures. The maximum peak slip velocity is 6 m/s for this  
526 simulation with  $D_c=0.6$  mm. The slip profiles (elliptical) shown in Panel e are also coherent  
527 with an accelerating crack-like rupture (Gabriel et al., 2012).

528 Figure 4-d and 4-e illustrates how rupture speed and peak slip velocity vary with respect to half  
529 fault strike dimension across different values of the critical slip weakening distance ( $D_c$ ). After  
530 the initial rapid acceleration, the rupture front decelerates with smoothly increasing rupture  
531 velocity remaining within the sub-shear regime. Decreasing the adopted  $D_c$  value results in a  
532 faster acceleration and higher rupture velocities. This is why we explore slightly larger  $D_c$   
533 values in Models B compared to those adopted in Models A, which would otherwise yield  
534 supershear rupture. Peak slip velocity continuously increases during propagation for all the  
535 adopted  $D_c$  values, with the largest peak slip rate values for the smallest  $D_c$ . The rupture  
536 propagates along the whole pressurized patch with an increasing peak slip velocity and without  
537 any deceleration. This characterizes the runaway ruptures. Our simulations suggest that,  
538 regardless of the adopted  $D_c$  value, obtaining a self-arresting rupture is not possible if the  
539 dynamic friction is imposed to 0.15, even when the chosen  $D_c$  value is approximately twice  
540 than that used in the class of Models A. For the set of parameters adopted in Models B, when  
541 rupture nucleates, it always propagates as a runaway rupture front. Rupture arrest for runaway  
542 ruptures occurs only if the rupture encounters a geometrical barrier or an area with unfavorable  
543 stress conditions outside the pressurized patch.



546 **Figure 4.** Illustration of the set Models B with imposed  $\mu_d = 0.15$  for along-strike section. (a-  
547 c) Example of rupture evolution through different snapshots of shear stress ( $\tau$ ), slip velocity  
548 ( $\dot{\delta}$ ) and slip profile ( $\delta$ ). (d) Rupture speed and peak slip rate (e) as a function of the hypocentral  
549 distance (injection point). Color scale displays temporal evolution in panels a-b-c and  $D_c$  values  
550 in panels d, e.

## 552 5. Discussion

553 In this study we have simulated self-arresting and runaway ruptures by stimulating a  
554 pressurized patch through fluid injection within the nucleating zone. Fluid injection maintains  
555 a constant peak of pore-pressure within the nucleation patch (1 m radius), where peak shear  
556 stress  $\tau_p$  is imposed to be equal to the initial stress value. Fluid injection generates a spatial  
557 pore-pressure gradient decreasing towards the edges of the pressurized patch. Since the initial  
558 stress is deliberately maintained as homogeneous across the fault, the resulting spatial gradient  
559 of effective normal stress (Figure 1) causes spatially variable strength excess, breakdown and  
560 dynamic stress drops. Therefore, it is crucial to discuss the factors determining whether a  
561 rupture is self-arresting or runaway, characteristics that directly impact the moment magnitude  
562 of the induced earthquake and the associated seismic hazard.

563        5.1 Fracture energy

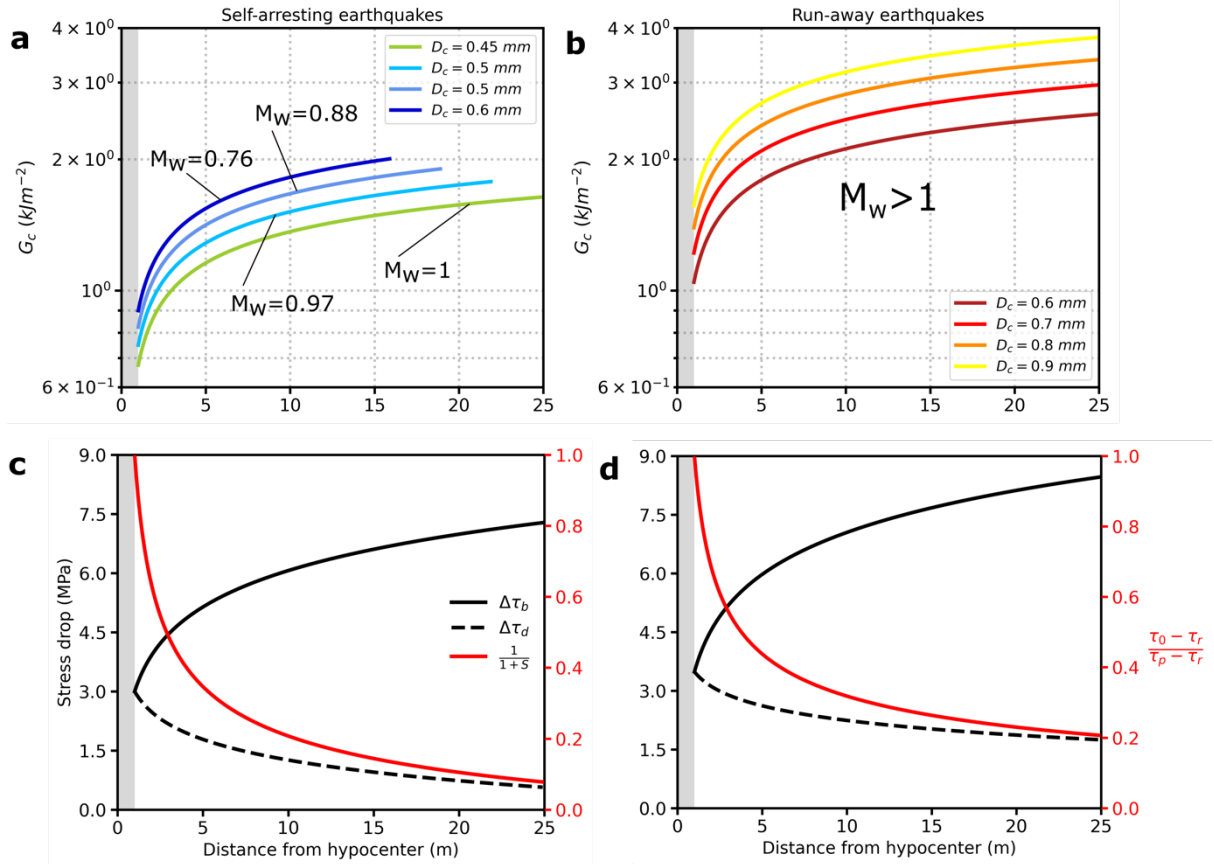
564        Models A and B differ in their dynamic friction coefficients and the range of employed critical  
565        slip weakening distances ( $D_c$ ). It is important to point out that for Models B, which are  
566        characterized by a lower dynamic friction coefficient, all simulated dynamic ruptures are  
567        runaway ruptures for any adopted value of  $D_c$ . On the contrary, for simulations belonging to  
568        Models A, the self-arresting feature disappears if we decrease  $D_c$  below 0.2 mm. To understand  
569        this different behavior, we analyze for each model the fracture energy  $G_c$ , a crucial parameter  
570        to understand earthquake propagation and arrest (Andrews, 1976; Cocco et al., 2023; Gabriel  
571        et al. 2024, Arxiv).

572        For a linear slip-weakening constitutive law,  $G_c$  depends linearly on breakdown stress drop and  
573         $D_c$  (Ida, 1972). Figure 5 shows the spatial evolution of fracture energy for self-arresting (panel  
574        a) and runaway (panel b) ruptures. Runaway ruptures dissipate more energy density (or  
575        breakdown work, Tinti et al., 2005) than self-arresting ruptures. Comparing the simulations  
576        performed with the same  $D_c$  value (0.6 mm) for the two classes of models, the self-arresting  
577        rupture (Models A) dissipates less fracture energy at the rupture front than the runaway rupture  
578        (Models B). This is because breakdown stress drop is larger for runaway ruptures belonging to  
579        the class of Models B (Figure 1b). Therefore, we conclude that self-arresting ruptures are not  
580        caused by a larger energy dissipation at the rupture front (i.e., fracture energy). Panels c) and  
581        d) of Figure 5 show that the decrease in dynamic stress drop for self-arresting ruptures (Models  
582        A) is larger than the one inferred for runaway ruptures (Models B). Furthermore, the increase  
583        in breakdown stress drop is smaller for self-arresting ruptures, and this results in a smaller ratio  
584        between dynamic and breakdown stress drop (i.e.  $1/(1+S)$  in Figure 5 c - d), which is associated  
585        with larger spatial values of the  $S$  parameter (Figure 1). It is important to emphasize that in all  
586        these dynamic models, rupture propagation is associated with spatially variable stress drops  
587        (dynamic and breakdown).

588        Decreasing  $D_c$  for Models A yields runaway ruptures because fracture energy  $G_c$  decreases,  
589        yielding  $G_c$  values much smaller than those inferred for larger  $D_c$  values ( $> 0.4$ ) or for Models  
590        B (see Supplementary Material Figure S4). This implies that within a given class of Models  
591        (i.e., for a given value of dynamic friction coefficient) the dissipated energy determines the  
592        self-arresting or runaway features of the dynamic rupture propagation of the induced  
593        earthquake. However, larger energy dissipation at the rupture front (i.e., fracture energy) is not  
594        sufficient to explain the occurrence of self-arresting ruptures as shown by the comparison  
595        between Panels b and a in Figure 5. More generally, self-arresting rupture depends on the

596 assumed residual stress level, and fracture energy alone does not fully characterize the required  
 597 conditions for self-arresting dynamic ruptures since the strength excess parameter  $S$  is also  
 598 important and it should be considered as well (see Panels 5c and 5d).

599



600

601

602 **Figure 5.** Fracture Energy (i.e., energy dissipation) and stress drop comparison for the two  
 603 sets of Models A and B. **(a-b)** Spatial variation of fracture energy with the distance from the  
 604 hypocenter (injection point) for the set of Models A and B, respectively. The curves for self-  
 605 arresting models (Models A) are interrupted to indicate the arrest points of the ruptures. **(c-d)**  
 606 Spatial variation of stress drops with distance from the hypocenter (injection point) for sets of  
 607 Models A and B, respectively. The black dashed line represents the dynamic stress drop, the  
 608 black solid line depicts the breakdown stress drop, and the red solid line illustrates the ratio  
 609 between these two stress drops, labeled by the  $1/(1+S)$  parameter to link the curve to the  
 610 strength parameter  $S$ .

611

## 5.2 Dynamic load

612 The behavior of peak slip velocity during dynamic propagation (Figures 3 and 4) suggests that  
 613 the differences between self-arresting and runaway ruptures can be interpreted in terms of the  
 614 dynamic load sustaining rupture front propagation. Despite the large dissipation at the rupture  
 615 front (i.e., fracture energy), the dynamic load is much larger for runaway ruptures than for self-

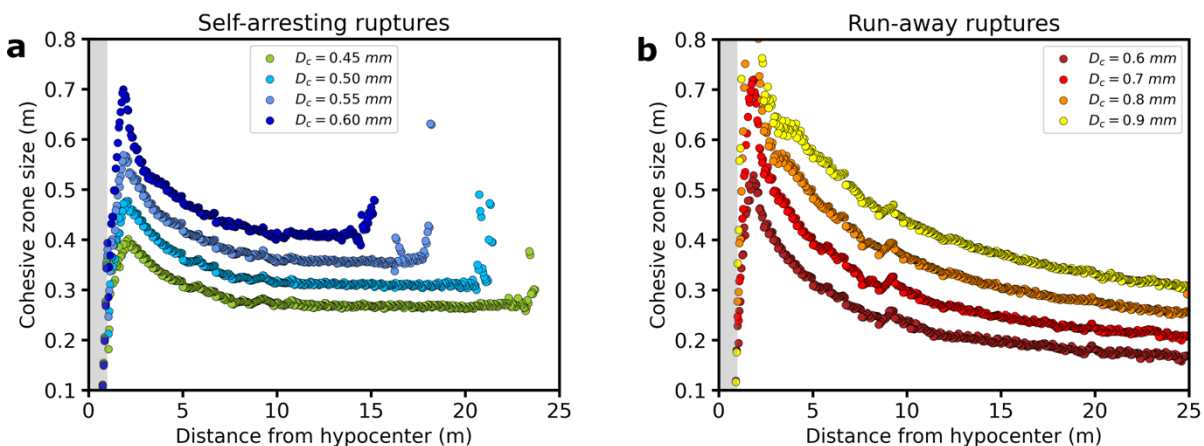
616 arresting ones. A straightforward method to represent the dynamic load at the rupture front is  
 617 computing the shear stress at a given point on the fault, which is a function of slip velocity.  
 618 Fukuyama and Madariaga (1998) proposed the following relationship:

619

$$\sigma(x, t) = -\frac{G}{2\beta} \dot{\delta}(x, t) + \int_{\Sigma} \int_0^t K(x - \xi; t - t') \dot{\delta}(\xi, t') dt' ds \quad (4)$$

620 where  $\beta$  is the shear wave velocity,  $\dot{\delta}(x, t)$  is the slip velocity function and  $K$  is the kernel  
 621 representing the dynamic interaction among those points that are slipping behind the rupture  
 622 front. The integral is computed over the portion of the fault  $\Sigma$  that slipped at time  $t$  in which  
 623 the rupture front has reached the point  $x$  on the fault. Equation (4) highlights that the  
 624 contribution to shear stress at a given point is composed of two terms: an instantaneous  
 625 contribution determined by the slip velocity evolution at that point in space and time (i.e., a  
 626 radiation damping term), and the integral term which represents the dynamic interactions of  
 627 the points on the fault behind the rupture front that are still slipping with decreasing values of  
 628 slip velocity. We can therefore infer that higher slip velocity values are associated with larger  
 629 dynamic load at the rupture tip. This discussion relates to the size of the cohesive zone, which  
 630 is the portion of the fault composed of the points located behind the rupture tip that are  
 631 undergoing dynamic weakening and are expected to have the largest values of slip velocity  
 632 around the peak slip rate. Therefore, they provide the largest contributions to the dynamic  
 633 interactions (the integral term in equation 4) and to the dynamic load at the rupture front.

634



635

636

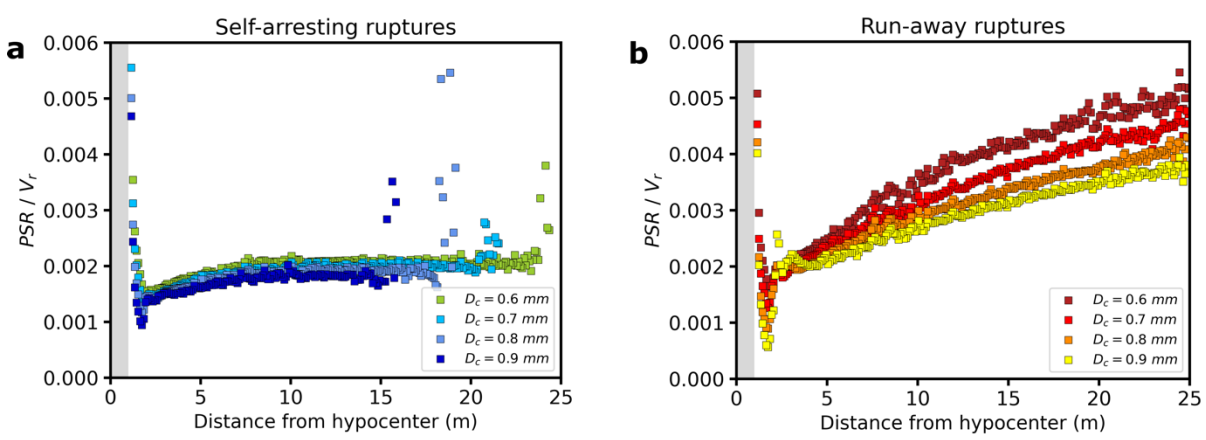
637 **Figure 6.** Cohesive zone behavior for set Models A and B. **(a-b)** The two panels respectively  
 638 show the cohesive zone size with respect to the hypocentral distance (injection point), of the  
 639 self-arresting (set Models A) and runaway ruptures (set Models B).

640

641 Figure 6 shows the cohesive zone sizes for self-arresting (Panel a) and runaway (Panel b)  
 642 ruptures measured for the different ranges of  $D_c$ . The size of the cohesive zone is measured

643 from the breakdown time (i.e., the time window representing the duration of dynamic  
 644 weakening) of each single fault point multiplied by its local rupture speed (Day et al., 2005;  
 645 Wollherr et al., 2018). Across the first 5-7.5 meters of rupture propagation away from the  
 646 nucleation patch the cohesive zone shrinks for both self-arresting and runaway ruptures. This  
 647 is associated with an increase of peak slip velocity and with rupture acceleration following the  
 648 nucleation (Figures 3 and 4). However, for self-arresting ruptures the cohesive zone size  
 649 becomes nearly constant (Figure 6a) as soon as the rupture stops accelerating (stage II in Figure  
 650 3), unlike for runaway ruptures where the cohesive zone size continuously decreases (Figure  
 651 6b and Figure S5). This key observation is associated with the decrease of peak slip velocity  
 652 and rupture velocity (stages III and IV of Figure 3a and b). This corroborates that the size of  
 653 the cohesive zone is linked to both slip velocity and rupture speed evolution during dynamic  
 654 rupture propagation (Day et al., 2005).

655 We next discuss the distinctive features of self-arresting and runaway ruptures by analyzing  
 656 the ratio between peak slip velocity and rupture speed. Figure 7 shows this ratio as a function  
 657 of the distance from the nucleation patch. After an initial stage in which rupture speed increases  
 658 more than peak slip velocity for both model classes (A and B), self-arresting ruptures are  
 659 characterized by a nearly constant ratio between peak slip velocity and rupture speed,  
 660 suggesting that they both decrease during the deceleration phase at the same rate in space. In  
 661 contrast, in runaway ruptures peak slip velocity increases more than rupture speed because the  
 662 shrinking of the cohesive zone decreases due to the reduced rupture acceleration (Figure 6b).  
 663



664  
 665  
 666 **Figure 7.** Peak slip rate variation normalized by the rupture speed for the set of Models A and  
 667 B. **(a-b)** Showing respectively the spatial variation of the ratio between the peak slip rate of the  
 668 rupture and the rupture speed with the hypocentral distance (injection point), for self-arresting  
 669 (set Models A) and runaway ruptures (set Models B).  
 670

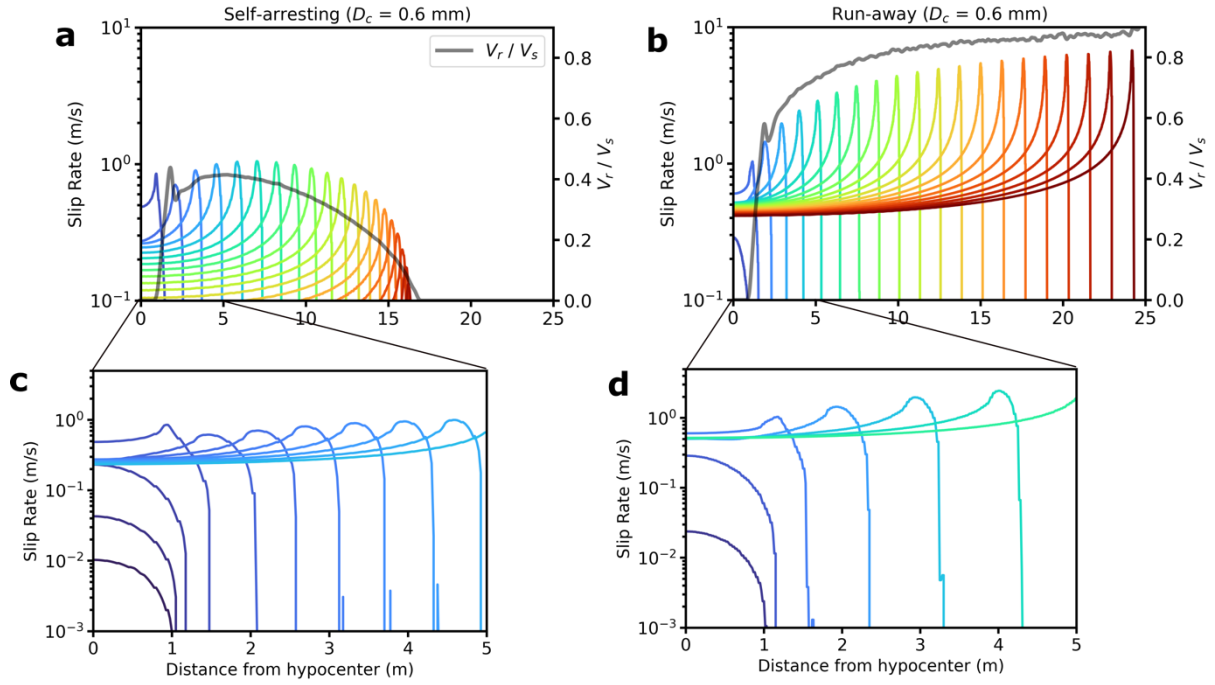
671

672        5.3 The dynamics of decelerating ruptures

673 The spatial gradient of strength excess, breakdown and dynamic stress drop caused by fluid  
674 injection in a pressurized patch determines interesting features for a self-arresting rupture  
675 characterized by a decelerating rupture front propagation over an extended portion of the fault.  
676 Figure 3 shows that the decelerating rupture front propagates over nearly 60% of the radius of  
677 the pressurized patch. The first key feature is the coupling between peak slip velocity and  
678 rupture velocity. This is further investigated in Figure 8 (Panels a and c) showing the slip  
679 velocity time histories and the evolution of rupture velocity in different fault positions along  
680 the strike direction for the simulations with  $D_c = 0.6$  mm. Runaway ruptures are characterized  
681 by an increasing peak slip velocity and rupture speed, with a constant asymptotic residual value  
682 of slip rate, as expected for crack-like models (0.4-0.5 m/s). On the contrary, self-arresting  
683 ruptures show an initial rupture acceleration with increasing peak slip velocities, followed by  
684 a deceleration with decreasing peak slip velocity. Unlike runaway ruptures, self-arresting  
685 ruptures display a decreasing asymptotic residual value of slip rate during the deceleration  
686 stages. This does not occur during the initial acceleration stage of self-arresting rupture. Figure  
687 8 b and d show a zoom of the slip velocity evolution during the first 5 meters from nucleation.  
688 During the initial acceleration stage slip velocity increases for both self-arresting and runaway  
689 ruptures, but the former have smaller values than the latter. Slip velocities for self-arresting  
690 ruptures remain smaller than 1 m/s, differing from runaway ruptures that exceed 1 m/s after a  
691 few meters from nucleation.

692 This analysis yields two main implications. First, it further corroborates that tiny differences in  
693 the residual stress due to the adopted dynamic friction coefficients and the spatial gradient of  
694 normal stress result in spatially variable dynamic stress drop and strength parameter  $S$ ,  
695 determining the self-arresting features. Second, for self-arresting ruptures during the  
696 deceleration stage, the asymptotic residual slip velocity value decreases during dynamic  
697 propagation approaching zero. This implies that during rupture deceleration and arrest, a crack-  
698 like model becomes a pulse like rupture, without exhibiting any stress undershoot (Lambert et  
699 al. 2021), encountering any fault width barrier (Weng & Ampuero, 2019), or facing bi-material  
700 contrast (Ampuero & Ben-Zion, 2008).

701



702  
703  
704  
705  
706  
707  
708  
709  
710  
711

**Figure 8.** Evolution of slip rate and rupture speed for two example ruptures with the same  $D_c$  (0.6mm) in the sets of Models A and B. Panels (a-c) display the slip rate evolution at different timesteps, indicated by the colormap, and the evolution of the rupture speed depicted by the gray solid line, for self-arresting (set Models A) and run-away (set Models B) ruptures, respectively. (b-d) Zooming in on the initial 5 meters of the rupture extension to emphasize the evolution of the slip rate during nucleation and the initial acceleration outside the nucleation patch.

712  
713  
714  
715  
716  
717  
718  
719  
720

#### 5.4 Implications for earthquake mechanics

721 Although the stress conditions modeled in this work are carefully selected, we believe that they  
722 are representative of fluid pressurization on a relatively homogeneous fault. While initial stress  
723 heterogeneity is a common condition to model dynamic ruptures on active faults (Ripperger et  
724 al., 2007; Ma et al. 200; Tago et al. 2012; Tinti et al., 2021; among many others), we believe  
725 that simulating dynamic propagation for a stress configuration characterized by a relatively  
726 smooth spatial gradient is of interest for studying induced seismicity. The results obtained in  
727 this work highlight distinct dynamic aspects of a decelerating rupture front that deserve to be  
728 further investigated under a wider range of initial conditions.

729 Notably, in our simulations the residual stress level (i.e., dynamic stress) is not constant in  
730 space and exhibits spatial gradients due to the effective normal stress changes induced by pore  
731 pressure perturbations. This is different from the conditions commonly adopted in linear elastic  
732 fracture mechanics (Galis et al., 2017; Brener and Bouchbinder, 2021; Kammer et al., 2024).

725 In particular, while runaway ruptures characterized by a dynamic propagation at increasing or  
726 nearly constant rupture velocity (i.e., without deceleration) are coherent with crack-like  
727 models, in which slip velocity evolves from its peak to an invariant residual value, self-arresting  
728 ruptures characterized by the propagation of a decelerating rupture front over an extended fault  
729 dimension exhibit unconventional features not completely coherent with pure crack-like  
730 models (as evidenced by the decreasing residual slip velocity values behind the decelerating  
731 rupture front). This feature represents a deviation from predictions from linear elastic fracture  
732 mechanics, and it is not usually observed in dynamic simulations with linear slip weakening  
733 law and heterogeneous prestress. It is worth noting that in our dynamic simulations we do not  
734 prescribe the Griffith energy balance at the crack tip (Freund, 1989; Galis et al., 2017; Kammer  
735 et al., 2024), for which the energy release rate (energy flow at the crack-tip) is equal to the  
736 fracture energy (i.e., the energy dissipated at the rupture front). In other words, we do not  
737 assume that the energy flow is equal to the dissipated energy at the rupture tip. Indeed, the  
738 solution of the 3D dynamic rupture propagation is obtained by assuming the constitutive law  
739 (the linear slip weakening in our case) and the collinearity between slip velocity and shear  
740 traction. This explains why self-arresting ruptures are not uniquely characterized by larger  
741 energy dissipation at the rupture tip; rather, the larger spatial decrease of dynamic stress drop  
742 (as mapped by spatial gradient of the strength parameter  $S$ ) determines self-arresting features.

## 743 6. Conclusions

744 In this paper we have performed a series of 3D simulations to model the dynamic rupture of a  
745 pressurized patch stimulated through fluid injection within the nucleation zone. To our  
746 knowledge, these represent the first dynamic rupture simulations for an induced micro-  
747 earthquake on a decametric-scale planar fault (50 m length). Previously, only Liu and Lapusta  
748 (2008) modeled a  $\sim 2$  magnitude micro-earthquake repeater of the San Andreas Fault through  
749 3D seismic cycle simulation. The fault geometry and the pore fluid pressure changes have been  
750 modeled to reproduce the stimulation experiments envisioned by the FEAR project in the  
751 Bedretto Lab (BULGG). In particular, the pore pressure profile along the fault radius and  
752 around the injection borehole has been computed through poro-elastic simulation of the fault  
753 zone. The initial stress is kept constant to investigate the role of the spatial gradient of effective  
754 normal stress. The two classes of models simulated in this study differ in their values of the  
755 dynamic friction coefficient and in the range of their values of the critical slip weakening  
756 distance. Models B have a smaller dynamic friction coefficient ( $\mu_d = 0.15$ ) and larger  $D_c$  values

757 ranging from 0.60 mm to 0.90 mm. They result in runaway ruptures propagating over the entire  
758 pressurized patch, without any deceleration of the rupture front. This behavior is obtained also  
759 using smaller values of the critical slip weakening distance  $D_c$ , which have not been discussed  
760 because they yield supershear ruptures. On the contrary, Models A, characterized by a higher  
761 dynamic friction coefficient ( $\mu_d = 0.21$ ) and smaller  $D_c$  values ranging from 0.45 mm to 0.60  
762 mm, display self-arresting rupture within the pressurized patch. Decreasing  $D_c$  for this class of  
763 Models A would yield runaway ruptures.

764 The results of this study are of relevance to discuss the dynamic propagation of rupture during  
765 an induced earthquake characterized by a spatially variable, continuously increasing effective  
766 normal stress governed by the pore fluid pressurization of the fault patch. This causes spatially  
767 variable peak and residual stress values, which result in a spatially variable strength excess,  
768 breakdown and dynamic stress drops. In this configuration, decreasing the residual stress by  
769 changing the dynamic coefficient of friction makes the fault more unstable, yielding runaway  
770 ruptures for a broad range of  $D_c$  values. This results in generating smooth, spatially variable  
771 frictional strength, as described by the spatial evolution of the S parameter. While this is  
772 expected, a tiny increase of the dynamic friction coefficient, which is still representative of a  
773 weak fault ( $\mu_d \approx 0.2$ ), can generate self-arresting ruptures characterized by a large spatial  
774 increase (gradient) of the S parameter caused by the spatial decrease in dynamic stress drop. In  
775 this configuration, we have found a range of  $D_c$  values for which self-arresting ruptures are  
776 characterized by the propagation of a decelerating rupture front over a finite portion of the  
777 pressurized patch. Self-arresting ruptures do not reach the edge of the pressurized patch, unlike  
778 runaway ruptures.

779 Our simulations corroborate that self-arresting and runaway ruptures are determined by the  
780 stress state within the pressurized patch. However, the analysis of the dynamics of a  
781 decelerating propagating rupture yields interesting and somehow surprising results.

782 We have shown that the distinction between self-arresting and runaway ruptures cannot be  
783 explained solely in terms of fracture energy (i.e., the energy dissipated at the rupture front);  
784 that is, ruptures are not self-arresting because they dissipate more energy at the tip. Runaway  
785 ruptures dissipate more energy than self-arresting ones, even if decreasing fracture energy (by  
786 decreasing  $D_c$ ) transforms self-arresting ruptures into runaway ones. The spatial variation of  
787 frictional strength caused by the spatially increasing normal stress within the pressurized patch  
788 is the key feature to enable self-arresting, because it is determining the dynamic load sustaining  
789 the propagation of the rupture front. Indeed, the behavior of slip velocity, rupture speed and

790 cohesive zone size suggests that dynamic load, supporting rupture front propagation, is larger  
791 for runaway ruptures. On the contrary, we can conclude that for self-arresting ruptures the  
792 dynamic load is not large enough to maintain the dynamic rupture propagation causing rupture  
793 deceleration associated with a nearly constant size of the cohesive zone and decreasing peak  
794 slip velocity values until the final rupture arrest. The peculiar feature of this dynamic  
795 propagation is the spatially variable dynamic stress drop and strength excess.

796 The dynamic propagation of an induced self-arresting rupture over a finite extension of the  
797 pressurized patch generates a slip velocity field that differs from that obtained for runaway  
798 ruptures, characterized by the propagation at constant or increasing rupture speed. The most  
799 evident feature is the decrease of peak slip velocity associated with the decelerating rupture  
800 and the nearly constant cohesive zone size. The other relevant feature is the decrease of the  
801 residual slip velocity value (asymptotic value for a crack-like rupture), which decreases during  
802 deceleration becoming nearly zero. This means that the initial crack-like rupture retrieved  
803 during the acceleration stage becomes a pulse-like rupture at the arrest.

804 The results of this study, obtained under specific stress conditions, are applied to a realistic  
805 scenario of an induced earthquake at BULGG. Nonetheless, they allow us to highlight how the  
806 study of the rupture dynamics of an induced earthquake involves peculiarities relevant to the  
807 mechanics of earthquakes. The spatially variable normal stress causes variations of frictional  
808 strength and spatially variable breakdown and dynamic stress drops. This might have  
809 implications for radiated energy and frequency contents of ground motions caused by induced  
810 earthquakes. Although further investigations are needed to account for prestress heterogeneity,  
811 we emphasize the importance of exploring rupture deceleration over a finite portion of a  
812 pressurized patch.

813  
814

## 815 **Acknowledgements**

816 This study has received funding from the European Research Council (ERC) under the  
817 European Union's Horizon 2020 research and innovation programme (grant agreement No  
818 856559). MC participated in this work as Principal Investigator of the European Research  
819 Council (ERC) project FEAR (grant agreement No 856559) under the European Community's  
820 Horizon 2020 Framework Programme. FM, LDZ, APL and ET also participated in this work  
821 in the framework of the European Research Council (ERC) project FEAR (grant agreement No  
822 856559) under the European Community's Horizon 2020 Framework Programme.

823 AAG acknowledges additional support by the European Union's Horizon 2020 research and  
824 innovation program (TEAR ERC Starting; grant no. 852992) and Horizon Europe (ChEESE-

825 2P, grant no. 101093038; DT-GEO, grant no. 101058129; and Geo-INQUIRE, grant no.  
826 101058518), the National Science Foundation (grant nos. EAR-2225286, EAR-2121568,  
827 OAC-2139536, OAC-2311208), and the National Aeronautics and Space Administration  
828 (grant no. 80NSSC20K0495).

829 We thank Ravil Dorozhinskii, Thomas Ulrich and the SeisSol team (see [www.seissol.org](http://www.seissol.org)).  
830 We acknowledge the CINECA award under the ISCRA initiative, for the availability of high-  
831 performance computing resources and support.

832

## 833 **Open Research**

834 We use the SeisSol software package available on GitHub (<https://github.com/SeisSol/SeisSol>)  
835 to simulate all dynamic models. We use SeisSol, version {202103\\_\\_Sumatra-686-gf8e01a54}  
836 (master branch on commit dd018b3398258a23ec2a33c74bd7f31b503dcca6, v1.1.3-362-  
837 gdd018b33). The procedure to download and run the code is described in the SeisSol  
838 documentation ([seissol.readthedocs.io/en/latest/](https://seissol.readthedocs.io/en/latest/)). Downloading and compiling instructions are  
839 at <https://seissol.readthedocs.io/en/latest/compiling-seissol.html>. Instructions for setting up and  
840 running simulations are at <https://seissol.readthedocs.io/en/latest/configuration.html>.  
841 Quickstart containerized installations and introductory materials are provided in the docker  
842 container and Jupyter Notebooks at {<https://github.com/SeisSol/Training>. Example problems  
843 and model configuration files are provided at <https://github.com/SeisSol/Examples>, many of  
844 which reproduce the SCEC 3D Dynamic Rupture benchmark problems described at  
845 [https://strike.scec.org/cvws/benchmark\\_descriptions.html](https://strike.scec.org/cvws/benchmark_descriptions.html).

846 All data required to reproduce the dynamic rupture scenarios are available at ... .

847 The data will be fully archived at Zenodo at acceptance.

848

849 **References**

850

851 Abercrombie, R. E. (1995). Earthquake source scaling relationships from– 1 to 5 ML using  
852 seismograms recorded at 2.5-km depth. *Journal of Geophysical Research: Solid Earth*.

853

854 Abercrombie, R. E. (2021). Resolution and uncertainties in estimates of earthquake stress drop  
855 and energy release. *Philosophical Transactions of the Royal Society A*.

856

857 Abercrombie, R. E., & Rice, J. R. (2005). Can observations of earthquake scaling constrain slip  
858 weakening?. *Geophysical Journal International*.

859

860 Achtziger-Zupančič, Peter & Ceccato, Alberto & Zappone, Alba & Pozzi, Giacomo & Shakas,  
861 Alexis & Amann, Florian & Behr, Whitney & Botero, Daniel & Giardini, Domenico &  
862 Hertrich, Marian & Jalali, Mohammadreza & Ma, Xiaodong & Meier, Men-Andrin & Osten,  
863 Julian & Wiemer, Stefan & Cocco, Massimo. (2024). Selection and Characterisation of the  
864 Target Fault for Fluid-Induced Activation and Earthquake Rupture Experiments.  
865 10.5194/egusphere-2024-586.

866

867 Ampuero, J. P., & Ben-Zion, Y. (2008). Cracks, pulses and macroscopic asymmetry of  
868 dynamic rupture on a bimaterial interface with velocity-weakening friction. *Geophysical  
869 Journal International*, 173(2), 674-692.

870

871 Andrews, D. J. (1976). Rupture velocity of plane strain shear cracks. *Journal of Geophysical  
872 Research*, 81(32), 5679-5687.

873

874 Andrews, D. J. (1985). Dynamic plane-strain shear rupture with a slip-weakening friction law  
875 calculated by a boundary integral method. *Bulletin of the Seismological Society of America*,  
876 75(1), 1-21.

877

878 Allmann, B. P., & Shearer, P. M. (2007). Spatial and temporal stress drop variations in small  
879 earthquakes near Parkfield, California. *Journal of Geophysical Research: Solid Earth*.

880

881 Allmann, B. P., & Shearer, P. M. (2009). Global variations of stress drop for moderate to large  
882 earthquakes. *Journal of Geophysical Research: Solid Earth*.

883

884 Bai, K., & Ampuero, J. P. (2017). Effect of seismogenic depth and background stress on  
885 physical limits of earthquake rupture across fault step overs. *Journal of Geophysical Research: Solid  
886 Earth*, 122(12), 10-280.

887

888 Barbot, S., Lapusta, N., & Avouac, J. P. (2012). Under the hood of the earthquake machine:  
889 Toward predictive modeling of the seismic cycle. *Science*, 336(6082), 707-710.

890

891 Barras, F., Thøgersen, K., Aharonov, E., & Renard, F. (2023). How do earthquakes stop?  
892 Insights from a minimal model of frictional rupture. *Journal of Geophysical Research: Solid  
893 Earth*, 128(8), e2022JB026070.

894

895 Biemiller, J., Gabriel, A. A., & Ulrich, T. (2023). Dueling dynamics of low-angle normal fault  
896 rupture with splay faulting and off-fault damage. *Nature Communications*, 14(1), 2352.

897

898 Bizzarri, A. (2010). How to promote earthquake ruptures: Different nucleation strategies in a  
899 dynamic model with slip-weakening friction. *Bulletin of the Seismological Society of America*,  
900 100(3), 923-940.

901

902 Bolton, D. C., Affinito, R., Smye, K., Marone, C., & Hennings, P. (2023). Frictional and  
903 poromechanical properties of the Delaware Mountain Group: Insights into induced seismicity  
904 in the Delaware Basin. *Earth and Planetary Science Letters*, 623, 118436.

905

906 Brener, E. A., & Bouchbinder, E. (2021). Unconventional singularities and energy balance in  
907 frictional rupture. *Nature communications*, 12(1), 2585.

908

909 Bröker, K., & Ma, X. (2022). Estimating the least principal stress in a granitic rock mass:  
910 systematic mini-frac tests and elaborated pressure transient analysis. *Rock Mechanics and*  
911 *Rock Engineering*, 55(4), 1931-1954.

912

913 Bröker, K., X. Ma, N. Gholizadeh Doonechaly, A. P. Rinaldi, M. Hertrich, A. Obermann, V.  
914 Clasen Repolles, S. Wiemer, D. Giardini, H. Maurer (2023). Hydro-geomechanical  
915 observations during multistage hydraulic stimulation at the Bedretto Underground Laboratory,  
916 Switzerland. In: *Proceedings of the 57th US Rock Mechanics/Geomechanics Symposium*,  
917 Atlanta, Georgia, USA.

918

919 Candela, T., Wassing, B., Ter Heege, J., & Buijze, L. (2018). How earthquakes are induced.  
920 *Science*, 360(6389), 598-600.

921

922 Cappa, F., Scuderi, M. M., Collettini, C., Guglielmi, Y., & Avouac, J. P. (2019). Stabilization  
923 of fault slip by fluid injection in the laboratory and in situ. *Science advances*, 5(3), eaau4065.

924

925 Cebry, S. B. L., Ke, C. Y., & McLaskey, G. C. (2022). The Role of Background Stress State in  
926 Fluid-Induced Aseismic Slip and Dynamic Rupture on a 3-m Laboratory Fault. *Journal of*  
927 *Geophysical Research: Solid Earth*, 127(8), e2022JB024371.

928

929 Ciardo, F., & Rinaldi, A. P. (2022). Impact of injection rate ramp-up on nucleation and arrest  
930 of dynamic fault slip. *Geomechanics and Geophysics for Geo-Energy and Geo-Resources*,  
931 8(1), 28.

932

933 Cocco, M., & Rice, J. R. (2002). Pore pressure and poroelasticity effects in Coulomb stress  
934 analysis of earthquake interactions. *Journal of Geophysical Research: Solid Earth*, 107(B2),  
935 ESE-2.

936

937 Cocco, M., Tinti, E., & Cirella, A. (2016). On the scale dependence of earthquake stress drop.  
938 *Journal of Seismology*.

939

940 Cornet, F. H. (2012). The relationship between seismic and aseismic motions induced by forced  
941 fluid injections. *Hydrogeology journal*, 20(8), 1463.

942

943 Cornet, F. H. (2016). Seismic and aseismic motions generated by fluid injections.  
944 *Geomechanics for Energy and the Environment*, 5, 42-54.

945

946 Das, S., & Aki, K. (1977). Fault plane with barriers: A versatile earthquake model. *Journal of*  
947 *geophysical research*, 82(36), 5658-5670.

948

949 Dalguer, L. A., & Day, S. M. (2009). Asymmetric rupture of large aspect-ratio faults at  
950 bimaterial interface in 3D. *Geophysical Research Letters*, 36(23).

951

952 Dal Zilio, L., Hegyi, B., Behr, W., & Gerya, T. (2022). Hydro-mechanical earthquake cycles  
953 in a poro-visco-elasto-plastic fluid-bearing fault structure. *Tectonophysics*, 838, 229516.

954

955 Dumbser, M., & Käser, M. (2006). An arbitrary high-order discontinuous Galerkin method for  
956 elastic waves on unstructured meshes—II. The three-dimensional isotropic case. *Geophysical  
957 Journal International*, 167(1), 319-336.

958

959 Ellsworth, W. L. (1995). Seismic evidence for an earthquake nucleation phase. *Science*.

960

961 Ellsworth, W. L. (2013). Injection-induced earthquakes. *Science*, 341(6142), 1225942.

962

963 Fukuyama, E., & Madariaga, R. (1998). Rupture dynamics of a planar fault in a 3D elastic  
964 medium: rate-and slip-weakening friction. *Bulletin of the Seismological Society of America*.

965

966 Gabriel, A. A., Ampuero, J. P., Dalguer, L. A., & Mai, P. M. (2012). The transition of dynamic  
967 rupture styles in elastic media under velocity-weakening friction. *Journal of Geophysical  
968 Research: Solid Earth*, 117(B9).

969

970 Gabriel, A. A., Garagash, D. I., Palgunadi, K. H., & Mai, P. M. (2023). Fault-size dependent  
971 fracture energy explains multi-scale seismicity and cascading earthquakes. *arXiv preprint  
972 arXiv:2307.15201*.

973

974 Gabriel, A. A., Ulrich, T., Marchandon, M., Biemiller, J., & Rekoske, J. (2023). 3D Dynamic  
975 Rupture Modeling of the 6 February 2023, Kahramanmaraş, Turkey M w 7.8 and 7.7  
976 Earthquake Doublet Using Early Observations. *The Seismic Record*, 3(4), 342-356.

977

978 Galis, M., Ampuero, J. P., Mai, P. M., & Cappa, F. (2017). Induced seismicity provides insight  
979 into why earthquake ruptures stop. *Science advances*.

980

981 Galis, M., Ampuero, J. P., Mai, P. M., & Kristek, J. (2019). Initiation and arrest of earthquake  
982 ruptures due to elongated overstressed regions. *Geophysical Journal International*, 217(3),  
983 1783-1797.

984

985 Garagash, D. I., & Germanovich, L. N. (2012). Nucleation and arrest of dynamic slip on a  
986 pressurized fault. *Journal of Geophysical Research: Solid Earth*, 117(B10).

987

988 Geubelle, P. H., & Kubair, D. V. (2001). Intersonic crack propagation in homogeneous media  
989 under shear-dominated loading: numerical analysis. *Journal of the Mechanics and Physics of  
990 Solids*, 49(3), 571-587.

991

992 Guglielmi, Y., Cappa, F., Avouac, J. P., Henry, P., & Elsworth, D. (2015). Seismicity triggered  
993 by fluid injection–induced aseismic slip. *Science*, 348(6240), 1224-1226.

994

995 Grigoli, F., Cesca, S., Priolo, E., Rinaldi, A. P., Clinton, J. F., Stabile, T. A., ... & Dahm, T.  
996 (2017). Current challenges in monitoring, discrimination, and management of induced  
997 seismicity related to underground industrial activities: A European perspective. *Reviews of  
998 Geophysics*, 55(2), 310-340.

999

1000 Grigoli, F., Cesca, S., Rinaldi, A. P., Manconi, A., López-Comino, J. A., Clinton, J. F., et al.  
1001 (2018). The November 2017 Mw 5.5 Pohang earthquake: A possible case of induced seismicity  
1002 in South Korea. *Science*.

1003

1004 Harris, R. A. (2017). Large earthquakes and creeping faults. *Reviews of Geophysics*, 55(1),  
1005 169-198.

1006

1007 Harris, R. A., Barall, M., Aagaard, B., Ma, S., Roten, D., Olsen, K., ... & Dalguer, L. (2018).  
1008 A suite of exercises for verifying dynamic earthquake rupture codes. *Seismological Research  
1009 Letters*, 89(3), 1146-1162.

1010

1011 Hunfeld, L. B., Chen, J., Niemeijer, A. R., Ma, S., & Spiers, C. J. (2021). Seismic slip-pulse  
1012 experiments simulate induced earthquake rupture in the Groningen gas field. *Geophysical  
1013 Research Letters*, 48(11), e2021GL092417.

1014

1015 Hubbert, M., & Rubey, W. W. (1959). Role of fluid pressure in mechanics of overthrust  
1016 faulting. *Geological Society of America Bulletin*.

1017

1018 Ida, Y. (1972). Cohesive force across the tip of a longitudinal-shear crack and Griffith's  
1019 specific surface energy, *J. Geophys. Res.*, 77.

1020

1021 Imanishi, K., & Ellsworth, W. L. (2006). Source scaling relationships of microearthquakes at  
1022 Parkfield, CA, determined using the SAFOD pilot hole seismic array. Washington DC  
1023 American Geophysical Union Geophysical Monograph Series.

1024

1025 Jiang, J., Erickson, B. A., Lambert, V. R., Ampuero, J. P., Ando, R., Barbot, S. D., ... & van  
1026 Dinther, Y. (2022). Community-driven code comparisons for three-dimensional dynamic  
1027 modeling of sequences of earthquakes and aseismic slip. *Journal of Geophysical Research: Solid Earth*, 127(3), e2021JB023519.

1029

1030 Kame, N., & Yamashita, T. (1999). A new light on arresting mechanism of dynamic earthquake  
1031 faulting. *Geophysical research letters*, 26(13), 1997-2000.

1032

1033 Kammer, D. S., McLaskey, G. C., Abercrombie, R. E., Ampuero, J. P., Cattania, C., Cocco,  
1034 M., ... & Tinti, E. (2024). Energy dissipation in earthquakes. arXiv preprint arXiv:2403.06916.

1035

1036 Kanamori, H. (1981). The nature of seismicity patterns before large earth-quakes, in  
1037 Earthquake Prediction—An International Review.

1038

1039 Kanamori, H. (2003). Earthquake prediction: An overview. *International Geophysics*, 81,  
1040 1205-1216.

1041

1042 Ke, C. Y., McLaskey, G. C., & Kammer, D. S. (2018). Rupture termination in laboratory-  
1043 generated earthquakes. *Geophysical Research Letters*, 45(23), 12-784.

1044

1045 Ke, C. Y., McLaskey, G. C., & Kammer, D. S. (2022). Earthquake breakdown energy scaling  
1046 despite constant fracture energy. *Nature communications*, 13(1), 1005.

1047

1048 Kieranen, K. M., Savage, H. M., Abers, G. A., \& Cochran, E. S. (2013). Potentially induced  
1049 earthquakes in Oklahoma, USA: Links between wastewater injection and the 2011 Mw 5.7  
1050 earthquake sequence. *Geology*.

1051

1052 Kim, K.-H., Ree, J.-H., Kim, Y., Kim, S., Kang, S. Y., \& Seo, W. (2018). Assessing whether  
1053 the 2017 M w 5.4 Pohang earthquake in South Korea was an induced event. *Science*.

1054

1055 Kostrov, B. V. (1964). Self-similar problems of propagation of shear cracks. *Journal of Applied  
1056 Mathematics and Mechanics*, 28(5), 1077-1087.

1057 Lapusta, N., \& Liu, Y. (2009). Three-dimensional boundary integral modeling of spontaneous  
1058 earthquake sequences and aseismic slip. *Journal of Geophysical Research: Solid Earth*,  
1059 114(B9).

1060

1061 Larochelle, S., Lapusta, N., Ampuero, J. P., \& Cappa, F. (2021). Constraining fault friction and  
1062 stability with fluid-injection field experiments. *Geophysical Research Letters*, 48(10),  
1063 e2020GL091188.

1064

1065 Lee, K. K., Ellsworth, W. L., Giardini, D., Townend, J., Ge, S., Shimamoto, T., ... \&  
1066 Langenbruch, C. (2019). Managing injection-induced seismic risks. *Science*, 364(6442), 730-  
1067 732.

1068

1069 Lesko, K.: The Sanford Underground Research Facility at Homestake (SURF), *Physics  
1070 Procedia*, 61, 542–551.

1071

1072 Liu, L. and Zoback, M. D.: The effect of topography on the state of stress in the crust:  
1073 application to the site of the Cajon Pass Scientific Drilling Project, *J. Geophys. Res.*

1074

1075 Liu, Y., & Lapusta, N. (2008). Transition of mode II cracks from sub-Rayleigh to intersonic  
1076 speeds in the presence of favorable heterogeneity. *Journal of the Mechanics and Physics of  
1077 Solids*, 56(1), 25-50.

1078

1079 Lui, S. K., & Lapusta, N. (2018). Modeling high stress drops, scaling, interaction, and  
1080 irregularity of repeating earthquake sequences near Parkfield. *Journal of Geophysical  
1081 Research: Solid Earth*, 123(12), 10-854.

1082

1083 Ma, X., Hertrich, M., Amann, F., Bröker, K., Gholizadeh Doonechaly, N., Gischig, V., ... \&  
1084 Giardini, D. (2022). Multi-disciplinary characterizations of the Bedretto Lab a new  
1085 underground geoscience research facility. *Solid Earth*.

1086

1087 Ma, S., Custódio, S., Archuleta, R. J., & Liu, P. (2008). Dynamic modeling of the 2004 Mw  
1088 6.0 Parkfield, California, earthquake. *Journal of Geophysical Research: Solid Earth*, 113(B2).

1089

1090 Martínez-Garzón, P., Ben-Zion, Y., Abolfathian, N., Kwiatek, G., & Bohnhoff, M. (2016). A  
1091 refined methodology for stress inversions of earthquake focal mechanisms. *Journal of  
1092 Geophysical Research: Solid Earth*, 121(12), 8666-8687.

1093

1094 McGarr, A. (2014). Maximum magnitude earthquakes induced by fluid injection. *Journal of  
1095 Geophysical Research: solid earth*, 119(2), 1008-1019.

1096

1097 Meier M.A. et al. "Activation of a natural granitic fault zone at the BedrettoLab" submitted  
1098 to Solid Earth (EGU).

1099

1100 Miller, S. A., Collettini, C., Chiaraluce, L., Cocco, M., Barchi, M., & Kaus, B. J. (2004).  
1101 Aftershocks driven by a high-pressure CO<sub>2</sub> source at depth. *Nature*.

1102

1103 Moein, M. J., Langenbruch, C., Schultz, R., Grigoli, F., Ellsworth, W. L., Wang, R., ... &  
1104 Shapiro, S. (2023). The physical mechanisms of induced earthquakes. *Nature Reviews Earth  
& Environment*, 4(12), 847-863.

1106

1107 Palgunadi, K. H., Gabriel, A. A., Ulrich, T., López-Comino, J. Á., & Mai, P. M. (2020).  
1108 Dynamic Fault Interaction during a Fluid-Injection-Induced Earthquake: The 2017 M<sub>w</sub> 5.5  
1109 Pohang Event. *Bulletin of the Seismological Society of America*, 110(5), 2328-2349.

1110

1111 Pelties, C., De la Puente, J., Ampuero, J. P., Brietzke, G. B., & Käser, M. (2012). Three-  
1112 dimensional dynamic rupture simulation with a high-order discontinuous Galerkin method on  
1113 unstructured tetrahedral meshes. *Journal of Geophysical Research: Solid Earth*, 117(B2).

1114

1115 Ramos, M. D., Thakur, P., Huang, Y., Harris, R. A., & Ryan, K. J. (2022). Working with  
1116 dynamic earthquake rupture models: A practical guide. *Seismological Society of America*,  
1117 93(4), 2096-2110.

1118

1119 Rice, J. R. (1992). Fault stress states, pore pressure distributions, and the weakness of the San  
1120 Andreas fault. In *International geophysics* (Vol. 51, pp. 475-503). Academic Press.

1121

1122 Rinaldi, A. P., & Rutqvist, J. (2019). Joint opening or hydroshearing? Analyzing a fracture  
1123 zone stimulation at Fenton Hill. *Geothermics*, 77, 83-98.

1124

1125 Rinaldi, A. P., Rutqvist, J., Luu, K., Blanco-Martín, L., Hu, M., Sentís, M. L., ... & Kaestli, P.  
1126 (2022). TOUGH3-FLAC3D: a modeling approach for parallel computing of fluid flow and  
1127 geomechanics. *Computational Geosciences*, 26(6), 1563-1580.

1128

1129 Rubin, A. M., & Ampuero, J. P. (2005). Earthquake nucleation on (aging) rate and state faults.  
1130 *Journal of Geophysical Research: Solid Earth*, 110(B11).

1131

1132 Schmedes, J., R. J. Archuleta, and D. Lavalle   (2010), Correlation of earthquake source  
1133 parameters inferred from dynamic rupture simulations, *J. Geophys. Res.*, 115, B03304,  
1134 doi:10.1029/2009JB006689

1135

1136 Scholz, C. H., & Cowie, P. A. (1990). Determination of total strain from faulting using slip  
1137 measurements. *Nature*, 346(6287), 837-839.

1138

1139 Scholz, C. H., & Lawler, T. M. (2004). Slip tapers at the tips of faults and earthquake  
1140 ruptures. *Geophysical research letters*, 31(21).

1141

1142 Shapiro, S. A., Kr  ger, O. S., Dinske, C., & Langenbruch, C. (2011). Magnitudes of induced  
1143 earthquakes and geometric scales of fluid-stimulated rock volumes. *Geophysics*, 76(6), WC55-  
1144 WC63.

1145

1146 Scuderi, M. M., & Collettini, C. (2016). The role of fluid pressure in induced vs. triggered  
1147 seismicity: Insights from rock deformation experiments on carbonates. *Scientific reports*, 6(1),  
1148 24852.

1149

1150 Tago, J., Cruz-Atienza, V. M., Virieux, J., Etienne, V., & Sánchez-Sesma, F. J. (2012). A 3D  
1151 hp-adaptive discontinuous Galerkin method for modeling earthquake dynamics. *Journal of*  
1152 *Geophysical Research: Solid Earth*, 117(B9).

1153

1154 Tinti, E., Bizzarri, A., Piatanesi, A., & Cocco, M. (2004). Estimates of slip weakening distance  
1155 for different dynamic rupture models. *Geophysical research letters*.

1156

1157 Tinti, E., Casarotti, E., Ulrich, T., Taufiqurrahman, T., Li, D., & Gabriel, A. A. (2021).  
1158 Constraining families of dynamic models using geological, geodetic and strong ground motion  
1159 data: The Mw 6.5, October 30th, 2016, Norcia earthquake, Italy. *Earth and Planetary Science*  
1160 *Letters*, 576, 117237.

1161

1162 Tobin, H. J., Saffer, D. M., Castillo, D. A., & Hirose, T. (2022). Direct constraints on in situ  
1163 stress state from deep drilling into the Nankai subduction zone, Japan. *Geology*, 50(11), 1229-  
1164 1233.

1165

1166 Uenishi, K., and J. R. Rice (2003), Universal nucleation length for slip-weakening rupture  
1167 instability under nonuniform fault loading, *J. Geophys.Res.*

1168

1169 Ulrich, T., Gabriel, A. A., Ampuero, J. P., & Xu, W. (2019). Dynamic viability of the 2016  
1170 Mw 7.8 Kaikōura earthquake cascade on weak crustal faults. *Nature communications*, 10(1),  
1171 1213.

1172

1173 Uphoff, C., May, D. A., & Gabriel, A. A. (2023). A discontinuous Galerkin method for  
1174 sequences of earthquakes and aseismic slip on multiple faults using unstructured curvilinear  
1175 grids. *Geophysical Journal International*, 233(1), 586-626.

1176

1177 Viesca, R. C., & Garagash, D. I. (2015). Ubiquitous weakening of faults due to thermal  
1178 pressurization. *Nature Geoscience*, 8(11), 875-879.

1179

1180 Volpe, G., Pozzi, G., Collettini, C., Spagnuolo, E., Achtziger-Zupančič, P., Zappone, A., ... &  
1181 Cocco, M. (2023). Laboratory simulation of fault reactivation by fluid injection and  
1182 implications for induced seismicity at the BedrettoLab, Swiss Alps. *Tectonophysics*, 862,  
1183 229987.

1184

1185 Wang, L., Kwiatek, G., Renard, F., Guérin-Marthe, S., Rybacki, E., Bohnhoff, M., ... & Dresen,  
1186 G. (2024). Fault roughness controls injection-induced seismicity. *Proceedings of the National  
1187 Academy of Sciences*, 121(3), e2310039121.

1188

1189 Wollherr, S., Gabriel, A. A., & Uphoff, C. (2018). Off-fault plasticity in three-dimensional  
1190 dynamic rupture simulations using a modal Discontinuous Galerkin method on unstructured  
1191 meshes: implementation, verification and application. *Geophysical Journal International*.

1192

1193 Yeck, W. L., Hayes, G. P., McNamara, D. E., Rubinstein, J. L., Barnhart, W. D., Earle, P. S.,  
1194 & Benz, H. M. (2017). Oklahoma experiences largest earthquake during ongoing regional  
1195 wastewater injection hazard mitigation efforts. *Geophysical Research Letters*.

1196

1197 Zoback, M., Hickman, S., Ellsworth, W., & SAFOD Science Team. (2011). Scientific drilling  
1198 into the San Andreas fault zone—an overview of SAFOD's first five years. *Scientific Drilling*,  
1199 11, 14-28.

# Modeling the 3D dynamic rupture of microearthquakes induced by fluid injection

**Mosconi F.<sup>1</sup>, Tinti E.<sup>1,2</sup>, Casarotti E.<sup>2</sup>, Gabriel A-A.<sup>3</sup>, Rinaldi A.P.<sup>4</sup>, Dal Zilio L.<sup>5</sup>, and Cocco M.<sup>2</sup>**

<sup>1</sup> La Sapienza Università di Roma, P.le Aldo Moro 5, 00185 Roma, Italia

<sup>2</sup> Istituto Nazionale di Geofisica e Vulcanologia, Rome, Italy

<sup>3</sup> Scripps Institution of Oceanography, UCSD, La Jolla, USA

<sup>4</sup> Swiss Seismological Service, Department of Earth Sciences, ETH Zürich, Switzerland

<sup>5</sup> Earth Observatory of Singapore, Nanyang Technological University, Singapore, Singapore,

Corresponding author: Francesco Mosconi (francesco.mosconi@uniroma1.it)

## Key Points:

- 3D dynamic rupture simulations of microearthquakes on a pressurized fault, with pore pressure profiles determined from poroelastic models.
- Modest variations of dynamic stress drop determine the rupture mode, distinguishing self-arresting from run-away ruptures.
- Runaway ruptures can dissipate more energy than self-arresting ones which display cracks transition into pulses upon arrest.

**Keywords:** induced earthquake, self-arresting rupture, runaway rupture, pore pressure changes, dynamic rupture propagation.

## Abstract

30 Understanding the dynamics of microearthquakes is a timely challenge with the potential to  
31 address current paradoxes in earthquake mechanics, and to better understand earthquake  
32 ruptures induced by fluid injection. We perform fully 3D dynamic rupture simulations caused  
33 by fluid injection on a target fault for FEAR experiments generating  $M_w \leq 1$  earthquakes. We

34 investigate the dynamics of rupture propagation with spatially variable stress drop caused by  
35 pore pressure changes and assuming different constitutive parameters. We show that the  
36 spontaneous arrest of propagating ruptures is possible by assuming a high fault strength  
37 parameter  $S$ , that is, a high ratio between strength excess and dynamic stress drop. In faults  
38 with high  $S$  values (low rupturing potential), even minor variations in  $D_c$  (from 0.45 to 0.6 mm)  
39 have a substantial effect on the rupture propagation and the ultimate earthquake size. Our  
40 results show that modest spatial variations of dynamic stress drop determine the rupture mode,  
41 distinguishing self-arresting from run-away ruptures. Our results suggest that several  
42 characteristics inferred for accelerating dynamic ruptures differ from those observed during  
43 rupture deceleration of a self-arresting earthquake. During deceleration, a decrease of peak slip  
44 velocity is associated with a nearly constant cohesive zone size. Moreover, the residual slip  
45 velocity value (asymptotic value for a crack-like rupture) decreases to nearly zero. This means  
46 that an initially crack-like rupture becomes a pulse-like rupture during spontaneous arrest. In  
47 summary, our findings highlight the complex dynamics of small earthquakes, which are  
48 partially contrasting with established crack-like models of earthquake rupture.

49

## 50 Plain language

51 Understanding small earthquakes, especially those induced by underground fluid injection, is  
52 crucial in earthquake science. In our study, we reproduce these events using computer  
53 simulations on a 50 meter wide fault, aiming to understand how fluid-induced stress changes  
54 affect the earthquake behavior. We find that earthquakes can stop under specific conditions,  
55 specifically when fault strength largely exceeds the difference between on-fault stress before  
56 and after the earthquake. Minor changes in rock properties, like static to dynamic friction  
57 transitions, significantly impact earthquake size. Our research also shows that stress variations  
58 on faults can determine if the earthquake is growing or arresting. We observe a significant  
59 spatial extension of the earthquake arrest phase, noting differences in features compared to  
60 earthquakes that exhibit accelerating rupture propagation. This distinct behavior is linked to  
61 the stress heterogeneity due to pore pressure gradient within the fault. Overall, our findings  
62 reveal the complex dynamics of small earthquakes, which is partially contrasting with the  
63 conventional crack theory.

## 64 1. Introduction

65 The study of earthquake mechanics and the analysis of source properties has been mainly  
66 focused on moderate to large seismic events (Kanamori, 2003; Schmedes et al., 2010; Harris,  
67 2017; Abercrombie, 2021). The investigation of the rupture process in micro-earthquakes, with  
68 magnitudes ranging between -4 and 2, has so far been carried out by spectral analysis of  
69 recorded data to derive source parameters such as seismic moment, source radius, stress drop  
70 and corner frequency (Imanishi and Ellsworth, 2006; Allmann et al., 2007, 2009; Selvadurai,  
71 2019; Abercrombie, 1995, 2021; Abercrombie and Rice, 2005; Cocco et al., 2016; 2023).  
72 These studies have been largely motivated by the need to constrain the scaling of earthquake  
73 source parameters – such as stress drop, radiated energy, source radius, and fracture energy –  
74 with seismic moment or total coseismic slip, laying the groundwork for our current  
75 understanding.

76 More recently, the emerging focus on induced seismicity and its related hazards has provided  
77 an opportunity to analyze faults more closely, improving our understanding of the dynamics  
78 that govern rupture initiation (Ellsworth, 2013; Grigoli et al., 2017; Moein et al., 2023; Galis  
79 et al., 2017). This was further promoted by the numerous laboratory experiments designed and  
80 performed to study the onset of dynamic instabilities in response to fluid injection on the rock  
81 sample, which provided relevant observations on induced laboratory earthquakes under  
82 controlled conditions (Scuderi and Collettini, 2016, Cappa et al., 2019; Hunfeld et al., 2021;  
83 Bolton et al., 2023; Volpe et al., 2023). While numerous studies on source complexity have  
84 concentrated on large earthquakes due to their associated severe damage and hazards, a  
85 persistent, unresolved, question in earthquake mechanics concerns the degree of heterogeneity  
86 and complexity influencing the rupture processes of microearthquakes. Furthermore, to the best  
87 of our knowledge, no studies have investigated the 3D rupture propagation and arrest of  
88 induced microearthquakes — an essential aspect in bridging the knowledge gap concerning  
89 induced seismicity and its relationship with microearthquakes.

90 Investigating the dynamics of microearthquakes necessitates the precise determination of  
91 constitutive parameters such as stress, friction, and critical slip at small spatial scales  
92 (millimeters to centimeters), which are crucial for understanding rupture propagation over  
93 meter-scale distances (1-100 m). Given the challenges in constraining source parameters using  
94 surface or near-surface data, innovative approaches have been proposed and adopted to collect  
95 near-source data and observations. These approaches include utilizing deep boreholes that  
96 intersect fault surfaces (Zoback et al., 2011; Tobin et al., 2022, among several others) as well

97 as underground laboratories providing access to fault zones at depths ranging between a few  
98 hundreds and a kilometer (Guglielmi et al. 2015; Lesko; 2015; among many others). Within  
99 this array of monitoring systems (deep borehole, underground labs and deep mines), the  
100 Bedretto Underground Laboratory for Geosciences and Geoenergies (BULGG) in the Swiss  
101 Alps provides access to a volume of crystalline faulted rocks at depth of 1000-1500 m (Ma et  
102 al., 2022; Achtziger et al., 2024). BULGG hosts the FEAR (Fault Activation and Earthquake  
103 Ruptures) ERC-Synergy project (Meier et al.; 2024) that aims at reactivating a natural fault  
104 under controlled conditions by stimulating the nucleation of a target earthquake of magnitude  
105  $M_w = 1$ . This event will be recorded with a dense multi-disciplinary on-fault monitoring system.  
106 Among several faults classified along the whole tunnel, the target fault for FEAR experiments,  
107 named hereinafter MC fault, has been identified (Achtziger et al., 2024; Volpe et al., 2023).  
108 The information required to constrain dynamic rupture simulations (e.g., Harris et al., 2018),  
109 including the fault geometry and stress state (slip tendency, stress orientation) as well as its  
110 frictional properties (Volpe et al., 2023) is available. Planned stimulation experiments within  
111 this fault zone, spanning 50-100 meters, will adhere to a precise injection protocol (Meier et  
112 al., 2024). The dedicated on-fault monitoring system is designed to capture microseismicity  
113 across a wide magnitude range ( $M_w$  -6 to 1), offering an unparalleled opportunity to examine  
114 the complex dynamics of rupture nucleation and propagation during microearthquakes within  
115 the magnitude range between 0 to 1.

116 The role of fluids in earthquake mechanics is well-documented in natural tectonic settings,  
117 anthropogenic activities, and laboratory experiments (Rice, 1992; Cocco and Rice, 2002;  
118 Miller et al., 2004; Ellsworth, 2013; Guglielmi et al., 2015; Viesca and Garagash, 2015;  
119 Martinez Garzon et al., 2016; De Barros et al., 2018; Cappa et al., 2019; Wang et al., 2024, and  
120 reference therein). Fault reactivation can result from an increase in the pore pressure  $P_f$   
121 (Hubbert and Rubey, 1959; Scholz, 1990), leading to a reduction in the effective normal stress  
122 ( $\sigma'_n = \sigma_n - P_f$ ) thereby influencing the frictional strength of the fault. In recent years, the  
123 growing energy demand, both fossil and renewable, has led to an increase in the activities  
124 related to the underground fluid injection. This requires to pose more attention on the hazard  
125 of the induced and triggered seismicity, in the context of oil and gas reservoir, underground  
126 carbon dioxide sequestration and geothermal energy (Ellsworth, 2013; Candela et al., 2018,  
127 Moein et al., 2023). Some examples of notable earthquakes associated to fluid injection are the  
128 2011  $M_w$  5.7 and 5.0 earthquakes near Prague in Oklahoma, United States (Keranen et al.,  
129 2013), the  $M_w$  5.8 Pawnee, Oklahoma, in 2016 (Yeck et al., 2017) and the 2017  $M_w$  5.5

130 earthquake near an enhanced geothermal site in Pohang, South Korea (Grigoli et al., 2018; Kim  
131 et al., 2018; Lee et al., 2019, Palgunadi et al., 2020).  
132 Numerous studies analyzed fault slip reactivation under elevated pore pressure, and both fluid-  
133 driven seismic and aseismic slip has been observed within a complex spectrum of fault-slip  
134 behavior (Garagash and Germanovich, 2012; Cappa et al., 2019; Larochelle et al., 2021; Dal  
135 Zilio et al., 2022; Ciardo and Rinaldi, 2022; Bolton et al., 2023). Experimental studies across  
136 various scales have highlighted the emergence of a zone characterized by aseismic slip, or  
137 creeping, adjacent to the injection point (Cornet, 2012, 2016; Garagash and Germanovich,  
138 2012; Guglielmi et al., 2015; Scuderi and Collettini, 2016). The nature of the stress state in the  
139 stimulated fault zone influences this aseismic slip, leading to strain-energy accumulation  
140 outside the slipping area. This process continues until a critical nucleation length is reached, at  
141 which point a dynamic instability can propagate (Uenishi and Rice, 2003; Cebry et al., 2022).  
142 Upon nucleation, the rupture propagates dynamically, characterized by high slip velocities and  
143 rupture speeds, generating seismic waves. The arrest of the rupture occurs when the rupture  
144 front does not possess enough energy to continue propagating. While the mechanisms of  
145 natural earthquake arrest are still debated (Kame and Yamashita, 1999; Galis et al., 2019; Ke  
146 et al., 2022; among several others), dynamic rupture models typically assume locally low-stress  
147 or high frictional strength, for example by prescribing spatial heterogeneities of the shear stress  
148 or static friction coefficient (Das & Aki, 1977; Harris et al., 2018; Ramos et al., 2021).  
149 The study of rupture propagation and arrest in induced earthquakes allows the differentiation  
150 between self-arrested and runaway ruptures. The former refers to ruptures that spontaneously  
151 stop at a finite distance from the nucleation zone often remaining within the pressurized patch,  
152 while the latter describes ruptures that extend across the entire fault, ceasing only at fault  
153 boundaries due to geometrical complexities, stress or strength heterogeneities (Galis et al.,  
154 2017; Ke et al., 2018, 2022). This classification elucidates the rupture dynamics without  
155 necessarily invoking heterogeneous stress patches. Galis et al., (2017) pointed out that, while  
156 injection-induced earthquakes may cause severe seismic hazard, they also represent an  
157 opportunity to gain insights in earthquake physics. They used a linear slip weakening law to  
158 model an induced rupture and Linear Elastic Fracture Mechanics (LEFM) to interpret the  
159 transition between self-arresting and runaway induced earthquakes. They found that this  
160 transition is mainly controlled by frictional parameters and stress heterogeneity. Additionally,  
161 these authors corroborate the dependence of the expected magnitude of the induced earthquake  
162 on the radius of the pressurized area and on the injected fluid volume (Mc Garr, 2014; Galis et

163 al., 2017; De Barros et al., 2019; Moein et al., 2023). However, a fundamental physical  
164 explanation of why dynamic rupture arrests or can continue propagating is still elusive.

165 In this study, we concentrate on the spontaneous dynamic simulation of rupture processes for  
166 induced earthquakes with a maximum magnitude of less than 1 ( $M_w < 1$ ). Our simulations  
167 encompass the full dynamics of earthquake rupture and seismic wave propagation within a 3D  
168 volume, based on a linear slip-weakening model to describe shear stress evolution at the rupture  
169 front and initiated by pore fluid pressurization. We apply our model to the target fault within  
170 the Bedretto Underground Laboratory for Geosciences and Geo-energies (BULGG) at an  
171 approximate depth of 1500 meters.

172 The aim of this study is to simulate the propagation and the arrest of dynamic ruptures on the  
173 pressurized fault selected for FEAR experiments. The fault is characterized by initially uniform  
174 frictional parameters and is subjected to uniform prestress. This simplified initial stress  
175 condition is adopted to emphasize the role of pore pressure changes on spontaneous dynamic  
176 rupture propagation. A realistic pore pressure profile caused by fluid injection in a nucleation  
177 patch is simulated considering the poroelastic response of the fault zone. The rupture process  
178 during induced microearthquakes is investigated to shed light on the key features of dynamic  
179 propagation as well as the constitutive parameters influencing the extent of the rupture before  
180 its arrest, determining the magnitude of the induced earthquake.

181

## 182 2. Methods and Source Parameterization

183 We utilize the open-source software SeisSol ([www.seissol.org](http://www.seissol.org)) to model the 3D spontaneous  
184 rupture propagation of micro-earthquakes on a 3D fault plane. SeisSol is based on the arbitrary  
185 high-order derivative discontinuous Galerkin (ADER-DG) method (Dumbser and Käser,  
186 2006), and solves the 3D elastodynamic equation for spontaneous frictional failure on a  
187 prescribed fault surface, whereas for the seismic wave propagation it computes the elastic wave  
188 equation in heterogeneous media (Pelties et al., 2012). The applicability of SeisSol has been  
189 verified in various earthquake scenarios, ranging from models including a simple planar fault  
190 to more complex fault geometries involving geometric discontinuities, non-planarity, fault  
191 roughness, and multiple intersecting adjacent fault branches (Harris et al., 2018; Ulrich et al.,  
192 2019; Tinti et al., 2021; Taufiqurrahman et al., 2022; Biemiller et al., 2023, Gabriel et al.,  
193 2023). This study presents the first dynamic rupture simulation for an induced micro-

194 earthquake on a decametric-scale planar fault (50 m length), under stress conditions determined  
195 by fluid injection and pore-pressure changes.

196

197 **2.1. Linear slip-weakening friction law**

198 Dynamic earthquake modeling requires the use of a fault constitutive law which describes shear  
199 traction evolution in each point on the fault characterizing the breakdown stage and dynamic  
200 weakening near the rupture front. Different constitutive laws analytically describe the shear  
201 stress as a function of diverse constitutive variables, such as slip, slip velocity, state, and  
202 temperature. Here, we adopt the linear slip-weakening (LSW) constitutive law (Ida, 1972)  
203 because it is simple and allows the clear definition of fracture energy and a direct control on  
204 different key parameters such as fault strength and dynamic stress drop during the rupture  
205 propagation.

206 This constitutive relation is characterized by the peak stress value on the fault  $\tau_p = \mu_s \sigma'_n$ , the  
207 dynamic residual (i.e., frictional) stress level  $\tau_d = \mu_d \sigma'_n$ , and the critical slip distance  $D_c$ , as

208

$$209 \tau = \begin{cases} \left[ \mu_s - (\mu_s - \mu_d) \frac{\delta}{D_c} \right] \sigma'_n, & \delta < D_c \\ \mu_d \sigma'_n, & \delta > D_c \end{cases} \quad (1)$$

210

211 where  $\mu_s$  and  $\mu_d$  are the static and dynamic friction coefficients, respectively,  $\sigma'_n$  is the effective  
212 normal stress and  $\delta$  the slip. When the shear stress reaches its peak value the fault starts  
213 slipping and the shear stress decreases linearly from the peak to the residual stress value over  
214 a critical slip distance  $D_c$ . This breakdown stress drop ( $\Delta\tau_p = \tau_p - \tau_d$ ) corresponds to a friction  
215 decrease from the static to the dynamic friction coefficient. Once the slip exceeds the critical  
216 slip distance ( $D_c$ ), the shear traction becomes independent of slip and equal to the residual  
217 dynamic stress level  $\tau_d = \mu_d \sigma'_n$ . The final stress is equal to the residual stress level, and stress  
218 overshoot or undershoot are not considered. The energy dissipated to sustain the rupture  
219 propagation, namely the fracture energy, depends on the values of the breakdown stress drop  
220 and the critical slip weakening distance  $D_c$ .

221 According to equation (1), the strength excess ( $\tau_p - \tau_0$ ) is defined as the difference in shear  
222 stress between its peak and initial values, with the peak stress being equal to the yield strength  
223 of the fault. The strength excess occurs with no slip and is associated with a linear elastic and  
224 reversible process. The dynamic stress drop ( $\Delta\tau_d = \tau_0 - \tau_d$ ), is the stress released during the

225 dynamic weakening. Because the final stress is equal to the residual dynamic stress level ( $\tau_d$ ),  
226 the dynamic and static stress drop are the same. The ratio between the stress excess and the  
227 dynamic stress drop is the strength parameter  $S$ , as defined by the pioneering paper of Andrews  
228 (1976):

$$229 \quad S = \frac{(\tau_p - \tau_0)}{(\tau_0 - \tau_r)} \quad (2)$$

230  
231 Previous studies dealing with modeling earthquake ruptures have emphasized the importance  
232 of computing the non-dimensional strength parameter  $S$  that allows us to describe the potential  
233 of the fault to develop a rupture (Andrews, 1976; Das & Aki, 1977; Geubelle & Kubair, 2001;  
234 Liu & Lapusta, 2008; Barras et al., 2023). Andrews (1976) found that the parameter  $S$  controls  
235 the transition of a crack from sub-shear rupture to supershear rupture propagation. More recent  
236 studies have also demonstrated its significance in influencing rupture style (Gabriel et al., 2012;  
237 Bai and Ampuero, 2017) or its role in the context of induced seismicity (Galis et al., 2017).  
238 The parameter  $S$  measures the material strength (strength excess) relative to the stress release  
239 during dynamic rupture (dynamic stress drop). The strength excess quantifies the necessary  
240 stress to be concentrated at the rupture front, from the initial to the peak shear stress, needed  
241 for the propagation. On the other hand, the dynamic stress drop encompasses the stress released  
242 during the dynamic breakdown referred to the initial shear stress, characterizing the tectonic  
243 loading of the fault before the initiation of a dynamic rupture.  
244 The LSW constitutive law allows the interpretation of key features of the dynamic rupture  
245 propagation in terms of a few parameters, even in a very sensitive condition such as an induced  
246 earthquake. The advantage of working in a well constrained in-situ boundary condition, as  
247 provided by the Bedretto Lab, helps to decrease the a-priori assumptions and to investigate the  
248 dynamics of microearthquakes focusing on the less poorly constrained constitutive parameters  
249 (such as the critical slip distance  $D_c$ ).

## 250        2.2. Fault model and input parameters

251 We simulate a dynamic rupture scenario, for an induced earthquake, on a  $60^\circ$  dipping normal  
252 fault, embedded in a 3D elastic medium, with a P-wave speed of 2621 m/s, S-wave speed of  
253 1531 m/s and a density of 2620 kg/m<sup>3</sup>. To accurately define the fault geometry, we leverage  
254 in-situ geological and geophysical characterizations of the target fault, conducted as part of the  
255 FEAR project in the Bedretto Tunnel. These characterizations, detailed in Achtziger et al.  
256 (2024), reveal that the target fault exhibits an approximately planar geometry, extending

257 laterally for about 250 meters. In our model we consider a volume of 200 x 200 x 200 m and  
258 a fault dimension of 50 x 50 m, representing the fluid pressurized portion of the larger MC fault  
259 zone (Figure 1a). The computational domain is discretized using an unstructured mesh, with a  
260 total number of ~69 million tetrahedral elements. The elements in the volume change in size,  
261 transitioning from 12 cm length close to the fault to a maximum value of 15 m at the volume  
262 edge, in order to maintain both computational efficiency and high resolution, simultaneously.  
263 The well-constrained in-situ boundary conditions of the Bedretto Tunnel allow us to include a  
264 realistic on-fault stress state with negligible spatial variations due to the small fault dimension  
265 here considered. Therefore, we impose a constant normal and shear stress on the fault prior to  
266 fluid injection, with the former prescribed at  $\sigma_n = 22.7$  MPa and the latter to  $\tau_0 = 4.7$  MPa.  
267 The static ( $\mu_s$ ) and dynamic ( $\mu_d$ ) friction coefficients are considered homogeneous and constant  
268 over the fault. The static friction is  $\mu_s = 0.58$ , while the dynamic friction is assumed to be  $\mu_d =$   
269 0.21 for the first set of Models A and  $\mu_d = 0.15$  for the second set of Models B that will be  
270 discussed in the paper. The initial resulting stress conditions after the stress perturbation due  
271 the injection of fluid within each specific set of models will be described more in detail in the  
272 subsequent Section 3.

273 A crucial parameter in dynamic rupture simulations is the on-fault resolution to capture the  
274 stress dissipation in the cohesive zone, i.e. the spatial dimension along fault where the shear  
275 stress weakening occurs, evolving from the peak value to the residual level. Based on the  
276 extended analysis conducted by Wollherr et al. (2018) to achieve a well resolved cohesive zone  
277 we adopt a spatial discretization with an on fault mesh element size of 12 cm with a mean  
278 cohesive zone dimension of 0.34m (detailes in Supplementary material)

279

### 280 3. Stress changes from fluid injection

281 The main goal of this work is to investigate the characteristics of a dynamic rupture resulting  
282 from on-fault fluid pressurization, exploring various scenarios to understand the conditions  
283 leading to a self-arresting rupture with  $M_w < 1$ , as opposed to a runaway earthquake that  
284 ruptures the entire fault surface, resulting in a  $M_w > 1$ .

#### 285 3.1. Pore pressure changes profile

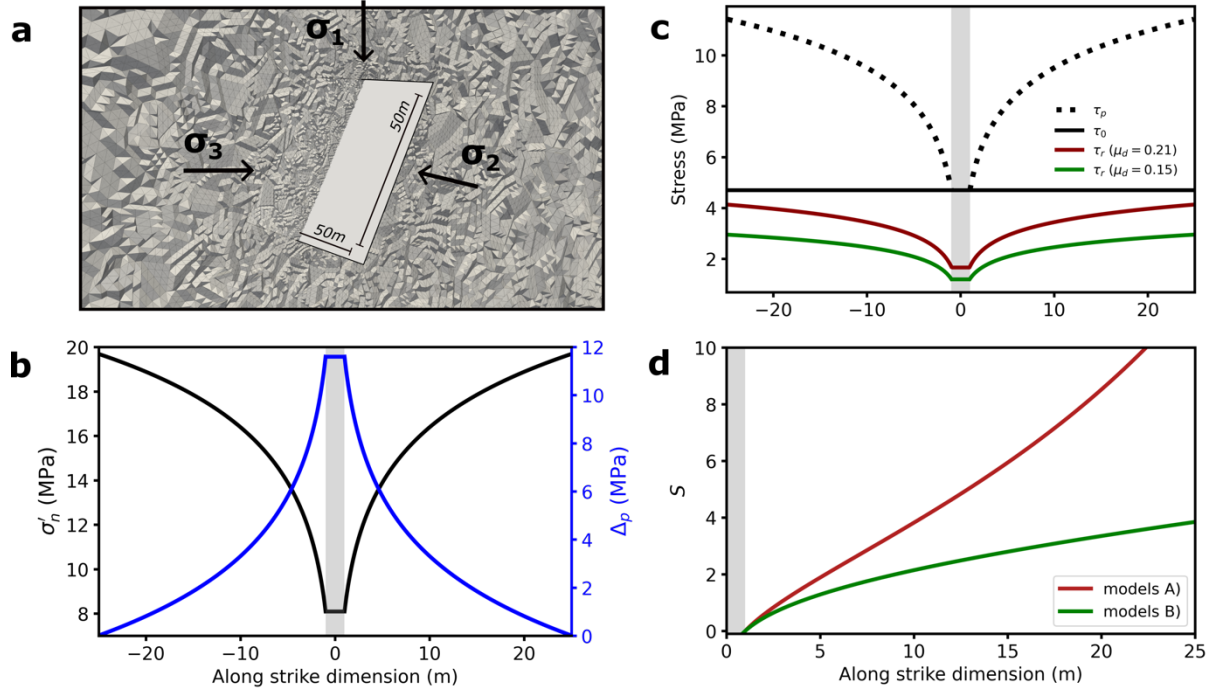
286 In order to create realistic pressure conditions on the fault zone, we employ the software  
287 TOUGH3-FLAC3D, that allows the simulation of coupled fluid flow and geomechanics

288 (Rinaldi et al., 2022). This approach aims at simulating complex non-linear behavior  
289 potentially occurring in the vicinity of the injection point, as well effects of a packed interval.  
290 The coupled approach allows us to account for full poroelasticity via porosity evolution as well  
291 as variation of permeability as function of geomechanical parameters (e.g. stress or strain). We  
292 develop a first-order model (50 m X 50 m X 50 m) with a fault zone dipping 60°, 20 cm thick,  
293 and cutting through an homogenous medium.

294 Initial conditions follow the state of stress found at the BedrettoLab (Bröker & Ma, 2022,  
295 Bröker et al., 2023), with minimum horizontal stress at 20 MPa, maximum horizontal stress at  
296 25 MPa, and vertical stress at 31 MPa for the injection region. The initial pore pressure at the  
297 injection is set at 3.8 MPa. We impose constant stress and pressure at all boundaries. In terms  
298 of rock properties, the fault zone is assumed weaker than the surrounding formation, with a  
299 Young's modulus of 5 GPa compared to 15 GPa of the host rock. The Poisson's ratio is set to  
300 0.25 in the entire domain. We neglect poroelastic effects by assuming a near-zero Biot's  
301 coefficient (0.001).

302 The permeability of the fault zone is assumed constant at  $10^{-15}$  m<sup>2</sup>, representing a fractured  
303 region within homogeneous granite with permeability set at  $10^{-18}$  m<sup>2</sup>. The injection region at  
304 the center of the model is set as a 1 m<sup>2</sup> patch, with permeability changing as a function of the  
305 normal effective stress (Rinaldi & Rutqvist, 2019). Porosity is set to 1% in the entire domain.  
306 We simulate 24 hours of injection at constant flow rate (0.012 kg/s), simulating a constant  
307 pressure of about 14.5 MPa at the injection point, and allowing fluids to propagate along the  
308 fault. The given pressure is the one observed to be the jacking pressure in several injections at  
309 the BedrettoLab (Bröker et al., 2023). In TOUGH-FLAC, the given conditions would reactivate  
310 the fault within the next numerical time step with a further increase in pressure when assuming  
311 a fault zone with a friction angle of 31°, yielding a static friction coefficient of 0.6 very similar  
312 to the value adopted for dynamic simulations (0.58). Hence, we stop our simulation at the time  
313 step before earthquake nucleation on the fault would occur. The simulated pressure profile  
314 (Figure 1b) is then used as the starting point for the dynamic rupture model and it is considered  
315 representative of key physical conditions during direct injection into a fault zone.

316



317

318 **Figure 1.** 3D dynamic rupture model setup. **(a)** Adopted fault geometry and grid size (50 x  
319 50m), volumetric computational mesh (200 x 200 x 200m) and principal stress orientations. **(b)**  
320 Profile of pore-pressure change of the 25m radius pressurized fault patch (blue line) and on-  
321 plane effective normal stress (black line). The gray bar shows the position of the injection  
322 borehole. **(c)** Spatial profile of the resulting stress parameters after the fluid pressurization.  
323 The peak stress (or static fault strength, black dashed line) and the initial shear stress (black  
324 solid line) are the same for both the class of Models A and B, which differ for the residual  
325 stress level because of the different adopted dynamic friction coefficients (red solid line 0.21  
326 and green solid line 0.15). **(d)** Evolution of the strength parameter S (Eq. 2) for half-fault  
327 dimension for the set of Models A and B (red line and green line, respectively).

328 **3.2. Modeled stress conditions**

329 Figure 1-b shows the pore pressure and normal stress profiles resulting from fluid injection into  
330 the modeled fault patch: the effective normal stress is minimal in the injection zone (gray  
331 shaded bar) and increases along the strike direction as pore pressure decreases.

332 Figure 1c illustrates the spatial distribution of the on-fault stress parameters. The peak stress or  
333 the fault static strength ( $\tau_p = \mu_s \sigma'_n$ ) is shown by a black dashed line and it increases from the  
334 fault center (injection point) towards the fault boundary due to the increase of  $\sigma'_n$  (Figure 1b).  
335 The initial stress (solid black line) is constant over the whole pressurized fault patch. At the  
336 center of the fault, the peak stress is equal to the initial shear stress meaning that the strength  
337 parameter is zero and the rupture can nucleate. The fault portion affected by the nucleation is  
338 represented with the gray bar. The residual shear stress also increases within the fault radius  
339 because of the effective normal stress gradient. It is important to note that all the discussed

340 stress conditions are valid across the different fault directions, implying a radial  
341 parametrization.

342 As anticipated above, we simulate here two sets of models distinguished for the value of the  
343 assumed dynamic friction coefficient: Models A (solid red) dynamic friction is  $\mu_d = 0.21$ , while  
344 in Models B  $\mu_d = 0.15$ . Although peak stress remains similar between Models A and B,  
345 variations in dynamic friction lead to differences in breakdown and dynamic stress drop values,  
346 as well as spatial stress gradients along the fault. The spatial gradient of the effective normal  
347 stress ( $\sigma'_n$ ) also determines the spatial variability of the parameter S (Figure 1d), which is due  
348 to the spatial increment of the strength excess coupled with the reduction in the dynamic stress  
349 drop along the fault radius. This implies a quite different spatial gradient of the strength  
350 parameter S for the two sets of Models (A and B), as shown in Figure 1d for half fault  
351 dimension.

352 As we will discuss in the following, each set of models yields different behaviors of dynamic  
353 rupture propagation for different ranges of the critical slip weakening distance: namely, Models  
354 A yield self-arresting ruptures and Models B runaway ruptures. This confirms that the S  
355 parameter plays a crucial role in the behavior of dynamic rupture propagation for induced  
356 earthquakes. It is worth observing that in our simulation, we intentionally did not include any  
357 additional heterogeneity of the initial stress or other constitutive parameters, because we are  
358 going to focus on the role of pore pressure and effective normal stress ( $\sigma'_n$ ) changes caused by  
359 the fluid injection. In the following we will examine the influence of the S parameter on the  
360 behavior of dynamic rupture propagation and arrest in the context of induced seismicity.

361

### 362 3.3. Rupture nucleation

363 The earthquake nucleation zone is located at the fault injection point by assuming that the fault  
364 strength (initial stress value) equals the peak shear stress, the latter being determined by the  
365 pore-pressure peak caused by fluid injection (see Figure 1). In models of single dynamic  
366 rupture events, we generally adopt the assumption of artificial rupture initiation to enable more  
367 computationally efficient simulations. (Dalguer & Day, 2009; Bizzarri, 2010; Galis et al.,  
368 2015). Indeed, accounting for spontaneous nucleation due to an increasing tectonic loading in  
369 time (Uenishi and Rice, 2003, Rubin and Ampuero, 2005) requires different model  
370 parametrization, a friction law that accounts for the fault strength recovery (i.e., Rate & State  
371 friction law) and different numerical algorithms, e.g., an adaptive time stepping scheme during  
372 the simulation of the full seismic cycle (Lapusta and Liu, 2009) solvers suited for elliptic

373 instead of hyperbolic partial differential equations (Uphoff et al., 2023), which are adopted for  
374 simulations of sequences of earthquakes and aseismic slip (e.g., Barbot et al. 2012; Jiang et al.,  
375 2022 ).

376 In general, a dynamic rupture necessitates to first reach a critical length before spontaneously  
377 growing, leading to an unstable propagation. A relation to estimate the universal critical  
378 nucleation length for homogenous condition of the in-plane crack under slip weakening friction  
379 law has been provided by Uenishi & Rice (2003):

380

381

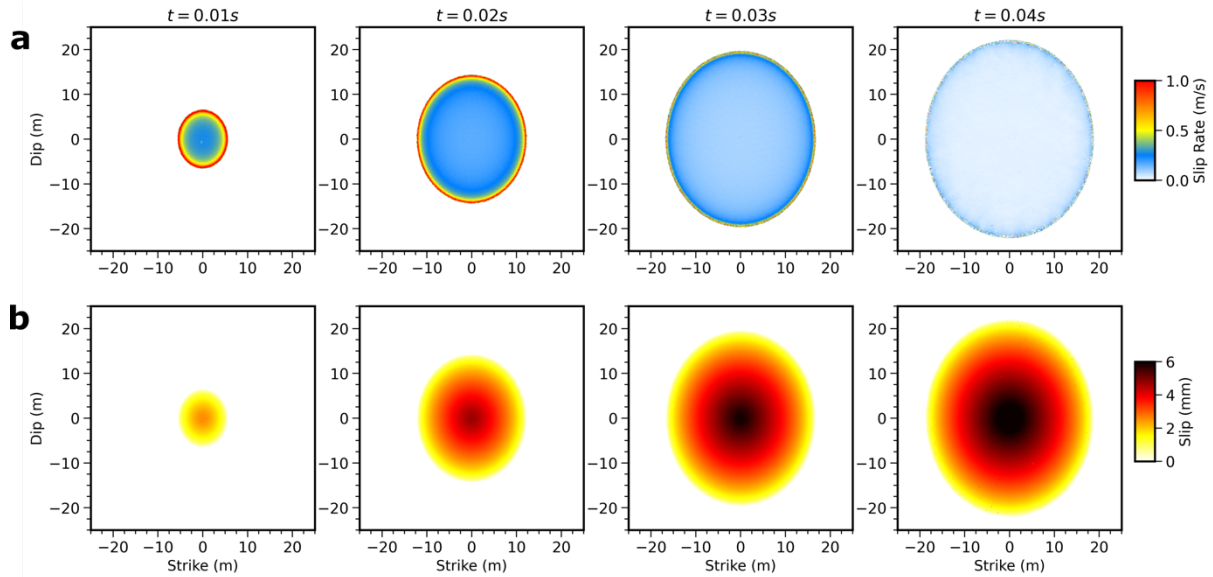
$$l_c = 1.158 \frac{1}{(1-\nu)} \frac{G D_c}{\Delta\tau_b} \quad (3)$$

382 where,  $G$  is the shear modulus,  $\nu$  the Poisson's ratio,  $D_c$  the critical slip weakening distance  
383 and  $\Delta\tau_b$  is the breakdown stress drop.

384 There are two nucleation approaches mainly adopted in the literature for dynamic rupture  
385 simulations: initiation through a time-weakening law where the rupture front velocity is  
386 imposed (Andrews, 1985) or the overstressed patch leading to instantaneous nucleation patch  
387 failure (Kanamori, 1981). This study adopts a slightly modified rupture initiation method,  
388 tailored to the unique stress conditions induced by fluid stimulation and the subsequent  
389 reduction in effective normal stress. We assume a constant time-independent pore pressure  
390 value within the injection zone corresponding to a borehole radius of 1 m and representing the  
391 maximum pressure change (Figure 1b, Section 3.1). This fluid pressure plateau represents the  
392 initial region where the fault strength equals the initial shear stress level, and consequently the  
393 rupture is able to nucleate. To achieve a gradual and smooth increase in fault slip rate at the  
394 hypocenter from  $\sim 10^{-2}$  m/s to typical seismic slip velocity values for dynamic rupture  
395 simulations ( $\sim 10^0$  m/s), we impose a slightly smaller  $D_c = 0.4$  mm within the nucleation patch  
396 for all models. A quantitative formulation which would allow us to estimate the critical size of  
397 the nucleation patch in 3D and under non-homogeneous normal stress conditions is elusive.  
398 We therefore use equation (3) to develop an estimate of the size of the nucleation patch.  
399 Equation 3 predicts a critical nucleation half-length varying between 0.7 and 1.2m due the  
400 variation in breakdown stress drop and the different adopted  $D_c$  values. In agreement with this  
401 estimate, in our simulations the nucleation patch size is adopted from the poro-elastic  
402 simulations protocol of fluid injection (1 m bore hole size), with a nucleation behavior  
403 consistent across all models. The adopted stress and constitutive conditions allow us to  
404 maintain the same nucleation patch size in all our simulations because the fault strength

405 reduction along the source radius is determined by the imposed pore-pressure profile resulting  
 406 from poro-elastic modeling.

407

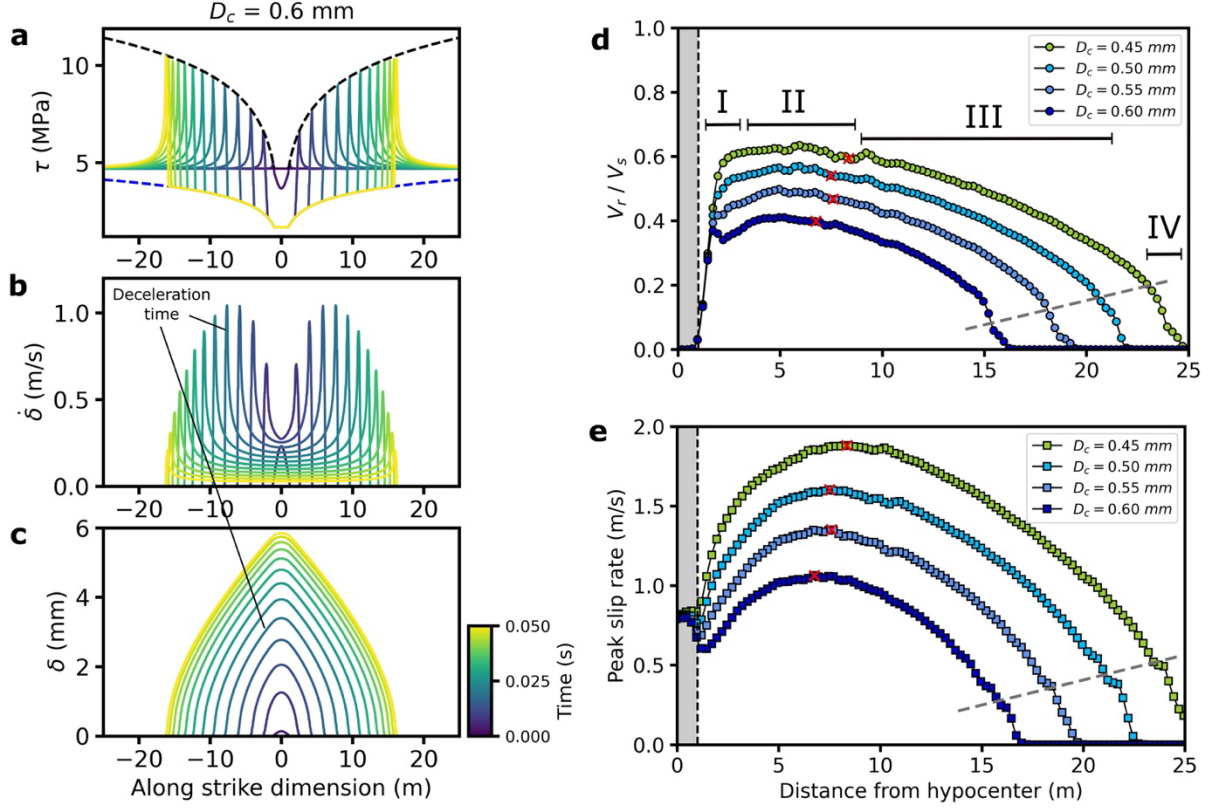


408  
 409

410 **Figure 2.** Evolution of the dynamic rupture for the model with  $D_c = 0.6$  mm belonging to the  
 411 class of Models A. **(a)** Snapshots of the slip rate during the rupture propagation. **(b)** Snapshots  
 412 of the accrued cumulative slip. Color scales display values of slip rate and slip.

## 413 4. Results

414 We present a series of 3D simulations of the spontaneous propagation of dynamic rupture along  
 415 a pressurized fault with a spatial pore pressure profile constrained by poroelastic simulations  
 416 aimed at reproducing a stimulation experiment envisioned in the FEAR project. As described  
 417 above, the fault geometry and parameterization are taken from the target fault zone of the FEAR  
 418 project in the Bedretto underground laboratory (BULGG). We investigate two classes of  
 419 Models characterized by different values of the dynamic friction coefficient: Models A have  
 420 dynamic friction  $\mu_d$  equal to 0.21, while in Models B  $\mu_d$  is 0.15. For each class of Models we  
 421 use different ranges of the critical slip weakening distance. In the following we present the  
 422 results of our simulations for each class of Models.



423

424

425 **Figure 3.** Illustration of the set Models A with imposed  $\mu_d = 0.21$  for an along-strike section.  
426 (a-c) Example of rupture evolution through different snapshots of shear stress ( $\tau$ ), slip velocity  
427 ( $\dot{\delta}$ ) and slip profile ( $\delta$ ), the colormap indicates the temporal evolution of the rupture. (d)  
428 Rupture speed and peak slip rate (e) as a function of the hypocentral distance (injection point).  
429 The four stages shown in panel d have been drawn for the model with  $D_c = 0.45$  mm. Red stars  
430 mark the end of phase II, corresponding to the respective maximum in peak slip rate for each  
431 model. Color scale displays temporal evolution in panels a-b-c and adopted  $D_c$  values in panels  
432 d, e.

433

434

#### 4.1. Self-arresting earthquakes

435 We first analyze the set of Models A ( $\mu_d = 0.21$ ) and explore a range of  $D_c$  values ranging from  
436 0.45 mm to 0.6 mm. The dynamic models computed with these parameters are characterized  
437 by self-arresting ruptures, which results in induced earthquakes with  $M_w < 1$ . Figure 2 shows  
438 the evolution of a propagating rupture for a model with  $D_c = 0.6$  mm: Panel (a) displays the  
439 snapshots of slip velocity at different times, while Panel (b) shows the snapshots of cumulative  
440 slip. The slip distribution shown in Panel b resembles those observed in natural earthquakes  
441 and laboratory experiments. (Scholz & Lawer, 2004; Ke et al., 2018). Given the source  
442 parameterization, the rupture propagates with nearly radial symmetry. This symmetry provides

443 a basis for detailed examination of shear stress, slip velocity, and slip evolution along specific  
444 orientations, including the along-strike direction – a focal point of our subsequent analysis.  
445 Figure 3 shows the shear stress, slip velocity and slip evolution with respect to the fault strike  
446 direction during dynamic rupture propagation computed for  $D_c = 0.6$  mm (panels a, b and c,  
447 respectively), which displays the key features of self-arresting ruptures over a source radius of  
448 nearly 15 m. The evolution of shear stress, slip velocity and slip in the along-dip direction is  
449 detailed in the Supplementary Material (Figure S1a, b, c). Comparing Figures 3a-c and S1a-c  
450 confirms that, despite minor differences in rupture velocities, the along-dip results are similar  
451 to those retrieved analyzing propagation along-strike direction. The initial increase of peak slip  
452 velocity is followed by a gradual decrease during the arrest stage resulting in the retrieved  
453 spatial slip gradient. This slip rate behavior implies a crack-like rupture (Kostrov, 1964),  
454 meaning that all points behind the rupture front continue to slip until the rupture arrest. Peak  
455 and residual stress values change with position along the strike because of the variable effective  
456 normal stress (Figure 1).

457 The breakdown stress drop increases during rupture propagation, because the increase of peak  
458 shear stress along the fault radius is larger than the increase of residual stress. Panels d and e  
459 of Figure 3 summarize the behavior of dynamic ruptures for the four simulations conducted  
460 with  $D_c$  ranging from 0.45 mm to 0.6 mm showing the rupture velocity and peak slip rate,  
461 respectively, with respect to half-strike dimension. The vertical gray-shaded bar indicates the  
462 size of the nucleation patch adopted in all simulations, while the red stars identify the points  
463 along the fault where each rupture model reaches its maximum peak slip velocity, (Figure 3 e).  
464 The behavior of rupture velocity and peak slip rate allows us to subdivide the rupture  
465 propagation in four distinct stages (Figure 3d). The first stage (I) corresponds to the initial rapid  
466 acceleration of the rupture front outside the nucleation patch associated with rapidly increasing  
467 peak slip rate. This stage is followed by a propagation at nearly constant rupture velocity  
468 characterized by smoothly increasing peak slip rate reaching its maximum value during  
469 propagation (stage II). At this point, the dynamic rupture starts to decelerate. We have  
470 distinguished two stages during rupture deceleration: stage III is characterized by a continuous  
471 decrease of rupture velocity with a progressive decrease of peak slip rate, followed by stage IV  
472 in which rupture velocity and peak slip velocity abruptly drop to zero. The inferred four stages  
473 describe acceleration, propagation, deceleration, and arrest of dynamic rupture propagation, as  
474 clearly pointed out by the spatial evolution of rupture speed and slip rate.

475 Rupture velocity reaches its maximum value during the initial rupture acceleration (I) in a  
476 relatively small spatial extension; this maximum rupture speed is maintained during the

477 subsequent stage (II) preceding rupture deceleration (in stage III). The spatial extension of  
478 dynamic rupture during these first two stages slightly depends on the adopted  $D_c$  values, while  
479 on the contrary the rupture velocity values depend on the assumed values of the critical slip  
480 weakening distance  $D_c$ : the smaller  $D_c$ , the higher the rupture velocity values characterizing  
481 each simulation. During the acceleration stages (I and II), peak slip velocity continuously  
482 increases up to its maximum value marking the beginning of rupture deceleration. Inferred  
483 peak slip velocity values are inversely proportional to the critical slip weakening distance  $D_c$   
484 (Figure 3 e).

485 Differently from the initial stages (I and II) characterized by rupture acceleration or propagation  
486 at nearly constant speed, the spatial extension of the deceleration stage (III) depends on  $D_c$ : the  
487 larger  $D_c$ , the smaller is the rupture area characterized by rupture deceleration. This implies  
488 that  $D_c$  together with the dynamic friction value control the dimensions of the final ruptured  
489 area and therefore the magnitude of the induced earthquake for self-arresting ruptures. It is  
490 interesting to observe that the rate at which the rupture decelerates appears to be similar among  
491 all models. Finally, all simulations display the arrest phase IV characterized by an abrupt  
492 decrease in both rupture speed and peak slip rate, as indicated by the gray dashed line in Fig.  
493 3d-e. We note that all ruptures stop within the pressurized fault patch, with source radii ranging  
494 from approximately  $\sim 15$  to  $\sim 24$  m. The released moment magnitudes ( $M_w$ ) are 0.76, 0.88, 0.97  
495 and 1, respectively, increasing with decreasing  $D_c$ .

496 A self-arresting rupture generates a nearly triangular shape of the slip spatial profile (Figure 3  
497 c), with a maximum slip of 5.8mm for the adopted  $D_c$  value (0.6 mm). During the initial rupture  
498 acceleration stages (I and II) slip reaches a peak value of  $\sim 3$ mm (at the injection point), as  
499 indicated by lines in Panel b-c highlighting the timestep when deceleration starts (the rupture  
500 front at this point is 6-7 m away from nucleation). This implies that only half of peak slip and  
501 less than half of the rupture extension has been reached during the acceleration of the rupture  
502 (phase I and II), determining a large portion of the seismic moment release during the  
503 deceleration stage (phase III and IV) (see Supplementary Material, Figure S3).

504

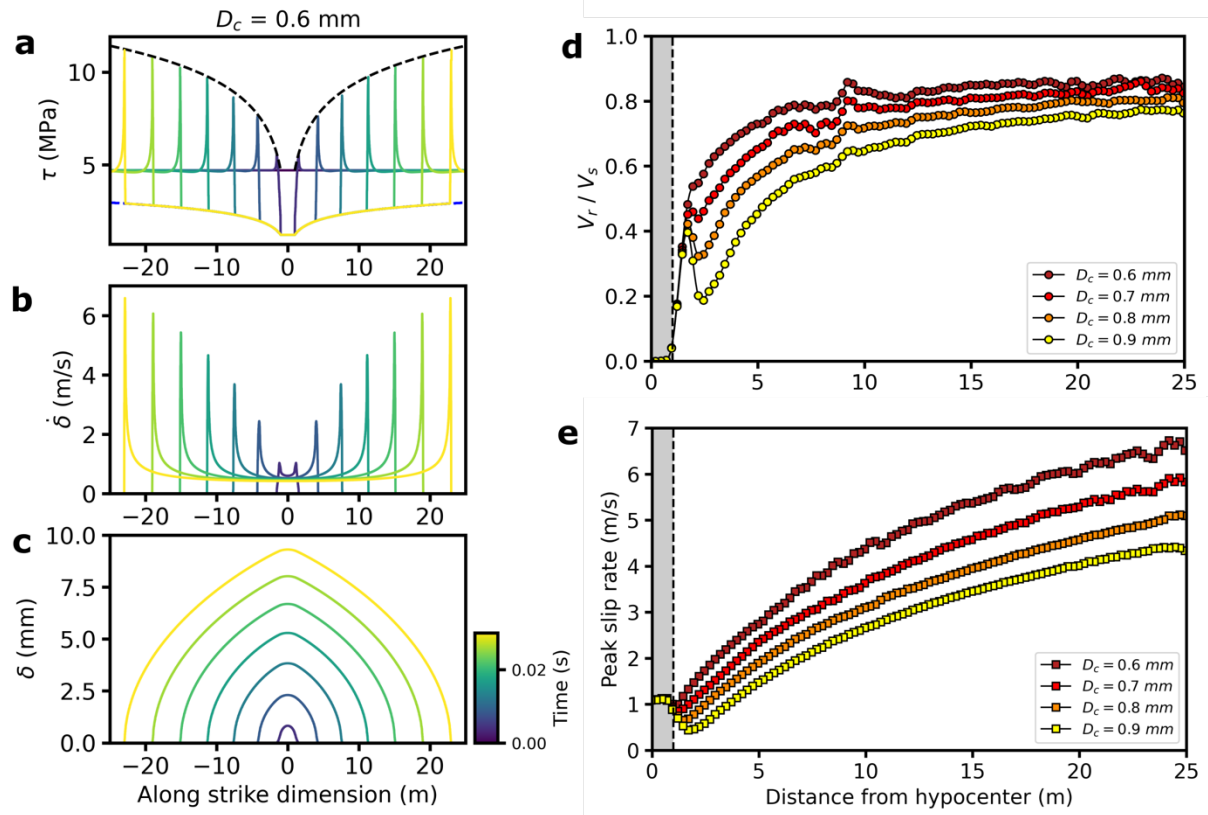
## 505 4.2. Runaway earthquakes

506 It is often assumed (Shapiro et al., 2011; McGarr, 2014) that a rupture remains confined within  
507 the volume affected by the pore pressure change, that is within the pressurized fault patch.  
508 However, if the dynamic load at the crack-tip is sufficiently large to sustain rupture  
509 propagation, the rupture can extend beyond the pressurized patch. This extension enables the

510 rupture to encompass a larger fault area, consequently leading to an earthquake of greater  
511 magnitude. This is the case of the runaway ruptures investigated in this study. As anticipated  
512 above, the class of Models B relies on the assumption of a lower dynamic friction coefficient  
513 (namely,  $\mu_d = 0.15$ ) over the target fault, leading to runaway ruptures propagating outside the  
514 pressurized fault. For this class of Models B, we explored a range of  $D_c$  values ranging from  
515 0.60 mm to 0.90 mm.

516 Figure 4 shows the shear stress, slip velocity and slip evolution along the strike direction  
517 (Panels a, b, c, respectively) for a simulation performed with  $D_c=0.6$  mm, the same  $D_c$  value  
518 used in Figure 3 for self-arresting ruptures (the respective along-dip evolution is shown in  
519 Figure S2). The shear traction evolution displayed in Figure 4a shows the differing increase of  
520 peak and residual stress values with space, resulting in the increase of breakdown stress drop  
521 during the rupture propagation. The spatial increase of the strength parameter S (Figure 1d) is  
522 modest because the increase of strength excess (the same as model A) is counterbalanced by  
523 the larger dynamic stress drop (see equation 2). The peak slip rate continuously increases  
524 during propagation, maintaining a constant residual slip velocity value behind the rupture front  
525 coherently with crack-like ruptures. The maximum peak slip velocity is 6 m/s for this  
526 simulation with  $D_c=0.6$  mm. The slip profiles (elliptical) shown in Panel e are also coherent  
527 with an accelerating crack-like rupture (Gabriel et al., 2012).

528 Figure 4-d and 4-e illustrates how rupture speed and peak slip velocity vary with respect to half  
529 fault strike dimension across different values of the critical slip weakening distance ( $D_c$ ). After  
530 the initial rapid acceleration, the rupture front decelerates with smoothly increasing rupture  
531 velocity remaining within the sub-shear regime. Decreasing the adopted  $D_c$  value results in a  
532 faster acceleration and higher rupture velocities. This is why we explore slightly larger  $D_c$   
533 values in Models B compared to those adopted in Models A, which would otherwise yield  
534 supershear rupture. Peak slip velocity continuously increases during propagation for all the  
535 adopted  $D_c$  values, with the largest peak slip rate values for the smallest  $D_c$ . The rupture  
536 propagates along the whole pressurized patch with an increasing peak slip velocity and without  
537 any deceleration. This characterizes the runaway ruptures. Our simulations suggest that,  
538 regardless of the adopted  $D_c$  value, obtaining a self-arresting rupture is not possible if the  
539 dynamic friction is imposed to 0.15, even when the chosen  $D_c$  value is approximately twice  
540 than that used in the class of Models A. For the set of parameters adopted in Models B, when  
541 rupture nucleates, it always propagates as a runaway rupture front. Rupture arrest for runaway  
542 ruptures occurs only if the rupture encounters a geometrical barrier or an area with unfavorable  
543 stress conditions outside the pressurized patch.



546 **Figure 4.** Illustration of the set Models B with imposed  $\mu_d = 0.15$  for along-strike section. (a-  
547 c) Example of rupture evolution through different snapshots of shear stress ( $\tau$ ), slip velocity  
548 ( $\dot{\delta}$ ) and slip profile ( $\delta$ ). (d) Rupture speed and peak slip rate (e) as a function of the hypocentral  
549 distance (injection point). Color scale displays temporal evolution in panels a-b-c and  $D_c$  values  
550 in panels d, e.

## 552 5. Discussion

553 In this study we have simulated self-arresting and runaway ruptures by stimulating a  
554 pressurized patch through fluid injection within the nucleating zone. Fluid injection maintains  
555 a constant peak of pore-pressure within the nucleation patch (1 m radius), where peak shear  
556 stress  $\tau_p$  is imposed to be equal to the initial stress value. Fluid injection generates a spatial  
557 pore-pressure gradient decreasing towards the edges of the pressurized patch. Since the initial  
558 stress is deliberately maintained as homogeneous across the fault, the resulting spatial gradient  
559 of effective normal stress (Figure 1) causes spatially variable strength excess, breakdown and  
560 dynamic stress drops. Therefore, it is crucial to discuss the factors determining whether a  
561 rupture is self-arresting or runaway, characteristics that directly impact the moment magnitude  
562 of the induced earthquake and the associated seismic hazard.

563        5.1 Fracture energy

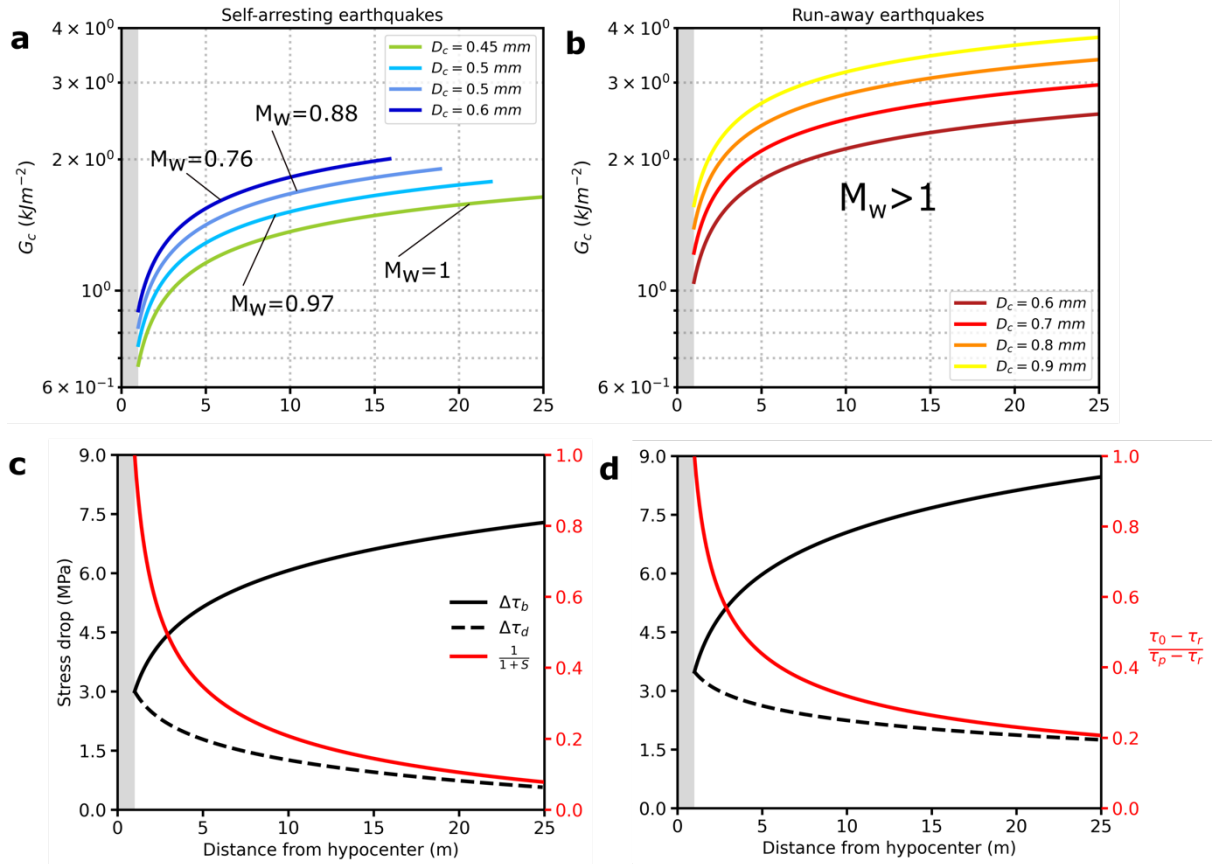
564        Models A and B differ in their dynamic friction coefficients and the range of employed critical  
565        slip weakening distances ( $D_c$ ). It is important to point out that for Models B, which are  
566        characterized by a lower dynamic friction coefficient, all simulated dynamic ruptures are  
567        runaway ruptures for any adopted value of  $D_c$ . On the contrary, for simulations belonging to  
568        Models A, the self-arresting feature disappears if we decrease  $D_c$  below 0.2 mm. To understand  
569        this different behavior, we analyze for each model the fracture energy  $G_c$ , a crucial parameter  
570        to understand earthquake propagation and arrest (Andrews, 1976; Cocco et al., 2023; Gabriel  
571        et al. 2024, Arxiv).

572        For a linear slip-weakening constitutive law,  $G_c$  depends linearly on breakdown stress drop and  
573         $D_c$  (Ida, 1972). Figure 5 shows the spatial evolution of fracture energy for self-arresting (panel  
574        a) and runaway (panel b) ruptures. Runaway ruptures dissipate more energy density (or  
575        breakdown work, Tinti et al., 2005) than self-arresting ruptures. Comparing the simulations  
576        performed with the same  $D_c$  value (0.6 mm) for the two classes of models, the self-arresting  
577        rupture (Models A) dissipates less fracture energy at the rupture front than the runaway rupture  
578        (Models B). This is because breakdown stress drop is larger for runaway ruptures belonging to  
579        the class of Models B (Figure 1b). Therefore, we conclude that self-arresting ruptures are not  
580        caused by a larger energy dissipation at the rupture front (i.e., fracture energy). Panels c) and  
581        d) of Figure 5 show that the decrease in dynamic stress drop for self-arresting ruptures (Models  
582        A) is larger than the one inferred for runaway ruptures (Models B). Furthermore, the increase  
583        in breakdown stress drop is smaller for self-arresting ruptures, and this results in a smaller ratio  
584        between dynamic and breakdown stress drop (i.e.  $1/(1+S)$  in Figure 5 c - d), which is associated  
585        with larger spatial values of the  $S$  parameter (Figure 1). It is important to emphasize that in all  
586        these dynamic models, rupture propagation is associated with spatially variable stress drops  
587        (dynamic and breakdown).

588        Decreasing  $D_c$  for Models A yields runaway ruptures because fracture energy  $G_c$  decreases,  
589        yielding  $G_c$  values much smaller than those inferred for larger  $D_c$  values ( $> 0.4$ ) or for Models  
590        B (see Supplementary Material Figure S4). This implies that within a given class of Models  
591        (i.e., for a given value of dynamic friction coefficient) the dissipated energy determines the  
592        self-arresting or runaway features of the dynamic rupture propagation of the induced  
593        earthquake. However, larger energy dissipation at the rupture front (i.e., fracture energy) is not  
594        sufficient to explain the occurrence of self-arresting ruptures as shown by the comparison  
595        between Panels b and a in Figure 5. More generally, self-arresting rupture depends on the

596 assumed residual stress level, and fracture energy alone does not fully characterize the required  
 597 conditions for self-arresting dynamic ruptures since the strength excess parameter  $S$  is also  
 598 important and it should be considered as well (see Panels 5c and 5d).

599



600  
 601

602 **Figure 5.** Fracture Energy (i.e., energy dissipation) and stress drop comparison for the two  
 603 sets of Models A and B. **(a-b)** Spatial variation of fracture energy with the distance from the  
 604 hypocenter (injection point) for the set of Models A and B, respectively. The curves for self-  
 605 arresting models (Models A) are interrupted to indicate the arrest points of the ruptures. **(c-d)**  
 606 Spatial variation of stress drops with distance from the hypocenter (injection point) for sets of  
 607 Models A and B, respectively. The black dashed line represents the dynamic stress drop, the  
 608 black solid line depicts the breakdown stress drop, and the red solid line illustrates the ratio  
 609 between these two stress drops, labeled by the  $1/(1+S)$  parameter to link the curve to the  
 610 strength parameter  $S$ .

611

## 5.2 Dynamic load

612 The behavior of peak slip velocity during dynamic propagation (Figures 3 and 4) suggests that  
 613 the differences between self-arresting and runaway ruptures can be interpreted in terms of the  
 614 dynamic load sustaining rupture front propagation. Despite the large dissipation at the rupture  
 615 front (i.e., fracture energy), the dynamic load is much larger for runaway ruptures than for self-

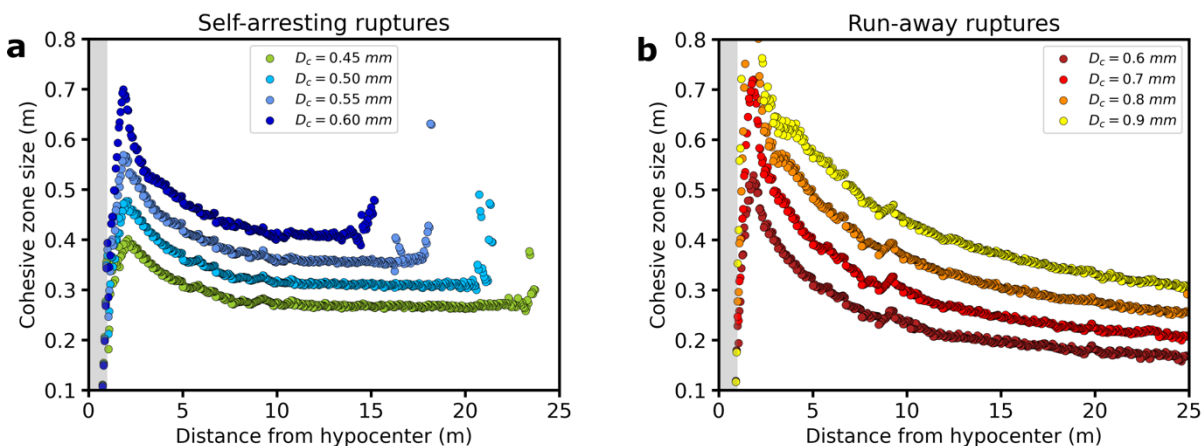
616 arresting ones. A straightforward method to represent the dynamic load at the rupture front is  
 617 computing the shear stress at a given point on the fault, which is a function of slip velocity.  
 618 Fukuyama and Madariaga (1998) proposed the following relationship:

619

$$\sigma(x, t) = -\frac{G}{2\beta} \dot{\delta}(x, t) + \int_{\Sigma} \int_0^t K(x - \xi; t - t') \dot{\delta}(\xi, t') dt' ds \quad (4)$$

620 where  $\beta$  is the shear wave velocity,  $\dot{\delta}(x, t)$  is the slip velocity function and  $K$  is the kernel  
 621 representing the dynamic interaction among those points that are slipping behind the rupture  
 622 front. The integral is computed over the portion of the fault  $\Sigma$  that slipped at time  $t$  in which  
 623 the rupture front has reached the point  $x$  on the fault. Equation (4) highlights that the  
 624 contribution to shear stress at a given point is composed of two terms: an instantaneous  
 625 contribution determined by the slip velocity evolution at that point in space and time (i.e., a  
 626 radiation damping term), and the integral term which represents the dynamic interactions of  
 627 the points on the fault behind the rupture front that are still slipping with decreasing values of  
 628 slip velocity. We can therefore infer that higher slip velocity values are associated with larger  
 629 dynamic load at the rupture tip. This discussion relates to the size of the cohesive zone, which  
 630 is the portion of the fault composed of the points located behind the rupture tip that are  
 631 undergoing dynamic weakening and are expected to have the largest values of slip velocity  
 632 around the peak slip rate. Therefore, they provide the largest contributions to the dynamic  
 633 interactions (the integral term in equation 4) and to the dynamic load at the rupture front.

634



635

636

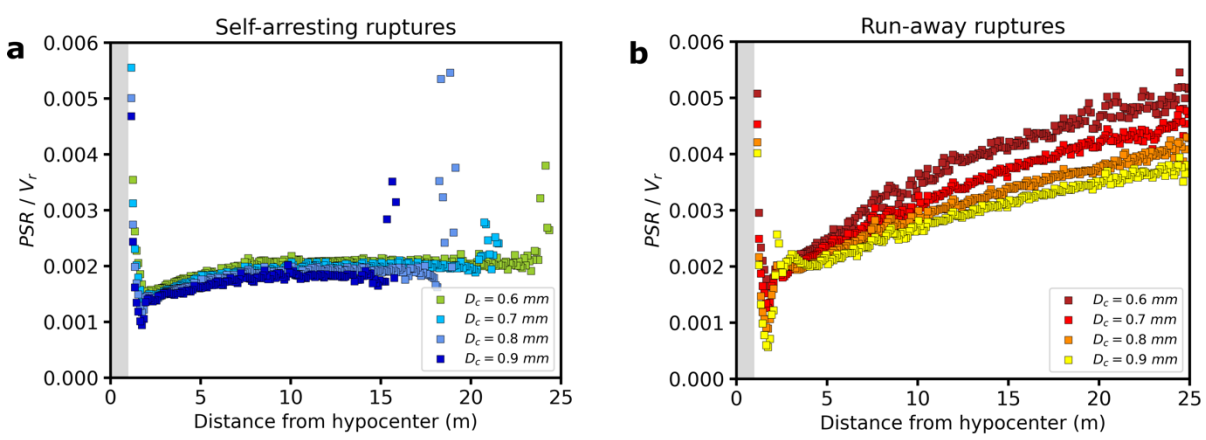
637 **Figure 6.** Cohesive zone behavior for set Models A and B. **(a-b)** The two panels respectively  
 638 show the cohesive zone size with respect to the hypocentral distance (injection point), of the  
 639 self-arresting (set Models A) and runaway ruptures (set Models B).

640

641 Figure 6 shows the cohesive zone sizes for self-arresting (Panel a) and runaway (Panel b)  
 642 ruptures measured for the different ranges of  $D_c$ . The size of the cohesive zone is measured

643 from the breakdown time (i.e., the time window representing the duration of dynamic  
 644 weakening) of each single fault point multiplied by its local rupture speed (Day et al., 2005;  
 645 Wollherr et al., 2018). Across the first 5-7.5 meters of rupture propagation away from the  
 646 nucleation patch the cohesive zone shrinks for both self-arresting and runaway ruptures. This  
 647 is associated with an increase of peak slip velocity and with rupture acceleration following the  
 648 nucleation (Figures 3 and 4). However, for self-arresting ruptures the cohesive zone size  
 649 becomes nearly constant (Figure 6a) as soon as the rupture stops accelerating (stage II in Figure  
 650 3), unlike for runaway ruptures where the cohesive zone size continuously decreases (Figure  
 651 6b and Figure S5). This key observation is associated with the decrease of peak slip velocity  
 652 and rupture velocity (stages III and IV of Figure 3a and b). This corroborates that the size of  
 653 the cohesive zone is linked to both slip velocity and rupture speed evolution during dynamic  
 654 rupture propagation (Day et al., 2005).

655 We next discuss the distinctive features of self-arresting and runaway ruptures by analyzing  
 656 the ratio between peak slip velocity and rupture speed. Figure 7 shows this ratio as a function  
 657 of the distance from the nucleation patch. After an initial stage in which rupture speed increases  
 658 more than peak slip velocity for both model classes (A and B), self-arresting ruptures are  
 659 characterized by a nearly constant ratio between peak slip velocity and rupture speed,  
 660 suggesting that they both decrease during the deceleration phase at the same rate in space. In  
 661 contrast, in runaway ruptures peak slip velocity increases more than rupture speed because the  
 662 shrinking of the cohesive zone decreases due to the reduced rupture acceleration (Figure 6b).  
 663



664  
 665  
 666 **Figure 7.** Peak slip rate variation normalized by the rupture speed for the set of Models A and  
 667 B. **(a-b)** Showing respectively the spatial variation of the ratio between the peak slip rate of the  
 668 rupture and the rupture speed with the hypocentral distance (injection point), for self-arresting  
 669 (set Models A) and runaway ruptures (set Models B).  
 670

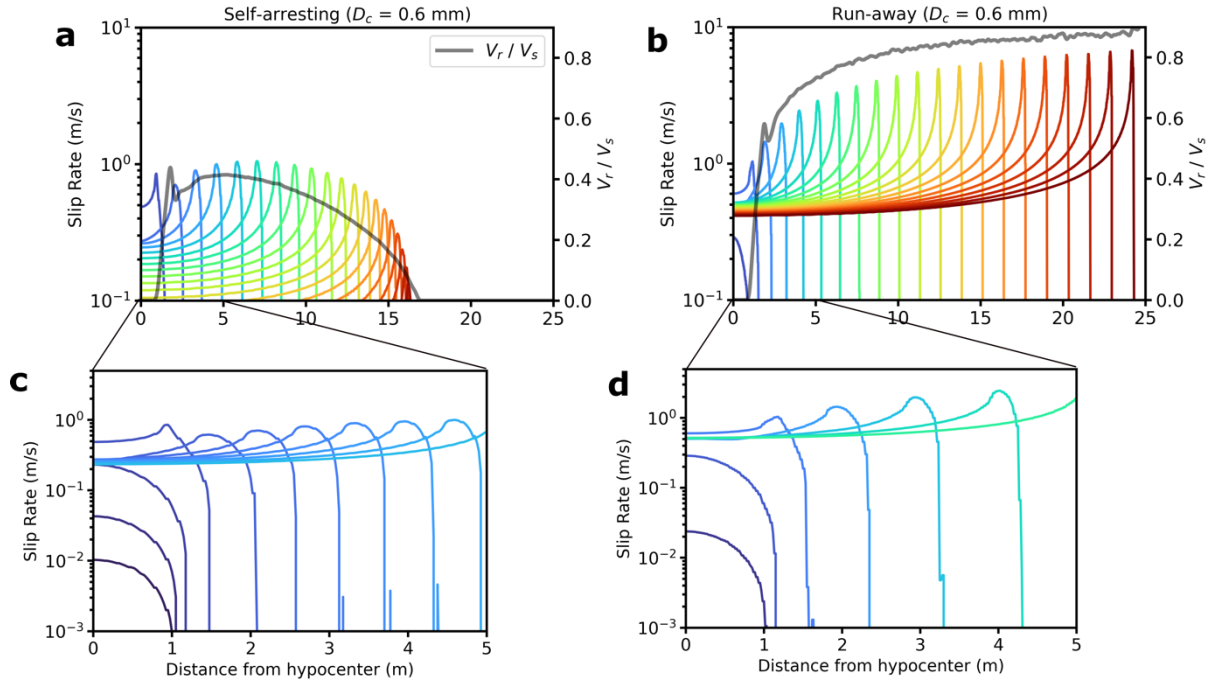
671

672        5.3 The dynamics of decelerating ruptures

673 The spatial gradient of strength excess, breakdown and dynamic stress drop caused by fluid  
674 injection in a pressurized patch determines interesting features for a self-arresting rupture  
675 characterized by a decelerating rupture front propagation over an extended portion of the fault.  
676 Figure 3 shows that the decelerating rupture front propagates over nearly 60% of the radius of  
677 the pressurized patch. The first key feature is the coupling between peak slip velocity and  
678 rupture velocity. This is further investigated in Figure 8 (Panels a and c) showing the slip  
679 velocity time histories and the evolution of rupture velocity in different fault positions along  
680 the strike direction for the simulations with  $D_c = 0.6$  mm. Runaway ruptures are characterized  
681 by an increasing peak slip velocity and rupture speed, with a constant asymptotic residual value  
682 of slip rate, as expected for crack-like models (0.4-0.5 m/s). On the contrary, self-arresting  
683 ruptures show an initial rupture acceleration with increasing peak slip velocities, followed by  
684 a deceleration with decreasing peak slip velocity. Unlike runaway ruptures, self-arresting  
685 ruptures display a decreasing asymptotic residual value of slip rate during the deceleration  
686 stages. This does not occur during the initial acceleration stage of self-arresting rupture. Figure  
687 8 b and d show a zoom of the slip velocity evolution during the first 5 meters from nucleation.  
688 During the initial acceleration stage slip velocity increases for both self-arresting and runaway  
689 ruptures, but the former have smaller values than the latter. Slip velocities for self-arresting  
690 ruptures remain smaller than 1 m/s, differing from runaway ruptures that exceed 1 m/s after a  
691 few meters from nucleation.

692 This analysis yields two main implications. First, it further corroborates that tiny differences in  
693 the residual stress due to the adopted dynamic friction coefficients and the spatial gradient of  
694 normal stress result in spatially variable dynamic stress drop and strength parameter  $S$ ,  
695 determining the self-arresting features. Second, for self-arresting ruptures during the  
696 deceleration stage, the asymptotic residual slip velocity value decreases during dynamic  
697 propagation approaching zero. This implies that during rupture deceleration and arrest, a crack-  
698 like model becomes a pulse like rupture, without exhibiting any stress undershoot (Lambert et  
699 al. 2021), encountering any fault width barrier (Weng & Ampuero, 2019), or facing bi-material  
700 contrast (Ampuero & Ben-Zion, 2008).

701



702  
703  
704  
705  
706  
707  
708  
709  
710  
711

**Figure 8.** Evolution of slip rate and rupture speed for two example ruptures with the same  $D_c$  (0.6mm) in the sets of Models A and B. Panels (a-c) display the slip rate evolution at different timesteps, indicated by the colormap, and the evolution of the rupture speed depicted by the gray solid line, for self-arresting (set Models A) and run-away (set Models B) ruptures, respectively. (b-d) Zooming in on the initial 5 meters of the rupture extension to emphasize the evolution of the slip rate during nucleation and the initial acceleration outside the nucleation patch.

712  
713  
714  
715  
716  
717  
718  
719  
720

#### 5.4 Implications for earthquake mechanics

721 Although the stress conditions modeled in this work are carefully selected, we believe that they  
722 are representative of fluid pressurization on a relatively homogeneous fault. While initial stress  
723 heterogeneity is a common condition to model dynamic ruptures on active faults (Ripperger et  
724 al., 2007; Ma et al. 200; Tago et al. 2012; Tinti et al., 2021; among many others), we believe  
725 that simulating dynamic propagation for a stress configuration characterized by a relatively  
726 smooth spatial gradient is of interest for studying induced seismicity. The results obtained in  
727 this work highlight distinct dynamic aspects of a decelerating rupture front that deserve to be  
728 further investigated under a wider range of initial conditions.

729 Notably, in our simulations the residual stress level (i.e., dynamic stress) is not constant in  
730 space and exhibits spatial gradients due to the effective normal stress changes induced by pore  
731 pressure perturbations. This is different from the conditions commonly adopted in linear elastic  
732 fracture mechanics (Galis et al., 2017; Brener and Bouchbinder, 2021; Kammer et al., 2024).

725 In particular, while runaway ruptures characterized by a dynamic propagation at increasing or  
726 nearly constant rupture velocity (i.e., without deceleration) are coherent with crack-like  
727 models, in which slip velocity evolves from its peak to an invariant residual value, self-arresting  
728 ruptures characterized by the propagation of a decelerating rupture front over an extended fault  
729 dimension exhibit unconventional features not completely coherent with pure crack-like  
730 models (as evidenced by the decreasing residual slip velocity values behind the decelerating  
731 rupture front). This feature represents a deviation from predictions from linear elastic fracture  
732 mechanics, and it is not usually observed in dynamic simulations with linear slip weakening  
733 law and heterogeneous prestress. It is worth noting that in our dynamic simulations we do not  
734 prescribe the Griffith energy balance at the crack tip (Freund, 1989; Galis et al., 2017; Kammer  
735 et al., 2024), for which the energy release rate (energy flow at the crack-tip) is equal to the  
736 fracture energy (i.e., the energy dissipated at the rupture front). In other words, we do not  
737 assume that the energy flow is equal to the dissipated energy at the rupture tip. Indeed, the  
738 solution of the 3D dynamic rupture propagation is obtained by assuming the constitutive law  
739 (the linear slip weakening in our case) and the collinearity between slip velocity and shear  
740 traction. This explains why self-arresting ruptures are not uniquely characterized by larger  
741 energy dissipation at the rupture tip; rather, the larger spatial decrease of dynamic stress drop  
742 (as mapped by spatial gradient of the strength parameter S) determines self-arresting features.

## 743 6. Conclusions

744 In this paper we have performed a series of 3D simulations to model the dynamic rupture of a  
745 pressurized patch stimulated through fluid injection within the nucleation zone. To our  
746 knowledge, these represent the first dynamic rupture simulations for an induced micro-  
747 earthquake on a decametric-scale planar fault (50 m length). Previously, only Liu and Lapusta  
748 (2008) modeled a ~2 magnitude micro-earthquake repeater of the San Andreas Fault through  
749 3D seismic cycle simulation. The fault geometry and the pore fluid pressure changes have been  
750 modeled to reproduce the stimulation experiments envisioned by the FEAR project in the  
751 Bedretto Lab (BULGG). In particular, the pore pressure profile along the fault radius and  
752 around the injection borehole has been computed through poro-elastic simulation of the fault  
753 zone. The initial stress is kept constant to investigate the role of the spatial gradient of effective  
754 normal stress. The two classes of models simulated in this study differ in their values of the  
755 dynamic friction coefficient and in the range of their values of the critical slip weakening  
756 distance. Models B have a smaller dynamic friction coefficient ( $\mu_d = 0.15$ ) and larger  $D_c$  values

757 ranging from 0.60 mm to 0.90 mm. They result in runaway ruptures propagating over the entire  
758 pressurized patch, without any deceleration of the rupture front. This behavior is obtained also  
759 using smaller values of the critical slip weakening distance  $D_c$ , which have not been discussed  
760 because they yield supershear ruptures. On the contrary, Models A, characterized by a higher  
761 dynamic friction coefficient ( $\mu_d = 0.21$ ) and smaller  $D_c$  values ranging from 0.45 mm to 0.60  
762 mm, display self-arresting rupture within the pressurized patch. Decreasing  $D_c$  for this class of  
763 Models A would yield runaway ruptures.

764 The results of this study are of relevance to discuss the dynamic propagation of rupture during  
765 an induced earthquake characterized by a spatially variable, continuously increasing effective  
766 normal stress governed by the pore fluid pressurization of the fault patch. This causes spatially  
767 variable peak and residual stress values, which result in a spatially variable strength excess,  
768 breakdown and dynamic stress drops. In this configuration, decreasing the residual stress by  
769 changing the dynamic coefficient of friction makes the fault more unstable, yielding runaway  
770 ruptures for a broad range of  $D_c$  values. This results in generating smooth, spatially variable  
771 frictional strength, as described by the spatial evolution of the S parameter. While this is  
772 expected, a tiny increase of the dynamic friction coefficient, which is still representative of a  
773 weak fault ( $\mu_d \approx 0.2$ ), can generate self-arresting ruptures characterized by a large spatial  
774 increase (gradient) of the S parameter caused by the spatial decrease in dynamic stress drop. In  
775 this configuration, we have found a range of  $D_c$  values for which self-arresting ruptures are  
776 characterized by the propagation of a decelerating rupture front over a finite portion of the  
777 pressurized patch. Self-arresting ruptures do not reach the edge of the pressurized patch, unlike  
778 runaway ruptures.

779 Our simulations corroborate that self-arresting and runaway ruptures are determined by the  
780 stress state within the pressurized patch. However, the analysis of the dynamics of a  
781 decelerating propagating rupture yields interesting and somehow surprising results.

782 We have shown that the distinction between self-arresting and runaway ruptures cannot be  
783 explained solely in terms of fracture energy (i.e., the energy dissipated at the rupture front);  
784 that is, ruptures are not self-arresting because they dissipate more energy at the tip. Runaway  
785 ruptures dissipate more energy than self-arresting ones, even if decreasing fracture energy (by  
786 decreasing  $D_c$ ) transforms self-arresting ruptures into runaway ones. The spatial variation of  
787 frictional strength caused by the spatially increasing normal stress within the pressurized patch  
788 is the key feature to enable self-arresting, because it is determining the dynamic load sustaining  
789 the propagation of the rupture front. Indeed, the behavior of slip velocity, rupture speed and

790 cohesive zone size suggests that dynamic load, supporting rupture front propagation, is larger  
791 for runaway ruptures. On the contrary, we can conclude that for self-arresting ruptures the  
792 dynamic load is not large enough to maintain the dynamic rupture propagation causing rupture  
793 deceleration associated with a nearly constant size of the cohesive zone and decreasing peak  
794 slip velocity values until the final rupture arrest. The peculiar feature of this dynamic  
795 propagation is the spatially variable dynamic stress drop and strength excess.

796 The dynamic propagation of an induced self-arresting rupture over a finite extension of the  
797 pressurized patch generates a slip velocity field that differs from that obtained for runaway  
798 ruptures, characterized by the propagation at constant or increasing rupture speed. The most  
799 evident feature is the decrease of peak slip velocity associated with the decelerating rupture  
800 and the nearly constant cohesive zone size. The other relevant feature is the decrease of the  
801 residual slip velocity value (asymptotic value for a crack-like rupture), which decreases during  
802 deceleration becoming nearly zero. This means that the initial crack-like rupture retrieved  
803 during the acceleration stage becomes a pulse-like rupture at the arrest.

804 The results of this study, obtained under specific stress conditions, are applied to a realistic  
805 scenario of an induced earthquake at BULGG. Nonetheless, they allow us to highlight how the  
806 study of the rupture dynamics of an induced earthquake involves peculiarities relevant to the  
807 mechanics of earthquakes. The spatially variable normal stress causes variations of frictional  
808 strength and spatially variable breakdown and dynamic stress drops. This might have  
809 implications for radiated energy and frequency contents of ground motions caused by induced  
810 earthquakes. Although further investigations are needed to account for prestress heterogeneity,  
811 we emphasize the importance of exploring rupture deceleration over a finite portion of a  
812 pressurized patch.

813  
814

## 815 **Acknowledgements**

816 This study has received funding from the European Research Council (ERC) under the  
817 European Union's Horizon 2020 research and innovation programme (grant agreement No  
818 856559). MC participated in this work as Principal Investigator of the European Research  
819 Council (ERC) project FEAR (grant agreement No 856559) under the European Community's  
820 Horizon 2020 Framework Programme. FM, LDZ, APL and ET also participated in this work  
821 in the framework of the European Research Council (ERC) project FEAR (grant agreement No  
822 856559) under the European Community's Horizon 2020 Framework Programme.

823 AAG acknowledges additional support by the European Union's Horizon 2020 research and  
824 innovation program (TEAR ERC Starting; grant no. 852992) and Horizon Europe (ChEESE-

825 2P, grant no. 101093038; DT-GEO, grant no. 101058129; and Geo-INQUIRE, grant no.  
826 101058518), the National Science Foundation (grant nos. EAR-2225286, EAR-2121568,  
827 OAC-2139536, OAC-2311208), and the National Aeronautics and Space Administration  
828 (grant no. 80NSSC20K0495).

829 We thank Ravil Dorozhinskii, Thomas Ulrich and the SeisSol team (see [www.seissol.org](http://www.seissol.org)).  
830 We acknowledge the CINECA award under the ISCRA initiative, for the availability of high-  
831 performance computing resources and support.

832

## 833 **Open Research**

834 We use the SeisSol software package available on GitHub (<https://github.com/SeisSol/SeisSol>)  
835 to simulate all dynamic models. We use SeisSol, version {202103\\_\\_Sumatra-686-gf8e01a54}  
836 (master branch on commit dd018b3398258a23ec2a33c74bd7f31b503dcca6, v1.1.3-362-  
837 gdd018b33). The procedure to download and run the code is described in the SeisSol  
838 documentation ([seissol.readthedocs.io/en/latest/](https://seissol.readthedocs.io/en/latest/)). Downloading and compiling instructions are  
839 at <https://seissol.readthedocs.io/en/latest/compiling-seissol.html>. Instructions for setting up and  
840 running simulations are at <https://seissol.readthedocs.io/en/latest/configuration.html>.  
841 Quickstart containerized installations and introductory materials are provided in the docker  
842 container and Jupyter Notebooks at {<https://github.com/SeisSol/Training>. Example problems  
843 and model configuration files are provided at <https://github.com/SeisSol/Examples>, many of  
844 which reproduce the SCEC 3D Dynamic Rupture benchmark problems described at  
845 [https://strike.scec.org/cvws/benchmark\\_descriptions.html](https://strike.scec.org/cvws/benchmark_descriptions.html).

846 All data required to reproduce the dynamic rupture scenarios are available at ... .

847 The data will be fully archived at Zenodo at acceptance.

848

849 **References**

850

851 Abercrombie, R. E. (1995). Earthquake source scaling relationships from– 1 to 5 ML using  
852 seismograms recorded at 2.5-km depth. *Journal of Geophysical Research: Solid Earth*.

853

854 Abercrombie, R. E. (2021). Resolution and uncertainties in estimates of earthquake stress drop  
855 and energy release. *Philosophical Transactions of the Royal Society A*.

856

857 Abercrombie, R. E., & Rice, J. R. (2005). Can observations of earthquake scaling constrain slip  
858 weakening?. *Geophysical Journal International*.

859

860 Achtziger-Zupančič, Peter & Ceccato, Alberto & Zappone, Alba & Pozzi, Giacomo & Shakas,  
861 Alexis & Amann, Florian & Behr, Whitney & Botero, Daniel & Giardini, Domenico &  
862 Hertrich, Marian & Jalali, Mohammadreza & Ma, Xiaodong & Meier, Men-Andrin & Osten,  
863 Julian & Wiemer, Stefan & Cocco, Massimo. (2024). Selection and Characterisation of the  
864 Target Fault for Fluid-Induced Activation and Earthquake Rupture Experiments.  
865 10.5194/egusphere-2024-586.

866

867 Ampuero, J. P., & Ben-Zion, Y. (2008). Cracks, pulses and macroscopic asymmetry of  
868 dynamic rupture on a bimaterial interface with velocity-weakening friction. *Geophysical  
869 Journal International*, 173(2), 674-692.

870

871 Andrews, D. J. (1976). Rupture velocity of plane strain shear cracks. *Journal of Geophysical  
872 Research*, 81(32), 5679-5687.

873

874 Andrews, D. J. (1985). Dynamic plane-strain shear rupture with a slip-weakening friction law  
875 calculated by a boundary integral method. *Bulletin of the Seismological Society of America*,  
876 75(1), 1-21.

877

878 Allmann, B. P., & Shearer, P. M. (2007). Spatial and temporal stress drop variations in small  
879 earthquakes near Parkfield, California. *Journal of Geophysical Research: Solid Earth*.

880

881 Allmann, B. P., & Shearer, P. M. (2009). Global variations of stress drop for moderate to large  
882 earthquakes. *Journal of Geophysical Research: Solid Earth*.

883

884 Bai, K., & Ampuero, J. P. (2017). Effect of seismogenic depth and background stress on  
885 physical limits of earthquake rupture across fault step overs. *Journal of Geophysical Research: Solid  
886 Earth*, 122(12), 10-280.

887

888 Barbot, S., Lapusta, N., & Avouac, J. P. (2012). Under the hood of the earthquake machine:  
889 Toward predictive modeling of the seismic cycle. *Science*, 336(6082), 707-710.

890

891 Barras, F., Thøgersen, K., Aharonov, E., & Renard, F. (2023). How do earthquakes stop?  
892 Insights from a minimal model of frictional rupture. *Journal of Geophysical Research: Solid  
893 Earth*, 128(8), e2022JB026070.

894

895 Biemiller, J., Gabriel, A. A., & Ulrich, T. (2023). Dueling dynamics of low-angle normal fault  
896 rupture with splay faulting and off-fault damage. *Nature Communications*, 14(1), 2352.

897

898 Bizzarri, A. (2010). How to promote earthquake ruptures: Different nucleation strategies in a  
899 dynamic model with slip-weakening friction. *Bulletin of the Seismological Society of America*,  
900 100(3), 923-940.

901

902 Bolton, D. C., Affinito, R., Smye, K., Marone, C., & Hennings, P. (2023). Frictional and  
903 poromechanical properties of the Delaware Mountain Group: Insights into induced seismicity  
904 in the Delaware Basin. *Earth and Planetary Science Letters*, 623, 118436.

905

906 Brener, E. A., & Bouchbinder, E. (2021). Unconventional singularities and energy balance in  
907 frictional rupture. *Nature communications*, 12(1), 2585.

908

909 Bröker, K., & Ma, X. (2022). Estimating the least principal stress in a granitic rock mass:  
910 systematic mini-frac tests and elaborated pressure transient analysis. *Rock Mechanics and*  
911 *Rock Engineering*, 55(4), 1931-1954.

912

913 Bröker, K., X. Ma, N. Gholizadeh Doonechaly, A. P. Rinaldi, M. Hertrich, A. Obermann, V.  
914 Clasen Repolles, S. Wiemer, D. Giardini, H. Maurer (2023). Hydro-geomechanical  
915 observations during multistage hydraulic stimulation at the Bedretto Underground Laboratory,  
916 Switzerland. In: *Proceedings of the 57th US Rock Mechanics/Geomechanics Symposium*,  
917 Atlanta, Georgia, USA.

918

919 Candela, T., Wassing, B., Ter Heege, J., & Buijze, L. (2018). How earthquakes are induced.  
920 *Science*, 360(6389), 598-600.

921

922 Cappa, F., Scuderi, M. M., Collettini, C., Guglielmi, Y., & Avouac, J. P. (2019). Stabilization  
923 of fault slip by fluid injection in the laboratory and in situ. *Science advances*, 5(3), eaau4065.

924

925 Cebry, S. B. L., Ke, C. Y., & McLaskey, G. C. (2022). The Role of Background Stress State in  
926 Fluid-Induced Aseismic Slip and Dynamic Rupture on a 3-m Laboratory Fault. *Journal of*  
927 *Geophysical Research: Solid Earth*, 127(8), e2022JB024371.

928

929 Ciardo, F., & Rinaldi, A. P. (2022). Impact of injection rate ramp-up on nucleation and arrest  
930 of dynamic fault slip. *Geomechanics and Geophysics for Geo-Energy and Geo-Resources*,  
931 8(1), 28.

932

933 Cocco, M., & Rice, J. R. (2002). Pore pressure and poroelasticity effects in Coulomb stress  
934 analysis of earthquake interactions. *Journal of Geophysical Research: Solid Earth*, 107(B2),  
935 ESE-2.

936

937 Cocco, M., Tinti, E., & Cirella, A. (2016). On the scale dependence of earthquake stress drop.  
938 *Journal of Seismology*.

939

940 Cornet, F. H. (2012). The relationship between seismic and aseismic motions induced by forced  
941 fluid injections. *Hydrogeology journal*, 20(8), 1463.

942

943 Cornet, F. H. (2016). Seismic and aseismic motions generated by fluid injections.  
944 *Geomechanics for Energy and the Environment*, 5, 42-54.

945

946 Das, S., & Aki, K. (1977). Fault plane with barriers: A versatile earthquake model. *Journal of*  
947 *geophysical research*, 82(36), 5658-5670.

948

949 Dalguer, L. A., & Day, S. M. (2009). Asymmetric rupture of large aspect-ratio faults at  
950 bimaterial interface in 3D. *Geophysical Research Letters*, 36(23).

951

952 Dal Zilio, L., Hegyi, B., Behr, W., & Gerya, T. (2022). Hydro-mechanical earthquake cycles  
953 in a poro-visco-elasto-plastic fluid-bearing fault structure. *Tectonophysics*, 838, 229516.

954

955 Dumbser, M., & Käser, M. (2006). An arbitrary high-order discontinuous Galerkin method for  
956 elastic waves on unstructured meshes—II. The three-dimensional isotropic case. *Geophysical  
957 Journal International*, 167(1), 319-336.

958

959 Ellsworth, W. L. (1995). Seismic evidence for an earthquake nucleation phase. *Science*.

960

961 Ellsworth, W. L. (2013). Injection-induced earthquakes. *Science*, 341(6142), 1225942.

962

963 Fukuyama, E., & Madariaga, R. (1998). Rupture dynamics of a planar fault in a 3D elastic  
964 medium: rate-and slip-weakening friction. *Bulletin of the Seismological Society of America*.

965

966 Gabriel, A. A., Ampuero, J. P., Dalguer, L. A., & Mai, P. M. (2012). The transition of dynamic  
967 rupture styles in elastic media under velocity-weakening friction. *Journal of Geophysical  
968 Research: Solid Earth*, 117(B9).

969

970 Gabriel, A. A., Garagash, D. I., Palgunadi, K. H., & Mai, P. M. (2023). Fault-size dependent  
971 fracture energy explains multi-scale seismicity and cascading earthquakes. *arXiv preprint  
972 arXiv:2307.15201*.

973

974 Gabriel, A. A., Ulrich, T., Marchandon, M., Biemiller, J., & Rekoske, J. (2023). 3D Dynamic  
975 Rupture Modeling of the 6 February 2023, Kahramanmaraş, Turkey M w 7.8 and 7.7  
976 Earthquake Doublet Using Early Observations. *The Seismic Record*, 3(4), 342-356.

977

978 Galis, M., Ampuero, J. P., Mai, P. M., & Cappa, F. (2017). Induced seismicity provides insight  
979 into why earthquake ruptures stop. *Science advances*.

980

981 Galis, M., Ampuero, J. P., Mai, P. M., & Kristek, J. (2019). Initiation and arrest of earthquake  
982 ruptures due to elongated overstressed regions. *Geophysical Journal International*, 217(3),  
983 1783-1797.

984

985 Garagash, D. I., & Germanovich, L. N. (2012). Nucleation and arrest of dynamic slip on a  
986 pressurized fault. *Journal of Geophysical Research: Solid Earth*, 117(B10).

987

988 Geubelle, P. H., & Kubair, D. V. (2001). Intersonic crack propagation in homogeneous media  
989 under shear-dominated loading: numerical analysis. *Journal of the Mechanics and Physics of  
990 Solids*, 49(3), 571-587.

991

992 Guglielmi, Y., Cappa, F., Avouac, J. P., Henry, P., & Elsworth, D. (2015). Seismicity triggered  
993 by fluid injection–induced aseismic slip. *Science*, 348(6240), 1224-1226.

994

995 Grigoli, F., Cesca, S., Priolo, E., Rinaldi, A. P., Clinton, J. F., Stabile, T. A., ... & Dahm, T.  
996 (2017). Current challenges in monitoring, discrimination, and management of induced  
997 seismicity related to underground industrial activities: A European perspective. *Reviews of  
998 Geophysics*, 55(2), 310-340.

999

1000 Grigoli, F., Cesca, S., Rinaldi, A. P., Manconi, A., López-Comino, J. A., Clinton, J. F., et al.  
1001 (2018). The November 2017 Mw 5.5 Pohang earthquake: A possible case of induced seismicity  
1002 in South Korea. *Science*.

1003

1004 Harris, R. A. (2017). Large earthquakes and creeping faults. *Reviews of Geophysics*, 55(1),  
1005 169-198.

1006

1007 Harris, R. A., Barall, M., Aagaard, B., Ma, S., Roten, D., Olsen, K., ... & Dalguer, L. (2018).  
1008 A suite of exercises for verifying dynamic earthquake rupture codes. *Seismological Research  
1009 Letters*, 89(3), 1146-1162.

1010

1011 Hunfeld, L. B., Chen, J., Niemeijer, A. R., Ma, S., & Spiers, C. J. (2021). Seismic slip-pulse  
1012 experiments simulate induced earthquake rupture in the Groningen gas field. *Geophysical  
1013 Research Letters*, 48(11), e2021GL092417.

1014

1015 Hubbert, M., & Rubey, W. W. (1959). Role of fluid pressure in mechanics of overthrust  
1016 faulting. *Geological Society of America Bulletin*.

1017

1018 Ida, Y. (1972). Cohesive force across the tip of a longitudinal-shear crack and Griffith's  
1019 specific surface energy, *J. Geophys. Res.*, 77.

1020

1021 Imanishi, K., & Ellsworth, W. L. (2006). Source scaling relationships of microearthquakes at  
1022 Parkfield, CA, determined using the SAFOD pilot hole seismic array. Washington DC  
1023 American Geophysical Union Geophysical Monograph Series.

1024

1025 Jiang, J., Erickson, B. A., Lambert, V. R., Ampuero, J. P., Ando, R., Barbot, S. D., ... & van  
1026 Dinther, Y. (2022). Community-driven code comparisons for three-dimensional dynamic  
1027 modeling of sequences of earthquakes and aseismic slip. *Journal of Geophysical Research: Solid Earth*, 127(3), e2021JB023519.

1029

1030 Kame, N., & Yamashita, T. (1999). A new light on arresting mechanism of dynamic earthquake  
1031 faulting. *Geophysical research letters*, 26(13), 1997-2000.

1032

1033 Kammer, D. S., McLaskey, G. C., Abercrombie, R. E., Ampuero, J. P., Cattania, C., Cocco,  
1034 M., ... & Tinti, E. (2024). Energy dissipation in earthquakes. *arXiv preprint arXiv:2403.06916*.

1035

1036 Kanamori, H. (1981). The nature of seismicity patterns before large earth-quakes, in  
1037 Earthquake Prediction—An International Review.

1038

1039 Kanamori, H. (2003). Earthquake prediction: An overview. *International Geophysics*, 81,  
1040 1205-1216.

1041

1042 Ke, C. Y., McLaskey, G. C., & Kammer, D. S. (2018). Rupture termination in laboratory-  
1043 generated earthquakes. *Geophysical Research Letters*, 45(23), 12-784.

1044

1045 Ke, C. Y., McLaskey, G. C., & Kammer, D. S. (2022). Earthquake breakdown energy scaling  
1046 despite constant fracture energy. *Nature communications*, 13(1), 1005.

1047

1048 Kieranen, K. M., Savage, H. M., Abers, G. A., \& Cochran, E. S. (2013). Potentially induced  
1049 earthquakes in Oklahoma, USA: Links between wastewater injection and the 2011 Mw 5.7  
1050 earthquake sequence. *Geology*.

1051

1052 Kim, K.-H., Ree, J.-H., Kim, Y., Kim, S., Kang, S. Y., \& Seo, W. (2018). Assessing whether  
1053 the 2017 M w 5.4 Pohang earthquake in South Korea was an induced event. *Science*.

1054

1055 Kostrov, B. V. (1964). Self-similar problems of propagation of shear cracks. *Journal of Applied  
1056 Mathematics and Mechanics*, 28(5), 1077-1087.

1057 Lapusta, N., \& Liu, Y. (2009). Three-dimensional boundary integral modeling of spontaneous  
1058 earthquake sequences and aseismic slip. *Journal of Geophysical Research: Solid Earth*,  
1059 114(B9).

1060

1061 Larochelle, S., Lapusta, N., Ampuero, J. P., \& Cappa, F. (2021). Constraining fault friction and  
1062 stability with fluid-injection field experiments. *Geophysical Research Letters*, 48(10),  
1063 e2020GL091188.

1064

1065 Lee, K. K., Ellsworth, W. L., Giardini, D., Townend, J., Ge, S., Shimamoto, T., ... \&  
1066 Langenbruch, C. (2019). Managing injection-induced seismic risks. *Science*, 364(6442), 730-  
1067 732.

1068

1069 Lesko, K.: The Sanford Underground Research Facility at Homestake (SURF), *Physics  
1070 Procedia*, 61, 542–551.

1071

1072 Liu, L. and Zoback, M. D.: The effect of topography on the state of stress in the crust:  
1073 application to the site of the Cajon Pass Scientific Drilling Project, *J. Geophys. Res.*

1074

1075 Liu, Y., & Lapusta, N. (2008). Transition of mode II cracks from sub-Rayleigh to intersonic  
1076 speeds in the presence of favorable heterogeneity. *Journal of the Mechanics and Physics of  
1077 Solids*, 56(1), 25-50.

1078

1079 Lui, S. K., & Lapusta, N. (2018). Modeling high stress drops, scaling, interaction, and  
1080 irregularity of repeating earthquake sequences near Parkfield. *Journal of Geophysical  
1081 Research: Solid Earth*, 123(12), 10-854.

1082

1083 Ma, X., Hertrich, M., Amann, F., Bröker, K., Gholizadeh Doonechaly, N., Gischig, V., ... \&  
1084 Giardini, D. (2022). Multi-disciplinary characterizations of the Bedretto Lab a new  
1085 underground geoscience research facility. *Solid Earth*.

1086

1087 Ma, S., Custódio, S., Archuleta, R. J., & Liu, P. (2008). Dynamic modeling of the 2004 Mw  
1088 6.0 Parkfield, California, earthquake. *Journal of Geophysical Research: Solid Earth*, 113(B2).

1089

1090 Martínez-Garzón, P., Ben-Zion, Y., Abolfathian, N., Kwiatek, G., & Bohnhoff, M. (2016). A  
1091 refined methodology for stress inversions of earthquake focal mechanisms. *Journal of  
1092 Geophysical Research: Solid Earth*, 121(12), 8666-8687.

1093

1094 McGarr, A. (2014). Maximum magnitude earthquakes induced by fluid injection. *Journal of  
1095 Geophysical Research: solid earth*, 119(2), 1008-1019.

1096

1097 Meier M.A. et al. "Activation of a natural granitic fault zone at the BedrettoLab" submitted  
1098 to Solid Earth (EGU).

1099

1100 Miller, S. A., Collettini, C., Chiaraluce, L., Cocco, M., Barchi, M., & Kaus, B. J. (2004).  
1101 Aftershocks driven by a high-pressure CO<sub>2</sub> source at depth. *Nature*.

1102

1103 Moein, M. J., Langenbruch, C., Schultz, R., Grigoli, F., Ellsworth, W. L., Wang, R., ... &  
1104 Shapiro, S. (2023). The physical mechanisms of induced earthquakes. *Nature Reviews Earth  
& Environment*, 4(12), 847-863.

1106

1107 Palgunadi, K. H., Gabriel, A. A., Ulrich, T., López-Comino, J. Á., & Mai, P. M. (2020).  
1108 Dynamic Fault Interaction during a Fluid-Injection-Induced Earthquake: The 2017 M<sub>w</sub> 5.5  
1109 Pohang Event. *Bulletin of the Seismological Society of America*, 110(5), 2328-2349.

1110

1111 Pelties, C., De la Puente, J., Ampuero, J. P., Brietzke, G. B., & Käser, M. (2012). Three-  
1112 dimensional dynamic rupture simulation with a high-order discontinuous Galerkin method on  
1113 unstructured tetrahedral meshes. *Journal of Geophysical Research: Solid Earth*, 117(B2).

1114

1115 Ramos, M. D., Thakur, P., Huang, Y., Harris, R. A., & Ryan, K. J. (2022). Working with  
1116 dynamic earthquake rupture models: A practical guide. *Seismological Society of America*,  
1117 93(4), 2096-2110.

1118

1119 Rice, J. R. (1992). Fault stress states, pore pressure distributions, and the weakness of the San  
1120 Andreas fault. In *International geophysics* (Vol. 51, pp. 475-503). Academic Press.

1121

1122 Rinaldi, A. P., & Rutqvist, J. (2019). Joint opening or hydroshearing? Analyzing a fracture  
1123 zone stimulation at Fenton Hill. *Geothermics*, 77, 83-98.

1124

1125 Rinaldi, A. P., Rutqvist, J., Luu, K., Blanco-Martín, L., Hu, M., Sentís, M. L., ... & Kaestli, P.  
1126 (2022). TOUGH3-FLAC3D: a modeling approach for parallel computing of fluid flow and  
1127 geomechanics. *Computational Geosciences*, 26(6), 1563-1580.

1128

1129 Rubin, A. M., & Ampuero, J. P. (2005). Earthquake nucleation on (aging) rate and state faults.  
1130 *Journal of Geophysical Research: Solid Earth*, 110(B11).

1131

1132 Schmedes, J., R. J. Archuleta, and D. Lavalle   (2010), Correlation of earthquake source  
1133 parameters inferred from dynamic rupture simulations, *J. Geophys. Res.*, 115, B03304,  
1134 doi:10.1029/2009JB006689

1135

1136 Scholz, C. H., & Cowie, P. A. (1990). Determination of total strain from faulting using slip  
1137 measurements. *Nature*, 346(6287), 837-839.

1138

1139 Scholz, C. H., & Lawler, T. M. (2004). Slip tapers at the tips of faults and earthquake  
1140 ruptures. *Geophysical research letters*, 31(21).

1141

1142 Shapiro, S. A., Kr  ger, O. S., Dinske, C., & Langenbruch, C. (2011). Magnitudes of induced  
1143 earthquakes and geometric scales of fluid-stimulated rock volumes. *Geophysics*, 76(6), WC55-  
1144 WC63.

1145

1146 Scuderi, M. M., & Collettini, C. (2016). The role of fluid pressure in induced vs. triggered  
1147 seismicity: Insights from rock deformation experiments on carbonates. *Scientific reports*, 6(1),  
1148 24852.

1149

1150 Tago, J., Cruz-Atienza, V. M., Virieux, J., Etienne, V., & Sánchez-Sesma, F. J. (2012). A 3D  
1151 hp-adaptive discontinuous Galerkin method for modeling earthquake dynamics. *Journal of*  
1152 *Geophysical Research: Solid Earth*, 117(B9).

1153

1154 Tinti, E., Bizzarri, A., Piatanesi, A., & Cocco, M. (2004). Estimates of slip weakening distance  
1155 for different dynamic rupture models. *Geophysical research letters*.

1156

1157 Tinti, E., Casarotti, E., Ulrich, T., Taufiqurrahman, T., Li, D., & Gabriel, A. A. (2021).  
1158 Constraining families of dynamic models using geological, geodetic and strong ground motion  
1159 data: The Mw 6.5, October 30th, 2016, Norcia earthquake, Italy. *Earth and Planetary Science*  
1160 *Letters*, 576, 117237.

1161

1162 Tobin, H. J., Saffer, D. M., Castillo, D. A., & Hirose, T. (2022). Direct constraints on in situ  
1163 stress state from deep drilling into the Nankai subduction zone, Japan. *Geology*, 50(11), 1229-  
1164 1233.

1165

1166 Uenishi, K., and J. R. Rice (2003), Universal nucleation length for slip-weakening rupture  
1167 instability under nonuniform fault loading, *J. Geophys.Res.*

1168

1169 Ulrich, T., Gabriel, A. A., Ampuero, J. P., & Xu, W. (2019). Dynamic viability of the 2016  
1170 Mw 7.8 Kaikōura earthquake cascade on weak crustal faults. *Nature communications*, 10(1),  
1171 1213.

1172

1173 Uphoff, C., May, D. A., & Gabriel, A. A. (2023). A discontinuous Galerkin method for  
1174 sequences of earthquakes and aseismic slip on multiple faults using unstructured curvilinear  
1175 grids. *Geophysical Journal International*, 233(1), 586-626.

1176

1177 Viesca, R. C., & Garagash, D. I. (2015). Ubiquitous weakening of faults due to thermal  
1178 pressurization. *Nature Geoscience*, 8(11), 875-879.

1179

1180 Volpe, G., Pozzi, G., Collettini, C., Spagnuolo, E., Achtziger-Zupančič, P., Zappone, A., ... &  
1181 Cocco, M. (2023). Laboratory simulation of fault reactivation by fluid injection and  
1182 implications for induced seismicity at the BedrettoLab, Swiss Alps. *Tectonophysics*, 862,  
1183 229987.

1184

1185 Wang, L., Kwiatek, G., Renard, F., Guérin-Marthe, S., Rybacki, E., Bohnhoff, M., ... & Dresen,  
1186 G. (2024). Fault roughness controls injection-induced seismicity. *Proceedings of the National  
1187 Academy of Sciences*, 121(3), e2310039121.

1188

1189 Wollherr, S., Gabriel, A. A., & Uphoff, C. (2018). Off-fault plasticity in three-dimensional  
1190 dynamic rupture simulations using a modal Discontinuous Galerkin method on unstructured  
1191 meshes: implementation, verification and application. *Geophysical Journal International*.

1192

1193 Yeck, W. L., Hayes, G. P., McNamara, D. E., Rubinstein, J. L., Barnhart, W. D., Earle, P. S.,  
1194 & Benz, H. M. (2017). Oklahoma experiences largest earthquake during ongoing regional  
1195 wastewater injection hazard mitigation efforts. *Geophysical Research Letters*.

1196

1197 Zoback, M., Hickman, S., Ellsworth, W., & SAFOD Science Team. (2011). Scientific drilling  
1198 into the San Andreas fault zone—an overview of SAFOD's first five years. *Scientific Drilling*,  
1199 11, 14-28.

1 **Supplementary material**

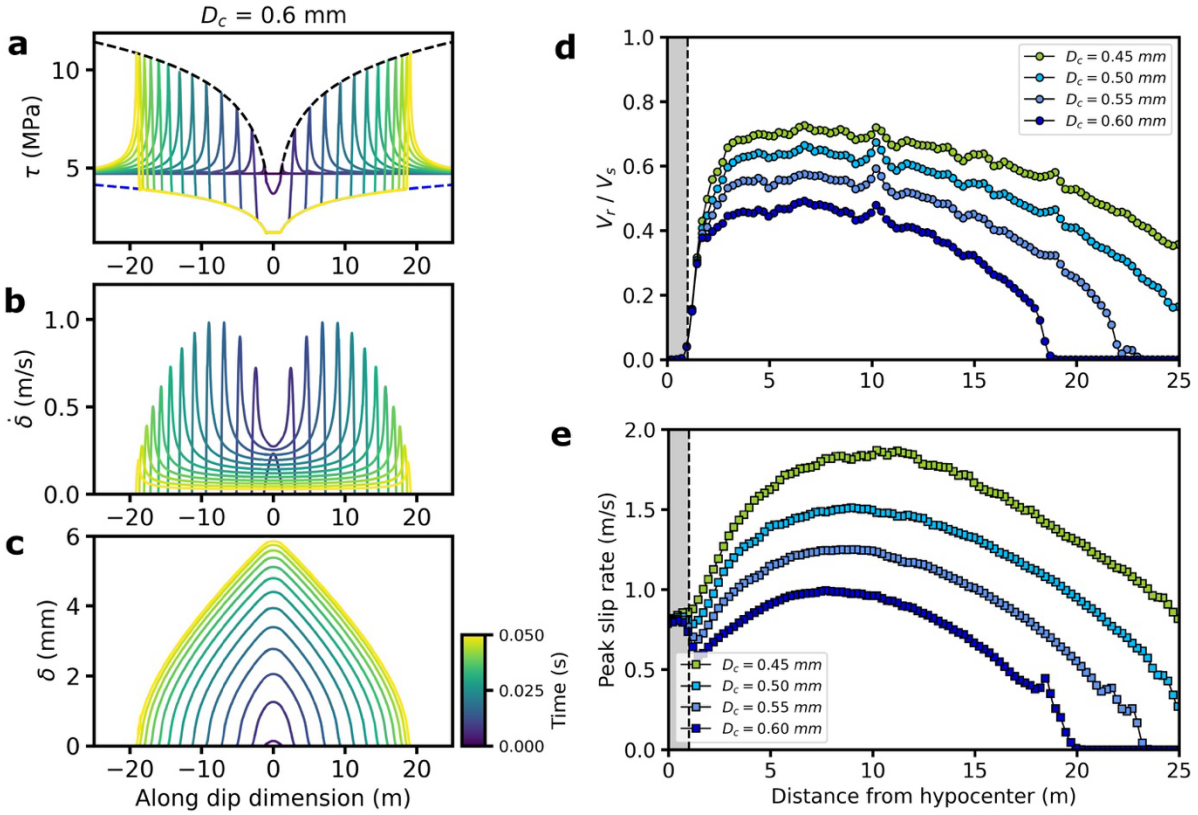
2  
3  
4

5 **Numerical method**

6 For the numerical simulations conducted in this study, we leveraged the advanced computational  
7 capabilities of SeisSol to capture the complex physical processes associated with induced seismicity.  
8 We employed high-order basis functions with a polynomial degree of  $p = 5$ , achieving  $\vartheta 6$  accuracy  
9 and double precision in both spatial and temporal wave propagation for all simulations. This high  
10 spatial and temporal resolution is crucial for accurately capturing the detailed spatiotemporal  
11 evolution of rupture processes. The fine resolution is particularly important for modeling the variable  
12 process zone size dictated by our frictional parameterization and stress conditions.  
13 SeisSol is optimized for the latest GPU architectures, allowing us to utilize a high-resolution mesh  
14 with approximately 69 million elements on the newly developed Leonardo cluster at CINECA. By  
15 employing 48 nodes, the simulations required approximately 5 hours, achieving an average  
16 performance of 208.746 TFLOP/s.

17

18



19

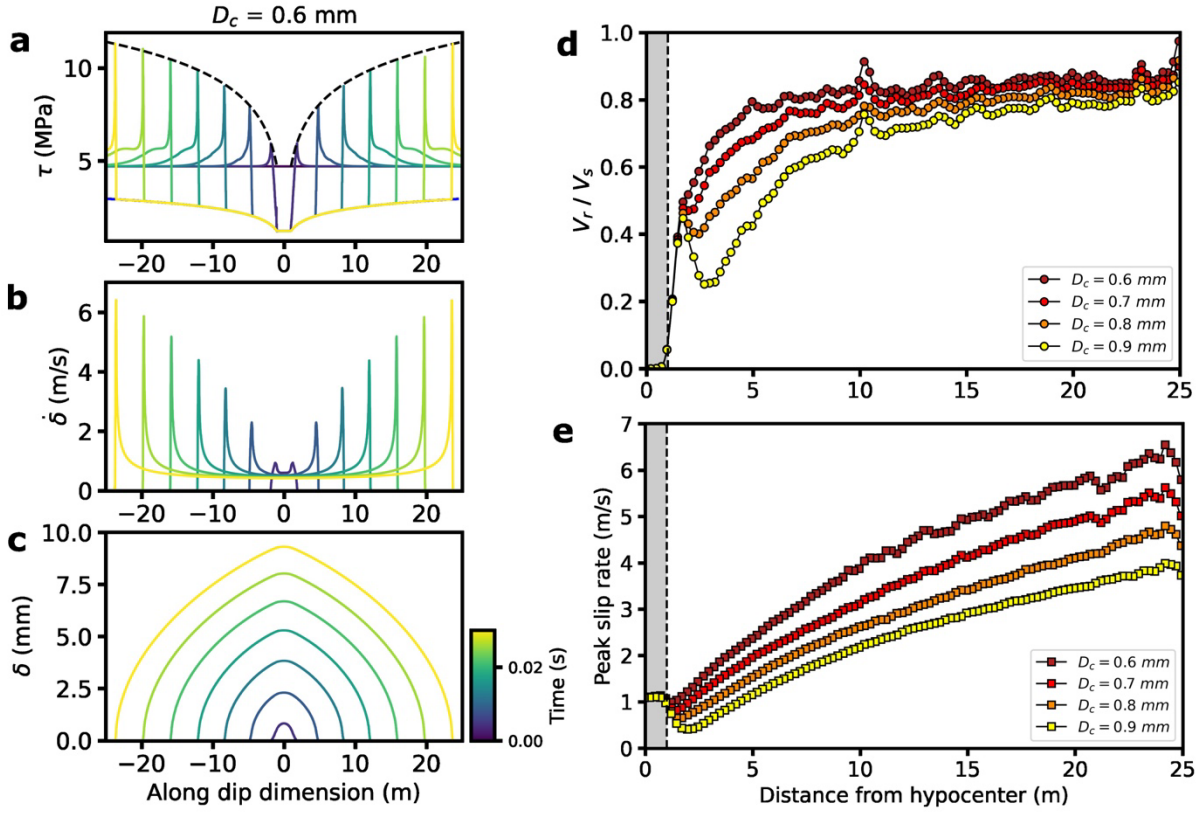
20

21 **Figure S1.** Illustration of the set models (A) with imposed  $\mu_d = 0.21$  for an along-dip section. (a-c)  
22 Example of rupture evolution through different snapshots of shear stress ( $\tau$ ), slip velocity ( $\dot{\delta}$ ) and slip  
23 profile ( $\delta$ ), the colormap indicates the temporal evolution of the rupture. (d) Rupture speed and peak  
24 slip rate (e) as a function of the hypocentral distance (injection point).

25

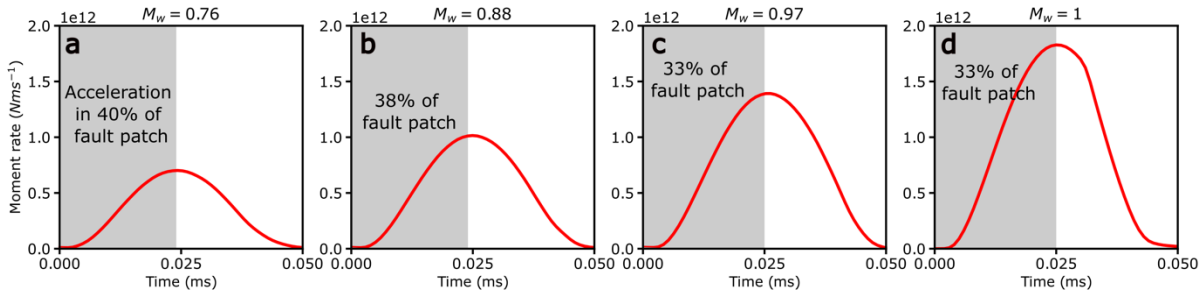
26

27



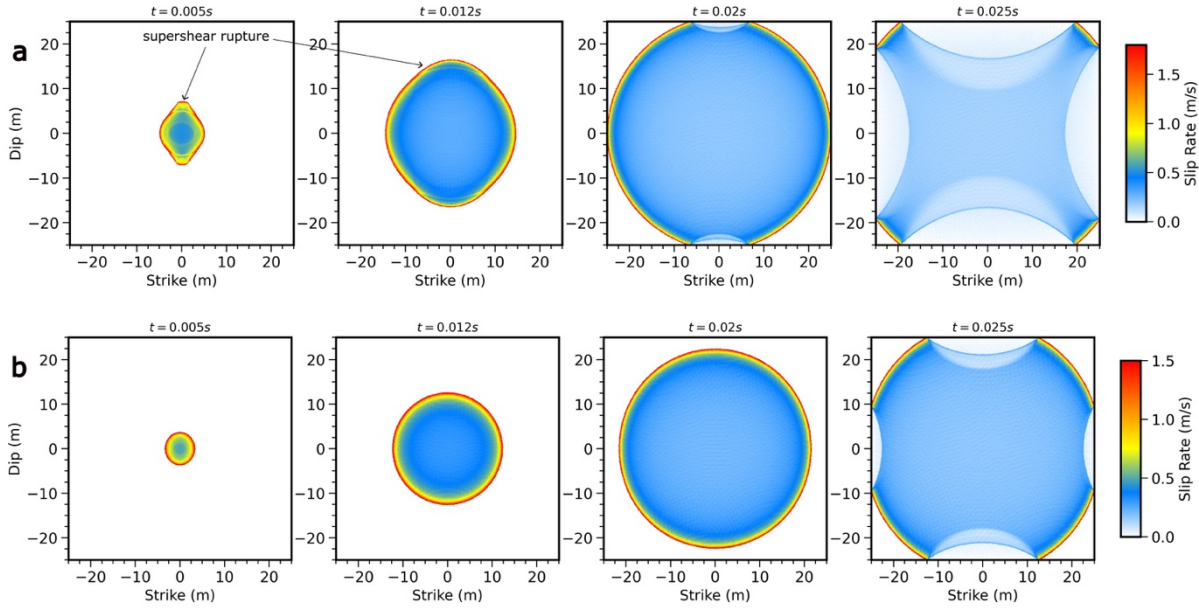
28  
29

30 **Figure S2.** Illustration of the set models (B) with imposed  $\mu_d = 0.15$  for along-slip section. **(a-c)** Example of rupture evolution through different snapshots of shear stress ( $\tau$ ), slip velocity ( $\delta'$ ) and  
31  
32  
33  
34  
35  
36  
37



38  
39

40 **Figure S3.** Moment rate function of numerical simulations in the set of models (A). **(a-d)** Displaying  
41  
42  
43  
44  
45



46

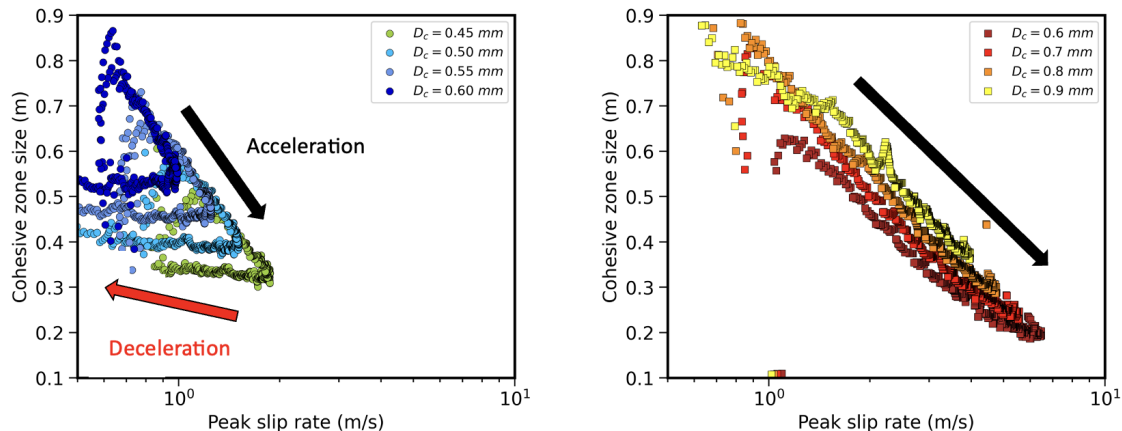
47

48 **Figure S4.** (a) Evolution of the dynamic rupture for the model with  $D_c = 0.1$  mm and (b)  $D_c = 0.2$  mm  
 49 belonging to the class of models (A), with the different panels that report the snapshots of the slip  
 50 rate during the rupture propagation.

51

52

53



54

55 **Figure S5.** Cohesive zone size versus the peak slip rate for self-arresting (set of models (A), left  
 56 panel) and runaway ruptures (set of models (B), right panel).

57